Computer Aided Medical Procedures
Prof. Dr. Nassir Navab

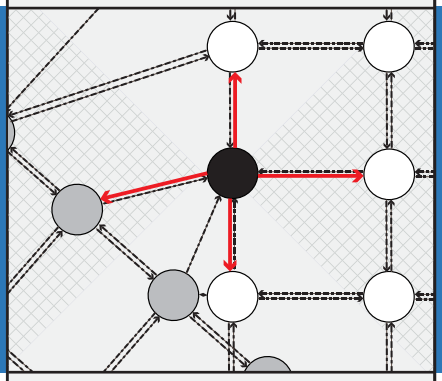

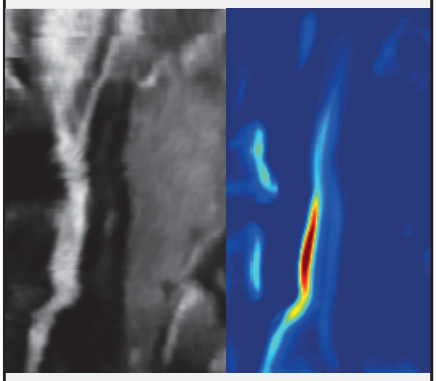

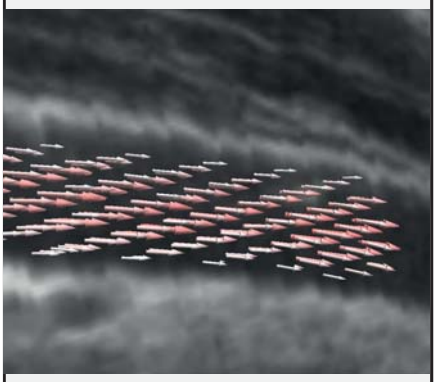

Dissertation

Domain-Specific Modeling for Vascular Freehand Ultrasound

Christoph Ludwig Hennersperger

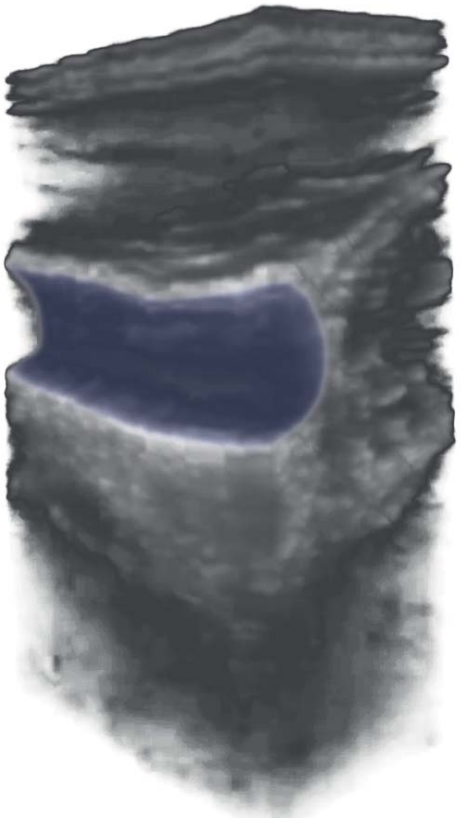

Fakultät für Informatik
Technische Universität München

TECHNISCHE UNIVERSITÄT MÜNCHEN

Fakultät für Informatik
Computer Aided Medical Procedures & Augmented Reality / I16

Domain-Specific Modeling for Vascular Freehand Ultrasound

Christoph Ludwig Hennersperger

Vollständiger Abdruck der von der Fakultät für Informatik der Technischen Universität München zur Erlangung des akademischen Grades eines

Doktors der Naturwissenschaften (Dr. rer. nat.)

genehmigten Dissertation.

Vorsitzender: Univ.-Prof. Dr. Nils Thuerey
Prüfer der Dissertation:
1. Univ.-Prof. Dr. Nassir Navab
2. Prof. Purang Abolmaesumi, PhD.
University of British Columbia, Kanada

Die Dissertation wurde am 26. Februar 2015 bei der Technischen Universität München eingereicht und durch die Fakultät für Informatik am 28. Mai 2015 angenommen.

Abstract

Ultrasound-imaging is nowadays the modality of choice for initial examinations in vascular applications. Real-time capabilities and the interactive nature of this modality allow trained sonographers to utilize their experience to perform reliable diagnosis with a minimal expenditure of time. For untrained doctors, however, a similar diagnosis is much more time-consuming and error prone. Consequently, especially 3D sonography suffers from a high dependency on the operator and variations of acquisition parameters, hampering the full clinical acceptance of those techniques.

With the goal of an improved reliability and quality of the whole ultrasound processing chain, this thesis introduces a set of mathematical and technical methods, incorporating domain-specific knowledge in both the acquisition process and further post-processing and quantification steps. This includes a novel solution for the acquisition of spatio-temporal ultrasound data, i.e. 3D+t information, by correlating pulse-oximetry sensors with ultrasound flow-velocity signals to retrieve an accurate reference for phases of cardiac pulsation. Moreover, both physically and biologically inspired models for an improved processing of ultrasound data are introduced. As such, a framework for a detailed physical modeling of ultrasound acquisitions is described, utilizing directed, unstructured graph networks to represent arbitrary sampling spaces, *i.e.* freehand ultrasound data. Based on such modeling, the estimation of confidence values for each sample of a 3D ultrasound acquisition is used to show the capabilities of the general framework. Furthermore, a geometrical model for the appearance of vessels in ultrasound images is introduced. Thereby, an approach to identify desired structures using specially designed filters is presented and second order derivatives are modeled accordingly. Finally, a biologically inspired waveform model of blood flow is used as a basis for the combined reconstruction of blood flow velocities along with laminar pulsation profiles from multiple 3D duplex-ultrasound acquisitions. Our results prove that such methods could potentially facilitate an improved understanding and future diagnosis of vessel flow dynamics in the clinical routine using 3D+t ultrasound imaging.

Zusammenfassung

Ultraschall als bildgebendes Verfahren ist heute die primäre Modalität für Erstuntersuchungen innerhalb der Gefäßdiagnostik. Dank einer hohen Interaktivität und der Möglichkeiten zur Bilddarstellung in Echtzeit können erfahrene Ärzte ihr Wissen einsetzen, um innerhalb kürzester Zeit eine zuverlässige Diagnose zu stellen. Im Gegensatz dazu neigen Ärzte mit wenig Erfahrung im Umgang mit Ultraschall zu zeitaufwändigeren und gleichermaßen fehleranfälligen Diagnosen. Aufgrund dieser hohen Untersucherabhängigkeit sowie des starken Einflusses von Aufnahmeparametern während der Untersuchung sind vor allem 3D-Ultraschall-Systeme heutzutage innerhalb der Medizin nicht weit verbreitet.

Mit dem Ziel einer höheren Verlässlichkeit und Qualität während der Aufnahme, wie auch in der weiteren Verarbeitung, beschreibt diese Arbeit sowohl mathematische als auch technische Methoden, um bildgebungsspezifisches Wissen innerhalb der Verarbeitungskette zu integrieren. Diese Methoden beinhalten zum einen ein System zur Aufzeichnung von 3D+t Ultraschall-Daten unter Verwendung eines Pulsoximeters in Korrelation mit Duplexsonographie während der Aufnahme, wodurch eine exakte Rekonstruktion der Pulsphasen innerhalb eines Blutgefäßes ermöglicht wird. Weiterhin werden Modelle zur physikalischen und physiologischen Modellierung zur verbesserten Verarbeitung der Daten vorgestellt. Einerseits werden dabei US-Aufnahmeparameter physikalisch innerhalb eines gerichteten, unstrukturierten Graphen modelliert, um daraus Informationen über die Zuverlässigkeit der Daten abzuleiten. Andererseits wird auch die spezifische Erscheinung von Gefäßen in Ultraschall-Bildern verwendet, um daraus ein geometrisches Modell herzuleiten. Hierfür wird ein Ansatz zum Auffinden von Zielstrukturen mittels speziell angepasster Filter innerhalb der zweiten Ableitung vorgestellt und auf Problemstellungen in der Gefäßdiagnostik angewendet. Schlussendlich wird innerhalb der Arbeit gezeigt, wie ein periodisches Pulsphasen-Modell unter Annahme eines laminaren Blutflusses verwendet werden kann, um aus mehreren 3D Duplex-Ultraschall-Aufnahmen ein vollständiges Flussprofil in 3D+t zu rekonstruieren. Die gewonnenen Ergebnisse zeigen dabei, dass derartige Methoden ein umfassenderes Verständnis der dynamischen Veränderungen des Blutflusses ermöglichen und somit langfristig auch für eine bessere Diagnosemöglichkeit sorgen können.

Acknowledgments

First of all, I would like to express my deep gratitude to Prof. Nassir Navab for enabling me the opportunity to pursue my research at the chair for computer aided medical procedures. To me, this was (and is) a great experience, especially thanks to his supervision, support and encouragement throughout the last three years. Without that, this thesis would have not been possible. Moreover, I want to thank my current colleagues Martina Hilla, Maximilian Baust, Benjamin Frisch, Oliver Zettinig, Richard Brosig, Diana Mateus, Asli Okur Kuru, Nicola Rieke, Fausto Milletari, Bernhard Fuerst, Ahmad Ahmadi, José Gardiazabal, Benjamin Gutierrez Becker, Silvan Kraft, Amin Katouzian, and Tobias Lasser for help, support, discussions and a lot of joy in the last years. Furthermore, among former colleagues, a special acknowledgment goes to Athanasios Karamalis, Brent Runyan and Kristin Henke for various constructive discussions and feedback during my first year at CAMP and as external PhD fellow.

Finally, I would like to thank my family and friends for the great support not only during the last years but throughout my whole life. This applies particularly to Claudia, for whose continuous support, warmth and joy I am deeply grateful.

Contents

Thesis Outline and Publications

In the following, a brief outline of the main chapters in this dissertation is presented.

Chapter 1: Introduction. In the first chapter, the basic principles of ultrasound imaging with a brief general history will be given, followed by an overview of the acquisition process and major clinical applications. Based on this general overview, vascular ultrasound as a main application field of the methods described in this thesis is introduced. In this scope, the current state of the art, recent technological advances and requirements for clinically applicable processing tools will be shown.

Chapter 2: Towards 3D+T Ultrasound. As the first major topic in this thesis, the second chapter discusses 3D ultrasound acquisitions over time. This includes an overview of applications, major challenges to be overcome, as well as prior art. Further, the main contribution to this area is introduced, incorporating anatomical and physical modeling of the ultrasound acquisition process into the problem statement.

Chapter 3: Advanced Computational Methods in Vascular Ultrasound. As the second field of contributions, advanced computational methods for vascular ultrasound are presented. In this regard, a general overview of ultrasound data processing, as well as main challenges and related work are given, followed by the main contributions for different modeling approaches. This includes a framework for general quadratic energy minimization problems, a method for multi-scale tubular structure detection specifically adapted to ultrasound imaging, and the reconstruction of 3D+T flow velocity profiles from multiple 3D Doppler ultrasound acquisitions.

Chapter 4: Conclusions and Outlook. The final chapter concludes the thesis with a brief summary of the main work presented in this dissertation, as well as remaining challenges and future directions, where a possible continuation of the presented approaches is described.

Chronologic List of Publications

[Hennersperger et al., 2014] C. Hennersperger, D. Mateus, M. Baust, and N. Navab, (2014), A Quadratic Energy Minimization Framework for Signal Loss Estimation from Arbitrarily Sampled Ultrasound Data. In *Medical Image Computing and Computer-Assisted Intervention - MICCAI 2014* (pp. 373-380). Springer International Publishing.

[Zettinig et al., 2014] O. Zettinig, C. Hennersperger, C. Schulte zu Berge, M. Baust, and N. Navab, (2014), 3D Velocity Field and Flow Profile Reconstruction from Arbitrarily Sampled Doppler Ultrasound Data. In *Medical Image Computing and Computer-Assisted Intervention - MICCAI 2014* (pp. 611-618). Springer International Publishing.

[Okur et al., 2014] A. Okur, C. Hennersperger, B. Runyan, J. Gardiazabal, M. Keicher, S. Paepke, N. and Navab, (2014), fhSPECT-US Guided Needle Biopsy of Sentinel Lymph Nodes in the Axilla: Is it Feasible?. In *Medical Image Computing and Computer-Assisted Intervention - MICCAI 2014* (pp. 577-584). Springer International Publishing.

[Hennersperger et al., 2014] C. Hennersperger, M. Baust, P. Waelkens, A. Karamalis, S. Ahmadi, and N. Navab, (2014), Multiscale Tubular Structure Detection in Ultrasound Imaging, In *Medical Imaging, IEEE Transactions on, 2014*

[Hennersperger et al., 2014] C. Hennersperger, A. Karamalis, N. and Navab, (2014), Vascular 3D+ T Freehand Ultrasound Using Correlation of Doppler and Pulse-Oximetry Data. In *Information Processing in Computer-Assisted Interventions* (pp. 68-77). Springer International Publishing.

[Rieke et al., 2014] N. Rieke, C. Hennersperger, D. Mateus, and N. Navab (2014), Ultrasound Interactive Segmentation with Tensor-Graph Methods, In *IEEE International Symposium on Biomedical Imaging 2014, Beijing, China*

[Feurer et al., 2012] R. Feurer, C. Hennersperger, B. Runyan, C.F. Seifert, J. Pongratz, M. Wilhelm, J. Pelisek, N. Navab, E. Bartels, and H. Poppert (2012), Reliability of a Freehand Three-Dimensional Ultrasonic Device Allowing Anatomical Orientation at a Glance: Study Protocol for 3D Measurements With Curefab CS', In *Journal of Biomedical Graphics and Computing, Vol. 2:2, 2012*

1 Introduction

1.1 Background and Main Objective

Up to the 19th century, accurate diagnoses were heavily relying on the experience of physicians. Technical assistance was primarily restricted to basic tools such as stethoscopes and other developments, in order to gain more information about the patient's health condition. Due to huge technical advances and discoveries, the upcoming century not only revolutionized civil life, but also the whole field of medicine in many ways. Among those discoveries, especially the detection of X-Rays by Wilhelm Conrad Röntgen in 1895 led to a breakthrough in medicine, resulting in the new domain of medical imaging.

While X-Ray has shown that interior parts of the body can be made visible with radiation transmitted through the body, the upcoming decades led to the development of other modalities, including medical ultrasound starting from 1949, the Computed Tomography in the mid 20th century and Magnetic Resonance Imaging starting from 1973. With those and other evolving modalities in place, medical imaging finally allowed for a detailed understanding of the human anatomy. In terms of applications, tomographic imaging modalities have quickly become standard of care in modern radiology, enabling not only 3D reconstructions of the whole body, but also a detailed and comprehensive view of specific anatomic regions, such as individual organs or tumors. As those modalities are usually targeted at a general-usage setup to provide full-body imaging, they mostly require patients to be placed within a spacious gantry unit, which impedes on-site diagnosis, *i.e.* at the patient's bed. Additionally, tomographic acquisitions may require images taken under influence of contrast-agents, often being nephro-toxic, or exposing patients to significant doses of radiation.

With this in view, sonography evolved as a standard for initial examinations in many medical disciplines, given the advantages of real-time and on-site imaging guided by the physician. Although being used frequently in daily routine, the interpretation of ultrasound images nowadays still remains challenging. The main reasons for this are the prevalence of imaging artifacts, and a strong operator dependence as a result of the ultrasonic imaging principle

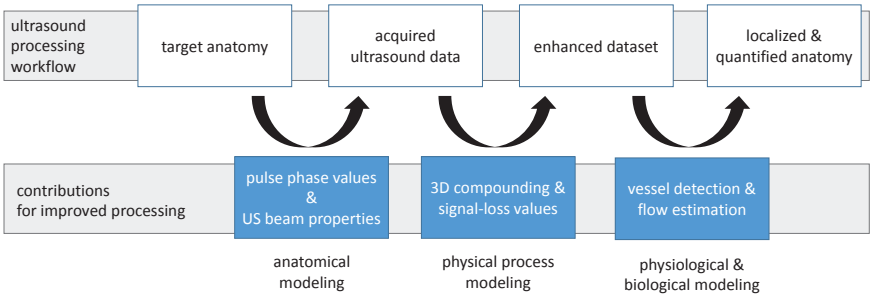

Figure 1.1: Ultrasound processing chain. In order to retrieve diagnostic values, ultrasound data of a desired region is collected, followed by an enhancement and an interpretation of the recorded information in order to retrieve diagnostic values.

of partial wave reflection at interfaces between tissues in the body. As the ratio of reflection differs with varying incision angles of the ultrasonic waves, acquisitions are heavily dependent on well-trained staff, and careful interpretation of the images is an elaborate task often requiring additional information about the imaging context. In today's practice, this contextual information is mostly provided by the fact that the physician directly guides the US imaging probe during examination, where the trained hand-eye cognition allows for an improved understanding of the anatomy during image acquisition. In distinction to 3D tomographic imaging modalities, and despite a variety of potential applications however, ultrasound suffers from this operator-dependence during acquisitions, imposing additional challenges to a potential post-processing of the data. This is also why the overall clinical availability of 3D-ultrasound solutions is still limited to certain applications where the whole target region of interest can be imaged directly by the probe, with prominent examples being echocardiography or imaging of small aortic aneurysms.

The main contributions presented in this thesis aim at improving the whole ultrasound processing chain in order to facilitate the acceptance of 3D ultrasound for vascular applications. In this context methods to incorporate physical and physiological modeling into different steps throughout the whole processing workflow will be shown, facilitating final diagnostic outcome, *cf.* Fig. 1.1. During acquisition, pulse-oximetry information is added for correlating vessel expansion and compression to acquired pulsed-wave flow estimates, leading to a full estimation of 3D flow profiles over cardiac cycles. Furthermore, ultrasound acquisition properties are included into compounding strategies, and processing methods for the retrieval of values of relative confidence for

the acquired ultrasound samples are presented, facilitating improved vessel detection in ultrasound data.

The Necessity of Modeling in Ultrasound Processing

In contrast to 3D imaging, 2D ultrasound is the modality of choice for a variety of applications where a diagnosis is necessary directly at the patient's bed, or within a limited time frame respectively. Moreover, ultrasonic waves are harmless to biological tissue and thus enable a high potential for screening applications in daily practice.

Within all general application fields, vascular ultrasound represents one of the major areas for both the screening and the diagnosis of acute events such as the detection of thrombi and stroke or aneurysm rupture [105]. The predominant tasks in this field include imaging of the vessels in the human body and blood hemodynamics by analyzing flow velocities. These methods allow for an inspection of the condition of the vessels as such, *i.e.* by detecting and grading a narrowing (stenosis) or widening (aneurysm) of arteries. An occurring disease can then be treated effectively by adapting the medication of patients, performing vascular surgery, or imposing an alternative treatment depending on the progress of the disease. With the advantages described above, ultrasound is recently enjoying an increased usage in new areas; a trend which is believed to continue in the next years.

When recalling the cognitive hand-eye coordination and action performed by the physicians during ultrasound imaging, it becomes immediately clear that in order to asses the images with respect to the given context, medical experts are heavily relying on their experience, such as knowledge of human anatomy and possible diseases. Collective information based on trained knowledge and experienced images can be summarized under the term of modeling, which can be categorized - with respect to the field of medical imaging and image processing - as follows:

1. *Physical modeling:* The specific physical properties and effects, characteristic for an imaging modality, are used to model specific image appearance and properties (*e.g.* noise models).

2. *Physiological modeling:* The anatomy, physiology, or even biochemistry of organs, vessels, tissue and other structures is modeled, *e.g.* by biomechanical or geometrical and deformable approaches.

While these different approaches pose challenges with respect to their integration into the clinical processing chain, they can drastically influence potential diagnostic outcome facilitated by further processing. This attempt of integrating modeling approaches into ultrasound imaging and processing is exactly the main scope of this thesis.

1.2 Essentials of Vascular Ultrasound

In this section, first a short overview of medical ultrasound in general will be given along with a brief history and a description of the detailed ultrasound image formation process. Next, it will be described how sonography can be utilized in vascular applications to detect and monitor diseases.

1.2.1 Brief History

While basic principles and effects of sound waves had already been examined by ancient philosophers and scientists, such as Pythagoras, Aristoteles, and Galileo, the fundamentals for the development of biomedical ultrasound were mostly discovered from the 18^{th} century on [19]. Essential knowledge about (non)linear acoustic wave propagation in liquids was already gathered by important mathematicians and physicians in the 18^{th} century, including Euler, Lagrange, and D'Almbert as well as Earnshaw, Helmholtz, Kirchhoff, Lebedev, Navier, Poisson, Raylegih, Riemann, and Stokes later in the 19^{th} century [23]. A major milestone for the theoretical understanding of ultrasonic acoustic wave propagation was presented by Rayleigh in 1877 with the book "The Theory of Sound", describing the propagation of waves in his two-volume experiment [112]. However, even earlier in 1842, Christian Doppler had discovered the well-known effect named after him, indicating that a moving wave source would cause a change in the perceived frequency, in relation to the movement velocity of the receiver. This forms the basis of today's vascular ultrasound imagery, where the speed of blood can be determined using this effect.

With respect to a real application of today's ultrasound technology, the discovery of the Piezo-electric effect by Pierre and Jacques Curie in 1880 [27] showed that pressure acting on certain crystals generated a potential difference between conducting surfaces attached to those crystals. This principle can also be reversed and serves as a general tool to transform mechanical stress into electric potentials. While today piezo-elements are used in a broad variety of industrial and medical applications, the discovery of the piezo-effect is the very foundation of all modern ultrasound transducers.

After the exploration of major theoretical and physical backgrounds of ultrasonic wave propagation and its effects, the start of World War I in 1914 led to a variety of practical developments aiming at sonar technology, with the goal of detecting enemy objects underwater. Among the scientists of that period, Paul Langevin certainly was the prime mover, together with his co-workers, namely Robert Boyle and Constantin Chilowski, developing the so-called "Hydrophone", the first practical system for using ultrasonic echoes to detect underwater objects [90]. In a patent filed in 1917, Langevin also describes a method to determine the relative motion of an object using the Doppler effect, leading to the development of Doppler Ultrasound [23]. Following those advances, Sokolov and Muhlhauser described techniques to detect small defects in metallic objects by continuous wave excitation. During World War II, a series of developments in similar fields were accomplished by Firestone and Sproule, again to detect small defects in metallic objects, where the majority of

outcomes was classified as confidential until the end of the war.

With a dual-transducer setup measuring the continuous wave (CW) transmission through the head, Karl T. Dussik and his brother Friedrich showed a 2D image of wave absorption through the ventricles in 1942, and more detailed in 1947. To do so, the transducers were aligned on both sides of the head with one being used for transmission, while the other served for reception [31, 32]. Although it was shown later that they only imaged artifacts caused by the transmission through the skull and not the ventricles, their work served as a main driving factor for further developments of ultrasound imaging techniques and the shift from transmission to reflection sonography as used in most of today's systems. [23].

While most of the developments before the end of World War II were considering 1D transmission through tissue over time only (the so-called Amplitude or A-mode), soon the interest in cross-sectional images arose in order to be able to interpret information more effectively with respect to the underlying anatomy. In this context, the development of a 2D-imaging system by Wild and Reid was another major milestone in ultrasound history [148]. In their work they showed how a cross-sectional image can be obtained from a mechanically rotated single element probe, and how the resulting sector image can be interpreted with respect to the underlying anatomy. This was also the key development leading to modern ultrasound imagery, showing the amount of reflection as changes in brightness, which finally lead to the term of B-Mode images. Among these new advances was also the development of non-invasive methods to measure the flow velocity of fluid using continuous wave ultrasound in arteries, as described by Kamus *et al.* [72] in 1954, going back to the very principles of Langevin and others. Two years later, the group around Satomura presented the first in-vivo results of flow-measurements in vessels, showing a potential applicability for the evaluation of vascular diseases. These findings were also verified by later experiments, although the underlying physiological principles remained unclear for some more years. Finally, starting from the 1960s several research groups identified the scattering of the red blood cells as main reason for the successful flow measurements, utilizing the Doppler frequency shift as basic principle.

In subsequent years, major advances of grayscale and flow ultrasound imaging techniques were achieved by separate groups around Kossoff and Brown, improving the overall image quality by beamforming techniques such as compound imaging, as well as logarithmic compression and amplification. In terms of commercial ultrasound systems, the Siemens Vidoson remains among the most well-known historic systems, as it was the first system being capable of providing real-time images with an ultrasonic wave frequency of 2.5 MHz. The major developments enabling this breakthrough were made by Krause and Soldner in Germany during the mid 1960s and allowed for the acquisition of 140 scan lines with a sampling rate of about 15 frames per second.

In the area of flow velocity estimation and in contrast to the continuous wave systems developed up to this time, several groups switched to the development of Pulsed Wave (PW) methods for flow measurement in the late 1960s.

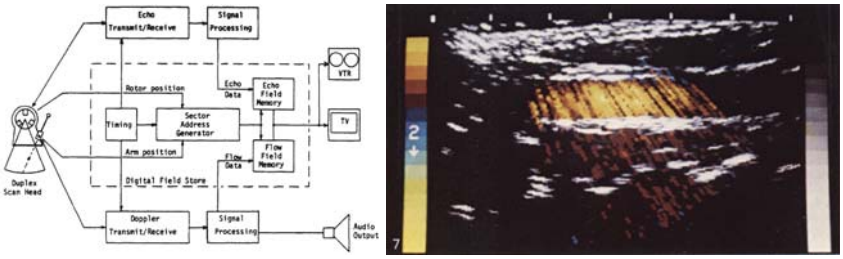

Figure 1.2: Early pulsed-waved duplex system. Shown are the system block-diagram of the system (left) and a resulting image showing a color coded flow visualization overlaid on B-mode grayscale images for the common carotid artery (right). Reprinted from [36] by permission from Elseveier.

While these are commonly referred to as PW Doppler, rather the movement of small scatterers between separate pulses than the resulting frequency-shift due to their movement is used to determine the velocity here, as discussed thoroughly in multiple publications in the mid 1980s [23]. The advantages of PW-systems over CW-estimation are thereby primarily that i) only one transducer is required for estimation, and ii) the depth of detected velocity estimates can be retrieved with PW-estimation in contrast to CW. Among the first of these systems was the one presented by Peronneau, who filed patent for flow estimation with a pulsed-system, followed by Baker, Watkins, and Wells' detailed report in 1969, presenting a pulsed-wave system to determine the velocity of cardiovascular structures. Following Baker and Watkins' efforts at the Univeristy of Wahsington, the first combination of B-Mode and velocity measurements was developed in the 1970s , which also shaped the term of Color-Coded Duplex (CCD) imaging. This allowed for a direct mapping of the vascular anatomy to measured flow velocities for the first time, providing a significant benefit for the field of vascular diagnosis. In the period around 1971/72, the first attempts towards an intuitive flow visualization were proposed by Hokansen and Fish. Finally, the works of Brandestini and Forter showed a full superimposition of grayscale B-Mode images with color flow velocity data for the first time in 1978, which is still used in a similar fashion in today's diagnostic machines [17].

From the end of the 1980s through the 1990s, the general image quality was further improved and additional technologies were developed. This included the introduction of 3D imaging by Von Ramm and Smith at the Duke University in 1987, as well as new imaging techniques, such as ultrasound elastography. Further achievements also lead to the exploration of better US contrast agents [98], gaining more importance in recent years within the context of accurate vascular diagnosis. All these advances facilitated the increased application of ultrasound imaging in practice with an associated improvement in image quality, and equipped with novel functionality. Finally, new developments continued throughout the last decade, when techniques such as plain wave imaging have drawn attention to both real-time and ultrafast scanning techniques of modern US systems, as well as the combination of

several ultrasonic signals for reliable and quantitative imaging.

1.2.2 Ultrasound Wave Propagation

Acoustic waves in the frequency range between 20 kHz and 1 GHz define the ultrasonic spectrum, where the distinction from lower frequencies is given by the definition of ultrasound not being perceivable by the human ear. While strictly spoken, ultrasound only defines a frequency spectrum, it is often used as a synonym for the respective imaging modality, whereas, depending on the application, frequencies ranging from 1 to 60 MHz are used in the medical field.

Ultrasonic (and general acoustic) waves transmitted through media can be categorized by their motion, with the two elementary forms being longitudinal and transverse waves. The former type, also referred to as compressional wave (*cf.* Fig. 1.3 left), employs a stress normal to the medium surface, which results in internally propagating areas of compression and rarefaction. In these regions, the particle displacements, densities, and other properties change over time as the area of excitement is traversing the medium. The overall wave transmit speed is called the speed of sound inside the medium, which is proportional to the material stiffness. In general, a higher stiffness leads to an increased speed, while more elastic materials will result in a slower transition of waves through the medium. Although the speed of sound varies even across (soft) tissue types, different assumptions for each tissue are not applicable in practice due to the lack of detailed knowledge about the different imaging media in clinical routine. Thus a speed of 1540 $\frac{m}{s}$ is usually set as a constant value in most of the modern ultrasound imaging systems, yielding an acceptable trade-off for most types of soft tissue appearing in the human body.

In contrast to longitudinal waves (*cf.* Fig. 1.3 right), for transverse waves the movement of particles is orthogonal to the wave propagation direction. Consequently, for these waves no regions of compression and rarefaction are present. However, particle movements in shear directions are induced. The shear movements are thereby proportional to the ratio given by the material-dependent shear modulus as well as the medium density.

In order to allow for an understanding and calculation of wave propagation in biological tissue, the continuity equation represents one of the basic principles by means of the conservation of mass. Thereby, this equation forces the mass of fluid flowing into a volume to be equal to the mass of fluid flowing out of the same volume, given by

$$\frac{\partial \rho}{\partial t} + div(\rho v) = 0, \tag{1.1}$$

where ρ is the density, $div()$ the divergence operation, and $v(x,t)$ the velocity of a particle at location x given at time t. The second equation required to simulate the propagation of viscous fluid extends Euler's equation of motion

$$\rho \left(\frac{\partial v}{\partial t} + (v\nabla)v \right) = -\nabla p, \tag{1.2}$$

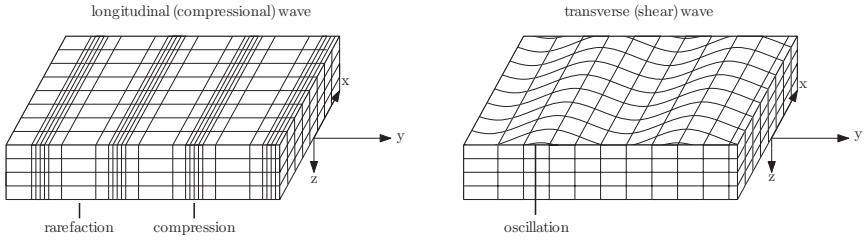

Figure 1.3: Wave propagation in y-direction for an isotropic medium. A plane longitudinal wave (left) produces propagating areas of compression and rarefaction with a movement in the axial y-direction , while for transversal waves particles move in the lateral x-direction (right).

relating the gradient of the pressure $p(x,t)$, given for a point in space and time, to the velocity of particles. By adding an additional term for shear stress, which is of significant importance in viscous fluid, this leads to the well-known Navier-Stokes equation

$$\rho\left(\frac{\partial v}{\partial t}+(v\nabla)v\right)=-\nabla p+\left(\mu_b+\frac{1}{3}\mu\right)\nabla(\nabla v)+\mu\nabla^2 v, \tag{1.3}$$

where μ an μ_b are the shear and bulk viscosities [23].

Finally, the propagation of longitudinal waves in a homogeneous medium can be defined as a combination of the continuity equation (1.1), and the Navier-Stokes-equation (1.3). In order to do so, the velocity potential $-\nabla\phi = v_L$ is introduced, whose gradient is the velocity of longitudinal waves v_L, leading to

$$\kappa\rho_o\frac{\partial^2\phi}{\partial t^2}=\nabla^2\phi+\kappa\left(\mu_b+\frac{4}{3}\mu\right)\frac{\partial}{\partial t}(\nabla^2\phi), \tag{1.4}$$

with κ being the adiabatic compressibility, relating a change in pressure to the change in density. Thereby, κ is based on the equilibrium density ρ_0, as well as the pressure and material density

$$\kappa=\frac{1}{\rho_0}\frac{\partial\rho}{\partial p}. \tag{1.5}$$

For the assumption of inviscid fluid, the given relation between velocity potential, pressure, and particle velocity, as introduced in Eq. (1.4) can be further reduced to

$$p=\rho_0\frac{\partial\phi}{\partial t} \tag{1.6}$$

$$\nabla p=-\rho_0\frac{\partial v}{\partial t}, \tag{1.7}$$

yielding a direct relation of the pressure to the velocity potentials, or the gradient of the pressure to a change of particle velocities respectively. The

latter forms an intuitive relation to the regions of compression and rarefaction indicated in Fig. 1.3. As the velocity of particles is correlating with changes in pressure, waves propagating through the tissue will cause periodic regions of changing pressures and particle velocities.

The distance between these indicated regions is referred to as wavelength λ and directly affects the resolution of objects which can be discriminated by an ultrasonic wave with a given frequency. The wavelength is in general given as the ratio between the propagation speed c and frequency f

$$\lambda = \frac{c}{f}, \tag{1.8}$$

which results in wavelengths of ultrasonic waves ranging from 1.54 mm for a frequency of 1 MHz up to 0.039 mm for 40 MHz, assuming a constant speed of sound as described above. In vascular ultrasound (excluding intravascular applications), frequencies in the range between 4 and 13 MHz are used most frequently, resulting in wavelengths between 0.39 mm and 0.12 mm. While λ describes the distance between compressional regions, the resolution of detectable structures using ultrasound waves varies for axial, lateral and elevational directions following the principles of wave propagation. In axial direction, the resolution is limited by the spatial pulse length of the acoustic wave, consisting of several wavelengths

$$R_a = \frac{L_p}{2} = \frac{n\lambda}{2}. \tag{1.9}$$

In practice, usually $n = 2,3$ pulses are used, enabling a straightforward relationship between wavelength and axial resolution. In lateral direction, the optimal resolution is affected by the focal length F and the aperture D of the transducer

$$R_l = 1.4\lambda\frac{F}{D}. \tag{1.10}$$

Figure 1.4 shows an example for a simulated ultrasound beam profile in axial and lateral directions. As can be seen, the beam width varies in lateral directions with increasing distance to the sound source. In this context, the beam width is indicating the width of the white region presented in the image in lateral direction, for which the acoustic pressure is within 6 dB of the emitted wave at the transducer source.

With a focus on the mechanical stress induced by ultrasonic waves, the vibrations characterized by the particle displacements in the media can be considered as an organized mass-spring system, *cf.* Fig. 1.5. Following this definition and making use of Hooke's law as well as Newton's second law [104, 109], we can reformulate the displacement of particles based on the mass and spring constants k as the harmonic function

$$\frac{\partial^2 x}{\partial t^2} + \frac{k}{m}x = 0, \tag{1.11}$$

whose solution is given by the form

$$x(t) = Asin(\omega_0 t + \phi_0), \tag{1.12}$$

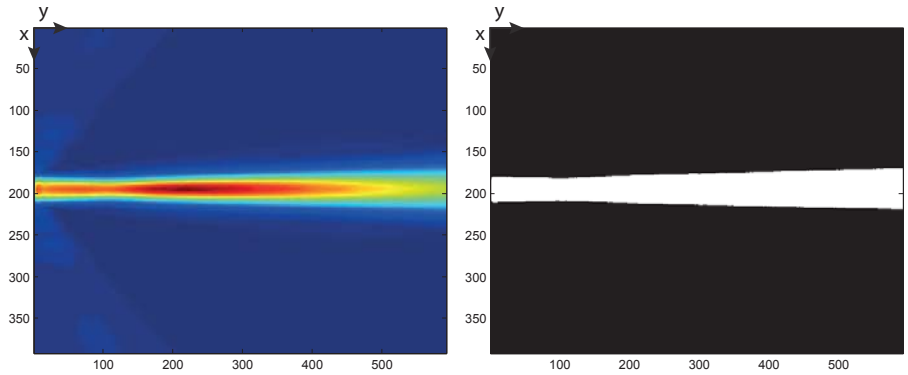

Figure 1.4: Simulated focused beam profile in the lateral-axial (x-y) plane based on ultrasound scan parameters. Left: Full simulated profile, where red to blue colors represent regions from high to low energies. Right: 6 dB field mask of the simulated ultrasound beam.

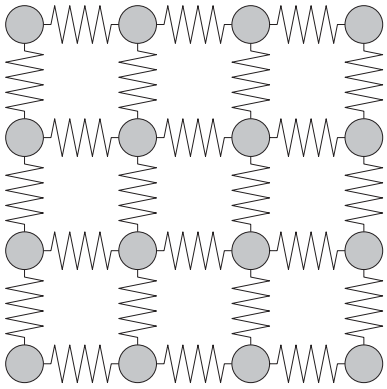

Figure 1.5: Mass-spring system as a model for particle vibration induced by ultrasonic waves. Particles are interconnected by springs, and their displacement is characterized by Hooke's law.

with the initial phase angle ϕ_0 and angular frequency

$$\omega_0 = \sqrt{\frac{k}{m}} = 2\pi f_0. \tag{1.13}$$

Given the additional constraints of the initial displacement x_0 and velocity v_0, A and ϕ_0 can be written for $t = 0$ as

$$A = x_0^2 + \frac{v_0}{\omega_0} \tag{1.14}$$

$$\phi_0 = tan^{-1}\frac{-v_0}{\omega_0 x_0}, \tag{1.15}$$

enabling the direct retrieval of the velocity v and acceleration a for a given

particle at the source and time t by using A and ω_0 respectively

$$v(t) = \frac{\partial x}{\partial t} = v_m cos(\omega_0 t + \phi_0) \tag{1.16}$$

$$a(t) = \frac{\partial^2 x}{\partial t^2} = -\omega_0 v_m sin(\omega_0 t + \phi_0). \tag{1.17}$$

The particle movement can be further extended to a function of the distance z to the transducer

$$x(t,z) = x_0 \, sin\left(\frac{2\pi}{\lambda}(ct - z)\right). \tag{1.18}$$

As both pressure and particle velocity are depending on the speed of sound c for given media, we can directly relate pressure and velocity, utilizing the material density

$$p(t,z) = \rho_m c_m \, v(t,z) = Z_m v(t,z), \tag{1.19}$$

where Z_m is the characteristic acoustic impedance for a given media m and is given by the product of the characteristic material properties, *i.e.* its density, and speed of sound

$$Z_m = \rho_m c_m. \tag{1.20}$$

As a whole, the acoustic impedance represents the basic physical quantity enabling ultrasound imaging at all, as different materials, such as fat, muscle, or water have different acoustic impedances. When an ultrasonic wave incises on an interface between two media with different acoustic impedances Z_1 and Z_2, Snell's law relates the angles of incision θ_i and transmission θ_t based on the speed of sound c_1, c_2 in both media

$$\frac{sin(\theta_i)}{sin(\theta_t)} = \frac{c_1}{c_2}. \tag{1.21}$$

In regard to the propagation of waves across tissue interfaces, two fundamental conditions must be satisfied, *i.e.* that both the pressure, as well as the particle velocity normal to the interface have to be continuous [109]. By using these conditions, Snell's law can be used to determine ratios of reflected and transmitted velocity potentials or pressures as

$$R_p = \frac{p_r}{p_i} = \frac{\phi_r}{\phi_i} = \frac{Z_2 cos(\theta_i) - Z_1 cos(\theta_t)}{Z_2 cos(\theta_i) + Z_1 cos(\theta_t)} \tag{1.22}$$

$$T_p = \frac{p_t}{p_i} = \frac{\phi_t}{\phi_i} = \frac{2Z_2 cos(\theta_i)}{Z_2 cos(\theta_i) + Z_1 cos(\theta_t)}, \tag{1.23}$$

where R_p and R_t are defined as reflection and transmission coefficients given an incident angle θ_i.

Figure 1.6 shows how Snell's law applies for a given interface between two media and how the Lambert cosine law relates to the observed wave intensity as a function of the incident angle to the surface. Similarly, these coefficients can be also described as the ratio between the intensity magnitudes of reflecting

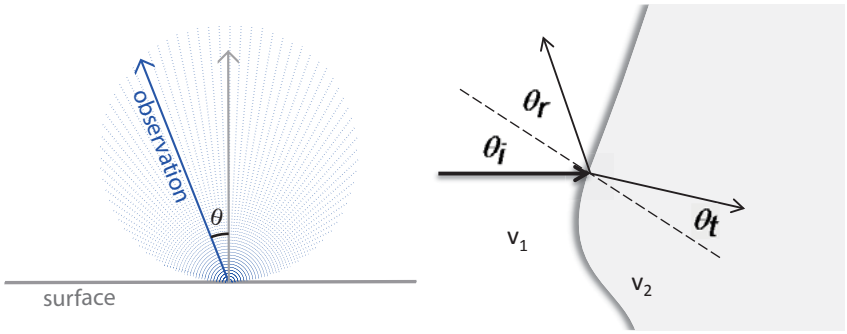

(a) Lambert's Cosine Law (b) Snell's Law

Figure 1.6: Lambert's cosine law (a) relates incident ultrasound waves to the observed reflected intensity for a given observation direction with respect to the incident angle. Snell's law (b) relates the ratio of incidence and transmission angle to the ratio of velocities in two interfacing media.

in incising waves [23]

$$R_i = \left(\frac{p_r}{p_i}\right)^2 = \left(\frac{Z_2 cos(\theta_i) - Z_1 cos(\theta_t)}{Z_2 cos(\theta_i) + Z_1 cos(\theta_t)}\right)^2 \tag{1.24}$$

$$T_i = \frac{4Z_1 Z_2 cos^2(\theta_i)}{(Z_2 cos(\theta_i) + Z_1 cos(\theta_t))^2}. \tag{1.25}$$

It becomes evident that for incident angles $\theta_i \neq \theta_t \neq 0$ the wave direction may change at tissue interfaces, referred to as refraction. However, with a normal incidence $\theta_i = \theta_t = 0$ to the interface, only reflection and transmission are present. Consequently, the reflection-transmission coefficients reduce to

$$R_i = \left(\frac{Z_2 - Z_1}{Z_2 + Z_1}\right)^2, \; T_i = \frac{4Z_1 Z_2}{(Z_2 + Z_1)^2}. \tag{1.26}$$

Figure 1.7 gives an example for an imaged region containing several media with different acoustic impedances. Emitted waves from the ultrasound transducer are partially reflected and transmitted at the interfaces between the media of acoustic impedances Z_1, Z_2, Z_3 facing normal incident angles to the surface.

An additional scenario being of high interest for multiple applications is the transmission of ultrasound waves through a medium with fixed thickness and defined acoustic properties. Such situations appear frequently in ultrasound phantom design or anatomical modeling, for which the transmission coefficient can be described as [23]

$$T_i = \frac{4Z_3 Z1}{(Z_1 + Z_3)^2 cos(\theta_2) + (Z_2 + Z_1 Z_3 / Z_2)^2 sin\,(\theta_2)^2}, \tag{1.27}$$

where $\theta_2 = 2\pi l / \lambda$ and Z_1, Z_2, Z_3 are the acoustic impedances, similar to the example given in Fig. 1.7. This relationship can be used in order to design

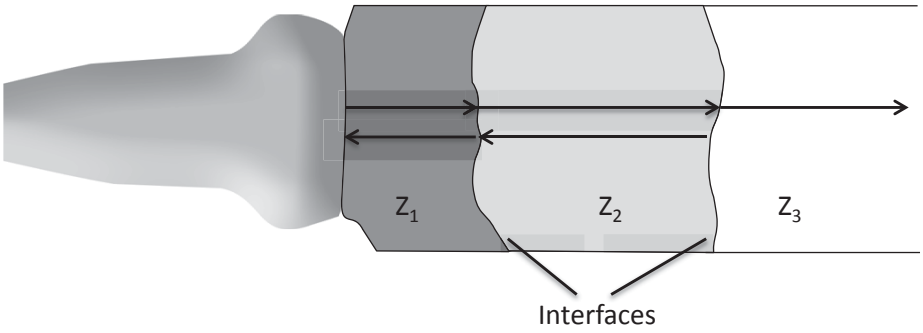

Figure 1.7: Example for several interfaces in an imaged region. Three media with acoustic impedances Z_1, Z_2, Z_3 are traversed by the ultrasound wave, causing subsequent reflections and the transmission of wave intensity at the respective interfaces.

layers of tissue where a passing wave will loose a defined (or even no) fraction of its intensity, and is valid for both liquids and solids.

In contrast to specially designed interfaces and layers in media such as human tissue, however, the wave energy is lost not only due to reflection at interfaces but also because of additional effects. The two predominant ones are absorption and scattering, often combined under the common term of ultrasound attenuation. Scattering describes the reflection of waves at objects smaller than the wavelength when, instead of a specular reflection as described above, a diffuse reflection is observed. More specifically, as a result of scattering at small objects, interference waves will be emitted from the scattering object in different directions, recursively causing a subsequent scattering at nearby objects. Although the visual impression of those speckle patterns seems to be noise-like, the process itself was recently shown to be a deterministic interference [124]. This also becomes evident visually, as tissue of a certain type exhibits similar speckle patterns, which is why ultrasound speckle is of high interest for various applications, such as tissue classification [121] and registration [137]. While speckle accounts for the scattering at small objects, absorption describes the loss of wave energy due to its conversion into other forms, such as heat. In detail, as the wave propagates through the tissue, regions of rarefaction and compression are caused by particle displacement, as already described in detail above. The movement and oscillation of particles causes a loss of wave energy and its dissipation as heat or chemical energy within the medium.

Following the physical principles presented above, it becomes evident that both scattering as well as absorption are frequency- and material-dependent. Consequently, a detailed modeling needs to be conducted in order to allow for a thorough examination of both effects. In many applications, a combined attenuation model is utilized, referring to the total loss of wave energy while traversing through tissue.

This attenuation can be modeled as a negative exponential gradual loss of wave energy with respect to the emitted intensity $I(0)$

$$I(z) = I(0)e^{-\alpha z}, \tag{1.28}$$

usually referred to as Beer-Lambert-Law. The attenuation coefficient α is frequency and temperature dependent; however, the frequency-dependence for most biological tissue can be reduced to

$$\alpha = \alpha_0 f^n, \tag{1.29}$$

where α_0 denotes the attenuation coefficient for a material given at constant temperature and n lies between 1 and 2 [23]. As the wave intensity decreases exponentially with increasing distance to the sound source, this intuitively indicates the physical limitations of the achievable penetration depth for certain frequencies, where the attenuation increases exponentially for higher frequencies.

1.2.3 B-Mode Image Formation

As already discussed in section 1.2.1, the discovery of the piezo-electric effect in 1880 was a major milestone in the development of modern ultrasound imaging technology, as it enabled the conversion of electric into mechanical energy; the basis for all modern ultrasound transducers. While most of the basic research in the early 20$^{\text{th}}$ century was conducted with single piezo-elements, the development of commercial systems yielded ultrasound transducers consisting of many single piezo-electric transducer elements. Today's probes usually consist of about 128 to 256 elements aligned in an array, enabling higher spatial resolution in lateral directions by combining several elements for the acquisition of images. In clinical practice, three basic forms of transducers exist for 2D ultrasound imaging, *cf.* Fig. 1.8:

1. *Phased arrays* employ a minimal footprint of the transducer to enable imaging through small acoustic windows, required for example in transcranial applications. The elements are therefore aligned on a line or plane and triggered with temporal delay in order to allow for a beam steering and associated imaging of a defined field of view (ultrasound fan).

2. *Curvilinear arrays* use single elements aligned on a circular arc with a given radius, allowing for an increase in the covered region without requiring additional movement of the probe. The main application region is abdominal imaging.

3. For *linear arrays*, elements are aligned on a rectangular array, such that a given region can be imaged with parallel ultrasound beams. Those arrays are frequently used in vascular diagnosis of the carotid and femoral arteries, as well as for high-resolution applications.

In addition, combined or modified forms exist for specific applications, such as trans-rectal or intra-cranial probes. In general however, those probes can be

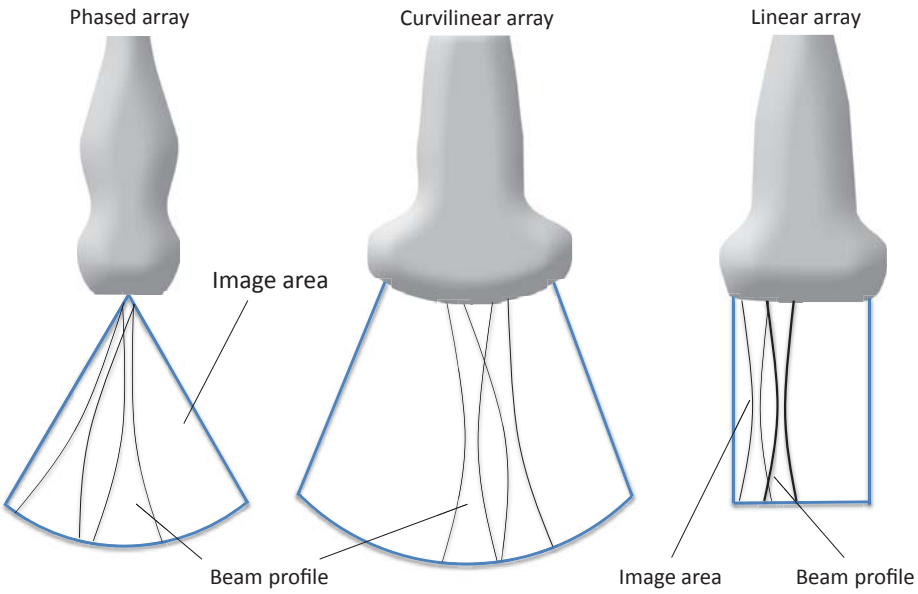

Figure 1.8: Three basic forms of ultrasound transducers with phased (left), curvilinear (middle) and linear (right) piezo arrays.

considered as modified forms of the fundamental probe geometries presented above.

With the goal of image generation, an ultrasonic pulse wave is first transmitted into the tissue, where individual piezo-elements are converting electrical signals into a mechanical wave. This pulse will cause reflections and other interactions within the tissue resulting in partially reflected waves returning to the transducer, as described in previous sections. In receiver-mode, the piezo-array will then convert the incoming wave energy back into electrical signals, which are processed in order to finally generate an output image for visualization and further processing. In more detail: For the transmission of ultrasonic waves, an ultrasonic pulse is generated as a convolution of the carrier signal at a certain frequency with a desired pulse, such as Gaussian or sinusoidal shapes. This allows for the control of the spatial pulse length of the ultrasound wave, such that the axial resolution can be set accordingly for the specific application. To generate a focused beam with an optimal spatial resolution with respect to the lateral and elevational directions, instead of transmitting the pulses simultaneously using all transducer elements, a short time delay is employed between the single elements, referred to as time-delay focus. Because of the change of temporal offsets within the array, the beam can thus be focused at desired locations. Alternatively, delays can also be incorporated to steer the whole ultrasound beam, as utilized in phased array transducers to cover a higher fan angle without requiring additional piezo-elements, or an increased probe footprint respectively. For an optimal control of the beam width and focus, usually not all but only a subset of the available transducer elements is used in order to generate a single scanline. Consequently, this

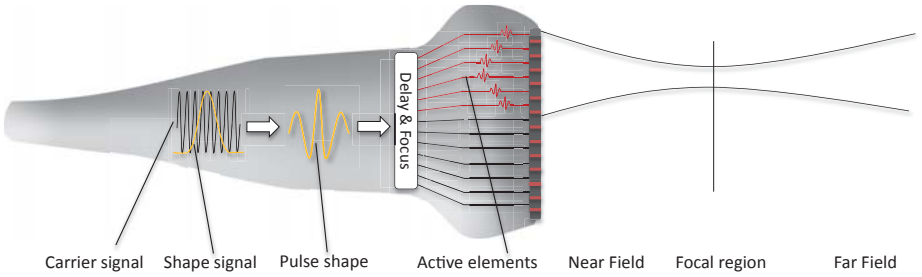

Figure 1.9: Ultrasound beamforming. The carrier signal with given frequency is shaped to create a pulse with a given length (usually 2-3 half-cycles). To create a focused ultrasound beam, the signals are transmitted delayed with respect to the single transducer elements of the probe.

allows for the acquisition of multiple scanlines in parallel and improved control of ultrasound beam shapes. Fig. 1.9 shows the basic process for ultrasound beamforming using a subgroup of all available elements (often about 5 to 30). In modern US systems, the transmitted pressure is further controlled separately for each piezo-crystal, where central elements are transmitting with higher power compared to the out-most ones. This approach is referred to as apodization, again enabling improved control over the desired beam shapes and properties. After transmission of the pulse for a desired scanline, the transducer switches into receiver mode, where it 'listens' to waves caused by reflection at subsequent tissue interfaces and processes the received signal in order to generate the final image, *cf.* 1.10 To do so, incoming waves are first amplified globally, followed by a local amplification for each depth value, *i.e.* time-gain-compensation (TGC). To allow for an analysis of the reflected waves, the signal is then demodulated in order to separate the carrier wave from the actual signal containing the reflection information. The modulated receiver signal can be written as

$$s(t) = a(t)\, cos(2\pi f_0 + \phi(t)), \tag{1.30}$$

with f_0 being the center frequency, $a(t)$ the signal amplitude, and $\phi(t)$ the phase. Eq. (1.30) can be represented in the complex domain by

$$z(t) = \mu(t)\, e^{j2\phi f_0 t}, \tag{1.31}$$

with $\mu(t) = |\mu(t)|e^{j\phi(t)}$ containing both amplitude and phase information, thus defined as the complex envelope signal [94]. Furthermore, $z(t)$ can alternatively be described as an analytic signal

$$z(t) = s(t) + jH\{s(t)\} \tag{1.32}$$

$$\tag{1.33}$$

where $H\{s(t)\} = \int_{x=-\infty}^{\infty} \frac{s(x)}{t-x} dx$ is the Hilbert transform of $s(t)$. The absolute value of the analytic signal is used in modern ultrasound systems to perform envelope detection, which is exactly the demodulation of the actual reflected

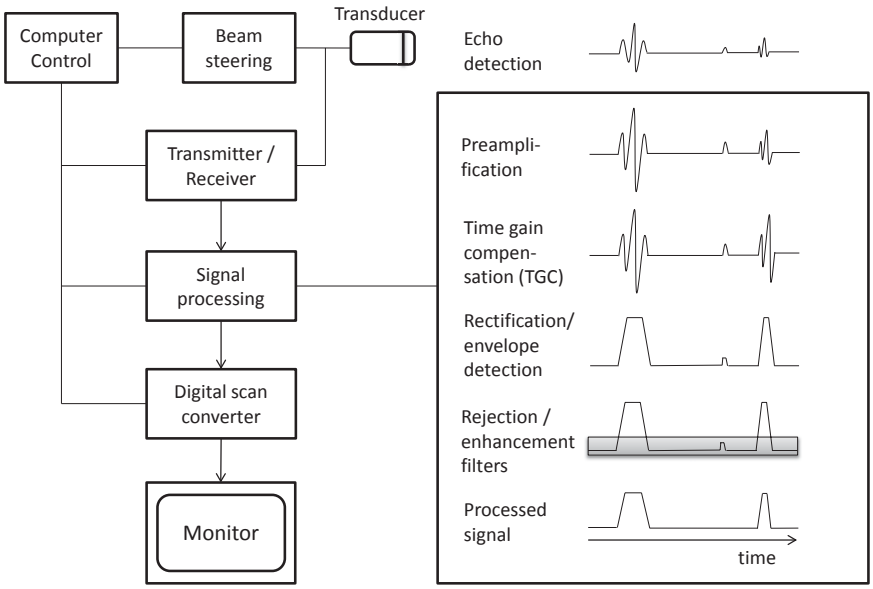

Figure 1.10: Ultrasound image generation system information flow.

signals from the carrier waves:

$$A = |z(t)| = \sqrt{s(t)^2 + H\{s(t)\}^2}. \tag{1.34}$$

The envelope A is then used for all further processing steps in order to retrieve images which can be shown to the end user. It should be noted that although the envelope detected data A are used for final presentation of ultrasound images to the physician, analytic or complex representations of the signals can be particularly useful, as they contain all available information acquired by the system hardware. For the example of speckle reduction, such information may be beneficial or even required to achieve a sufficient quality of the resulting image samples. In contrast to this, the envelope A is usually subject to further processing, where the signals are passed through a series of filters, for example to reduce the noise present in the data. While different groups of such filters are commercially available, most of the ultrasound manufacturers are developing and refining specialized pipelines for their own products, but details or implementations mostly remain unknown to the public and the research community. After post-processing of the data, the signal is interpolated from single scanlines, which were acquired using separately transmitted beams, to a 2D image representation of the ultrasound information. This step is called scan-conversion and represents the interpolation of the individually acquired rays into a 2D image. After scan-conversion, the image will be compressed in order to allow a perception of the whole dynamic range of the ultrasound data by the human eye, which is restricted to 8 or 16 bit of distinct gray-values.

In this sense, the output for one image I is denoted as

$$I = D\ln(A) + G, \tag{1.35}$$

where I is the final (displayed) intensity value, G a constant gain factor and D the dynamic range of the signal

$$D = \frac{X_{max} - X_{min}}{ln(A_{max} - A_{min})} = \frac{255}{ln(A_{max} - A_{min})}, \tag{1.36}$$

assuming maximum and minimum gray values of 255 and 0, representing an 8 bit image. The equation above describes the compression step as a nonlinear function of the envelope signal, for which also alternative forms can be found in literature [33].

1.2.4 Flow Image Formation

The retrieval of flow information from ultrasound data is of special interest for vascular applications, which is often referred to Doppler imaging in clinical practice. While the basic definitions of analytic signals and ultrasonic pulses for this imaging mode remain identical to the terms described in Section 1.2.3, several modifications to the transmission and reception of waves have to be made in order to allow for an estimation of blood flow velocities.

In this context, we recall the Doppler-effect as the relation between a change in frequency and the speed of a moving object, such as an ultrasound scatterer

$$f_D = -\frac{2v}{c_m} f_0 cos(\theta), \tag{1.37}$$

where v is the velocity of the scatterer, c_m the speed of sound in the media, f_0 the frequency and θ the Doppler angle, *i.e.* the angle between the movement direction of the object with respect to the observer. With today's ultrasound system, both continuous- as well as pulsed-wave estimation is possible, although pulsed-wave systems are more wide-spread in clinical practice. In general, ultrasound elements are constantly firing/receiving in transmission and reception mode for continuous-wave estimation of flow, while for pulsed-wave methods, transducer-elements will switch back and forth between both modes, similarly to classical B-Mode imaging. For a detailed introduction to continuous flow imaging, the reader is referred to [23], while we will focus mainly on pulsed-wave flow estimation. Although the Doppler-effect as presented above seems intuitive to explain the principle of pulsed-wave flow estimation, researchers are questioning since the early 1980s, whether it is in fact the responsible phenomena for flow estimation in pulsed-wave imaging [117]. While we skip a detailed explanation of the distinction from the basic Doppler effect, pulsed-wave imaging uses for flow estimation rather the movement of scatterers between two subsequent short pulses than their frequency shift. In practice, these movements relate to the distances traveled between the time points when the transducer elements are triggered in transmit mode. In contrast to this, the definition of the Doppler-effect would assume

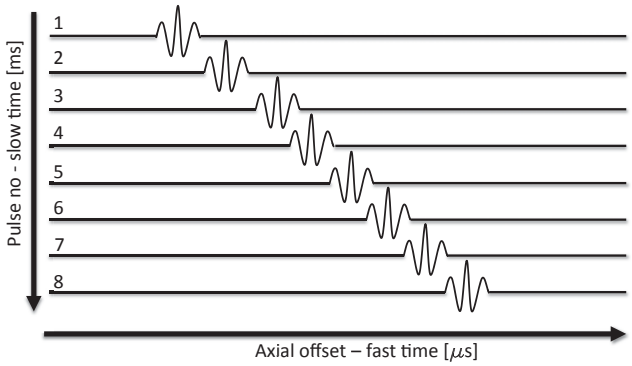

Figure 1.11: Received signal of a single scatterer for a series of fired ultrasound pulses into the media. For each pulse ($n = 1, 2, ..., 8$) referred to as slow-time, the scatter signal will arrive at the transducer with a different temporal delay (fast-time).

a frequency-shift of the ultrasonic waves due to the velocity of the moving scatterers observed at each point in time.

From the observation above it follows that at least two separate pulses have to be transmitted into the tissue to allow for an estimation of the velocity, where in practice usually about 8 to 12 pulses are used for the estimation along each scanline. For a specific direction and velocity of a moving scatterer (such as a red-blood cell) over time, its distance to the transducer source will vary, as the scatterer moves towards the probe or away from it. This behavior becomes evident from Fig. 1.11, where 8 pulses are transmitted subsequently into the tissue. For this scenario, the reflected scatterer signal will arrive with a varying temporal delay for each transmitted pulse, corresponding to a change of distance to the wave source.

The number of transmitted pulses is called ensemble and consists of n pulses shot over a given time period (slow-time) in the order of ms. Each pulse will be transmitted, reflected at scatterers, and the reflected wave will be received at the transducer. All these steps lie within a period of several μs, which is why a single pulse transmission-reception cycle usually is referred to as fast-time. For pulsed-wave acquisitions, the temporal distance between subsequent pulses is specified by the so-called pulse-repetition interval t_{PRI}. Its inverse quantity, the pulse repetition frequency $f_{PRF} = \frac{1}{t_{PRI}}$, represents one of the major settings to be adapted by the physicians according to the respective medical application. For the example above, the distance traveled by a scatterer between two pulses in beam-direction is given by

$$\Delta z = (v\, cos(\theta))t_{PRI}, \tag{1.38}$$

and can be evenly expressed in the delay time between two subsequent ultrasound pulses

$$\Delta t = \frac{2\Delta z}{c_m}. \tag{1.39}$$

This enables to reformulate the scatterer velocity as a function of the delay

time Δt, the speed of sound c_m, as well as the pulse-repetition interval and the angle of the scatterer movement direction with respect to the beam angle θ

$$v = \frac{c_m \Delta t}{2\, t_{PRI}\, cos(\theta)}. \tag{1.40}$$

Furthermore, by assuming a constant phase-shift for fast- and slow-time, the frequency of the latter signal can be defined as $f_{PW} = \frac{f_c \Delta t}{t_{PRI}}$, enabling an estimation of the velocity from received pulse waves using the relation

$$f_{PW} = \frac{2\, v\, cos(\theta)}{c_m} f_c. \tag{1.41}$$

The necessity of several short pulses transmitted into tissue obviously also implies certain restrictions to minimal and maximal velocity magnitudes, being detectable with pulsed-wave approaches. According to the Nyquist sampling criterion, a scatterer must not move with more than half a period length of the emitted pulse in order to be able to determine f_{PW} properly. Similarly, the minimum speed is determined such that at least one period has to be observed in a time window consisting of n pulses. Thus the maximum and minimum detectable speed of scatterers can be determined by

$$v_{max} = \frac{c_m f_{PRF}}{4 f_c cos(\theta)}, \quad v_{min} = \frac{c_m f_{PRF}}{2n f_c cos(\theta)}. \tag{1.42}$$

Above and below those limits, the estimations will be distorted by aliasing. Consequently, in clinical practice, a careful balance between the resolution of differentiable values (low absolute velocities - high pulse-repetition-frequency) has to be considered versus high absolute velocities (low pulse-repetition-frequency).

While the explanations above describe the flow estimation process for pulsed-wave excitations over time for a single position, the same principle can be extended to several samples along one scanline, as well as for multiple scanlines. Hereby, for each additional sample along a scanline, the required total processing time for a full image will increase based on the ensemble size n, and the pulse-repetition and center frequencies f_{PRF}, f_c. It should be noted here that the comparably low speed of sound is limiting the achievable update-rate for pulsed-wave acquisitions, requiring a trade-off between the desired field of view and high temporal sampling rates. Thus, flow estimates are usually restricted to a certain window in which they and their associated pulse-tranmissions will be carried out. Within these so-called gates, the estimated flow speed can be either displayed for single positions over time as velocity-time-curves, or as color-coded pulsed-wave duplex (CCD-PWD), where estimated velocities are superimposed in color on top of the gray-valued B-Mode images. For CCD, a mapping of blue to red colors based on movements towards or from the transducer are usually employed. Figure 1.12 shows two examples for CCD-PWD of the carotid artery, with both cross-sectional as well as longitudinal views.

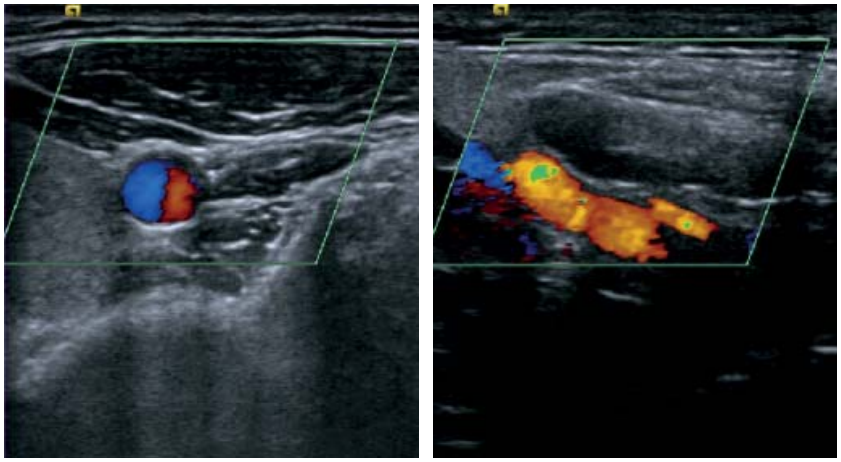

(a) Cross-sectional (b) Longitudinal

Figure 1.12: Cross-sectional and longitudinal views for pulsed-wave flow estimation. Color-coded values show movement towards/from the transducer in red/blue. Green areas show regions for which aliasing is present due to a non-optimal setting of the pulse-repetition frequency.

1.3 Clinical Background and Vascular Applications

As the general focus of this work is the field of vascular imaging, a short overview of major applications will be given below. The cardio-vascular system provides the main infrastructure to transport necessary substances within the body, including gases, nutrition, heat, hormones, antibodies, or water. In this cycle, the heart serves as main actuator, pumping blood through the cardiovascular system to target organs and extremities. All vessels used for blood streaming out of the heart are referred to as arteries, while inflowing blood is transported through veins. Each vessel contains of several layers, facilitating the transport of blood through the Lumen of the vessel. The innermost layer of the vessel wall is the Intima, a epithelium layer, interfacing to the Media, a layer of muscular tissue strengthening the stability of the overall vessel. While the Media can regulate the widening of arteries, such as for high and low temperatures, it is thick in comparison to the Intima, which by itself is usually not observable with ultrasound imaging. Consequently, the two inner layers are often considered as the combined Intima-Media complex. Finally, the out-most layer is referred to Adventitia and acts mainly as a fascia to the surrounding tissue.

Major diseases in the context of vessels are a narrowing of arteries due to atherosclerotic disease, as well as a widening (ballooning). The latter effect is in general referred to as Aneurysms, where the Abdominal-Aortic-Aneurysm (AAA) is the most occurring form [119]. With an increasing loss of elasticity of the aortic wall, mechanical stress caused by the blood flow streaming through the artery causes an extension of the vessel in diameter, ultimately leading

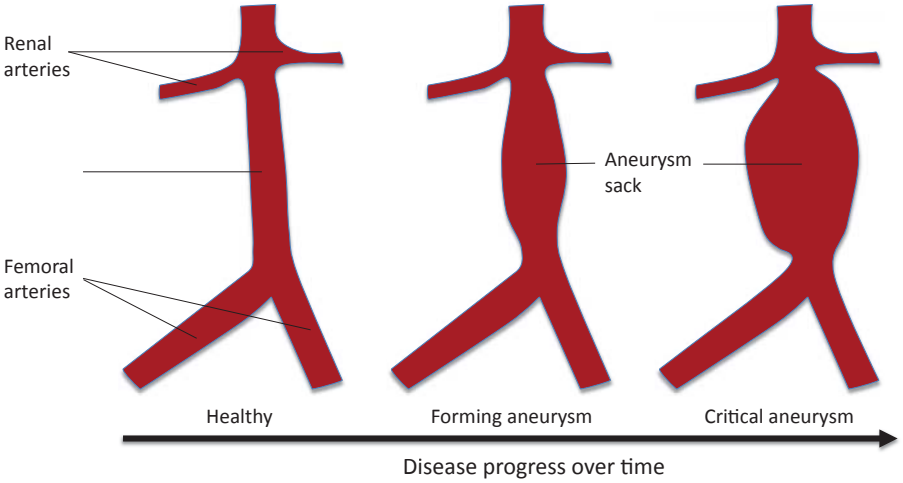

Figure 1.13: Stages of forming aneurysms. Due to shear stress acting on the vessel wall, the artery extends in size and an aneurysm sack forms over time. An increasing size of the aneurysm causes serious risk of rupture.

to a pronounced aneurysm sack. The main risk factor in this context is the aneurysm-rupture, which is characterized by high mortality if not treated in-time. Figure 1.13 shows a schematic progress of an AAA, where in most situations a ballooning is observable between the branches of the renal and femoral arteries, even though other forms exist similarly. Despite open surgery, endovascular abdominal repair (EVAR) of aneurysms is an increasingly used form of treatment for AAA, where a stent graft is placed within the artery through catheters. In general, the risk of mortality can be greatly reduced with an early detection and monitoring throughout progressing disease [119], facilitating screening applications for AAA. In this context, 2D ultrasound is the modality of choice for the initial diagnosis, mainly due to its fast examination times, high patient-safety as well as a potential support for screening scenarios.

The second major group of atherosclerotic diseases concerns the narrowing

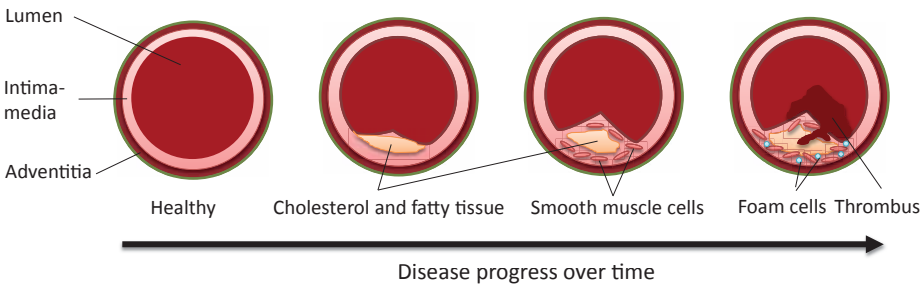

Figure 1.14: Different stages of forming plaques inside an artery. Throughout the progression of the disease, tissue is deposited at the inner artery wall, narrowing the blood flow increasingly, finally leading to vessel occlusion.

of arteries, which is widely considered as one of the major causes of death worldwide. Due to an inflammation of the epithelium (Intima) with subsequent binding of cholesterol within the arterial wall, material is deposited in the artery, referred to as arterial plaque. Throughout the progress of atherosclerosis, the arterial wall is thickened incrementally, resulting in an increasing constraint of the blood flow through the narrowed vessel Lumen (stenosis). Consequently, the available blood flow arriving at post-stenotic regions decreases, causing an under-supply of organs. If an artery finally gets fully occluded by plaques, serious events such as strokes or heart-failures are frequent consequences. A regular screening could avoid those cases, similar to aortic aneurysms.

Besides those major areas, a variety of smaller applications exist, including diseases of veins or inflammations. As vessels are in general well-observable by ultrasound imaging, it serves as one of the most important tools for the diagnosis of vascular diseases, especially in daily routine. For a detailed overview of the whole field of vascular diseases and their anatomical background, the reader is referred to [71, 79].

2

Towards 3D+t Freehand Ultrasound

Due to the real-time feedback of 2D+t ultrasound, the modality serves as a generic tool for diagnosis in vascular applications, as for example, changes in arterial flow can be easily examined over time by a medical expert. Moreover, it is possible to extend 2D and 2D+t ultrasound imaging to 3D and 3D+t imaging by considering the acquired sweeps as a volumetric dataset based on their spatial context. In this chapter the motivation, basic scope, today's challenges as well as potential future applications will be described with respect to the area of vascular 3D+t ultrasound as one of the main contributions of this thesis.

2.1 Problem Definition and Motivation

Given the basic physical principles of ultrasonic wave propagation, as introduced in the last chapter, the goal of 3D and 3D+t ultrasound is to provide 3D information either for a given time-step, or, alternatively, over a desired time frame. Thus, for every ultrasound sample s_i, a tuple consisting of the ultrasound intensity I_i, the position in 3D space x_i, and time information t_i is acquired

$$s_i = \{I_i, x_i, t_i\}. \tag{2.1}$$

In the view of acquiring such data, general concepts in order to provide 3D-information, assuming the examined anatomy to be static over time, are introduced at first. Two distinct approaches have evolved in the last 30 years to retrieve 3D ultrasound data [68]:

- *Matrix-array probes* enabling real-time 3D acquisition of a defined volume covered by the probe.
- *Freehand 3D ultrasound* using 2D ultrasound images with their spatial context, *i.e.* their position and orientation in space, to obtain volumetric information.

Matrix-array transducers (*cf.* Fig. 2.1a) as the first group consist of two-dimensional arrays of ultrasound elements aligned on a plane. Therefore,

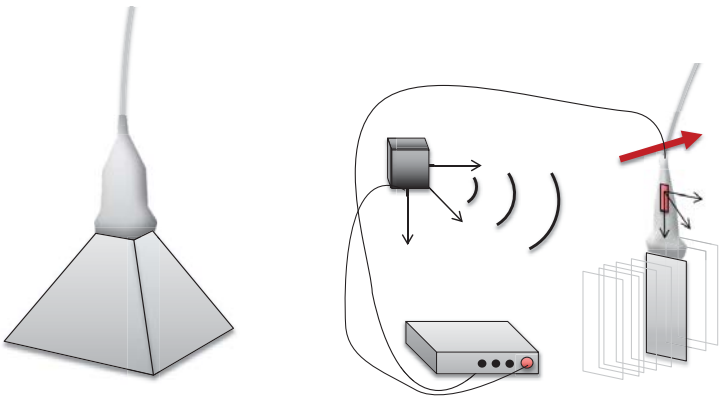

Figure 2.1: Basic techniques for the acquisition of 3D+t data. Left: Matrix array probes provide realtime 3D information for a volumetric region. Right: The freehand 3D scanning technique allows for dynamic movements and the coverage of arbitrary field of views.

the alignment of all single piezo-elements enables the system to cover not only a narrow 2D slice, but a defined volumetric region with several transmit-receive-cycles, so that 3D volume information can be acquired in real-time. It should be noted that the alignment of transducer-elements on a two dimensional array requires a significantly higher amount of elements to achieve a lateral resolution comparable to the one of linear arrays (often about 2000 to 3000 elements). Imposing more elements on a transducer results in additional requirements in terms of signal-processing, partial beamforming and multiplexing of signals. Thus, for most available systems, these steps are partially directly performed at the transducer, as the necessary cable connections running from the array to the ultrasound machine for the high number of elements would impose too high restrictions for the usability of such systems. Despite the first commercial release of matrix-array probes thirteen years ago and the associated benefits for a variety of applications [26], matrix probes unfortunately are still comparably expensive and open systems are not widely available. Today, the major application fields are echocardiography, as well as diseases which make it necessary that a whole volume of interest is captured by the probe at each point in time, *e.g.* small aortic aneurysms.

As an alternative to matrix-array transducers, freehand scanning techniques (*cf.* Fig. 2.1b) augment 1D- or 2D-information, as provided by any ultrasound device, with spatial pose information acquired by tracking systems or sensors in mechanical actuators to perform the respective movement [132]. In contrast to this, sensor-less approaches try to estimate the pose-changes between subsequent images directly from the acquired data, or assume a constant movement or rotation speed in order to allow 3D image reconstruction [67]. Due to the fact that for the latter approach the accuracy is highly depending on the performance and experience of the operator, systems augmenting 2D imaging with tracking information are used more frequently in clinical practice. Finally, ultrasound systems utilizing mechanically-actuated piezo-arrays

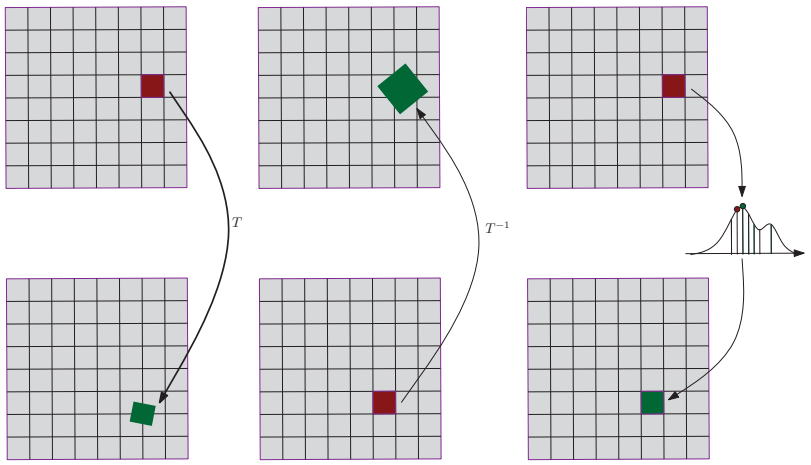

Figure 2.2: Interpolation strategies for compounding using forward transformations, backward transformations or estimation of functional parameters.

are often referred to as Wobbler-probes, being available for most ultrasound systems.

For further processing and visualization in combination with other 3D imaging data, such as CT- or MR-angiography, 3D freehand data is often interpolated with respect to a regular grid. This interpolation procedure is commonly referred to as 3D reconstruction or compounding [125] and can be done in different ways, with differences in both reconstruction complexity and quality of the resulting 3D images (compare Fig. 2.2):

- *Forward interpolation* transforms every sample (pixel) directly into the corresponding voxel to determine the final voxel intensity value. Compounding can be performed fast (real-time), but holes can occur as the mapping is not necessarily surjective with respect to the target voxels.

- *Backward interpolation* applies the inverse transformation to the target voxel position in order to interpolate the voxel intensity from the closest neighbors in pixel space, *e.g.* by trilinear interpolation. Compounding is considerably slower. However, holes are naturally avoided due to the surjectivity of the mapping.

- *Functional interpolation* is used if more than the closest neighbors in the pixel space shall be considered for interpolation. To do so, basis functions with a larger support are employed (such as B-Splines), which then can be sampled at the desired voxel positions in order to reconstruct an intensity value. Such interpolation can provide the best overall quality. However, it is often limited by the computational complexity of the reconstruction.

When comparing matrix-array imaging with freehand 3D ultrasound, it becomes obvious that the former technology provides the functionality to retrieve

3D information in combination with time domain data right-away. As the full volume can be covered by a single probe, these systems can acquire 3D+t data with up to 40 volumes per second [53]. In contrast to this, freehand techniques provide data with a high spatial resolution, but mostly neglect the temporal domain. In case of freehand 3D+t acquisitions, one usually has to trade temporal for spatial resolution and it is often advantageous to consider the acquired data as individual 1D-rays in 3D+t space or 2D image planes respectively, as they are sparsely distributed either in the spatial, or in the temporal domain. It should be noted here that also matrix-array probes can be combined with tracking devices in order to acquire freehand 3D+t ultrasound, combining volumetric images at several positions and time phases. Figure 2.3 shows an example for a

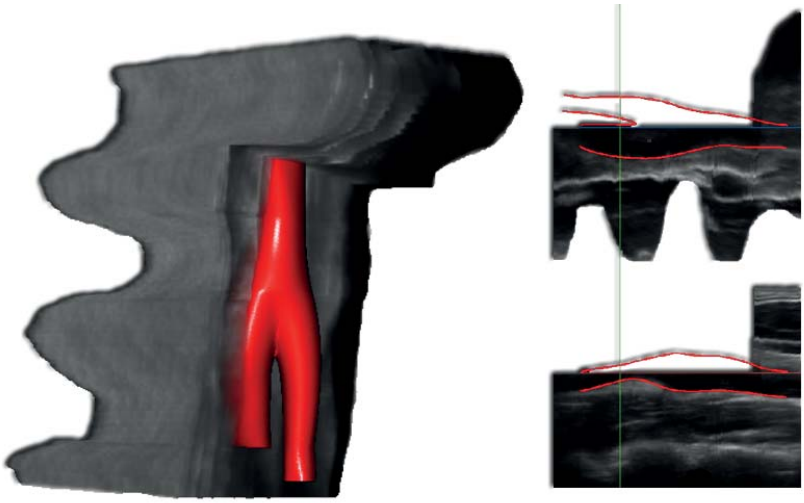

Figure 2.3: 3D-reconstruction (left) and two longitudinal cuts (right) through a freehand 3D-ultrasound scan with periodical lateral displacement during movement along the artery. The segmentation of the Lumen boundary shows the bifurcation from the common to the internal and external Carotid artery. Images were acquired with a Curefab CS 3D ultrasound system.

freehand 3D-ultrasound scan of the Carotid artery, acquired with a tracked 2D US probe using magnetic position tracking. To demonstrate the possibilities of dynamic acquisition trajectories as one of the main advantages of the freehand scanning technique, the transducer was moved freely in a sinusoidal trajectory along the artery for this acquisition. With respect to the sparsity in temporal domain, neglecting the time-domain can be potentially unfavorable for vascular diseases, as changes in time usually correspond to changes in the anatomy due pulsation, breathing or patient motion. Considering an artery for example, such changes include the expansion and compression of the artery, causing artifacts and distortions in the 3D volumetric reconstructions (*cf.* Fig. 2.4).

The main challenge in 3D+t freehand ultrasound is thus to utilize all available information in a way that optimally takes the sparsity with respect to the spatial or the temporal domain into account. In this context, spatio-

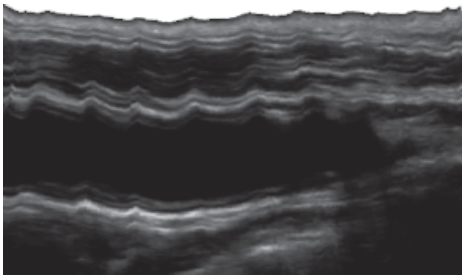

Figure 2.4: Pulsating artifacts in a longitudinal cut through a transverse free-hand 3D-scan without consideration of time as a separate domain.

temporal physiological models can be used in order to regularize the acquired information, especially with respect to the temporal domain. For vascular applications in particular, the temporal domain can be restricted to the period of cardiac pulsation, wherein an artery would move from a compressed state to full expansion and back to the initial state. Exploiting this periodic nature, *i.e.* repetitive cycles of cardiac pulse phases, measurements of several cycles can be merged in the spatial domain, which leads to an increased sampling rate in the temporal domain.

Under the assumption that a spontaneous movement of the patient can be excluded, similar physiological models can thus be utilized for image acquisition and throughout the whole workflow chain in general. In order to allow for a subsequent utilization of temporal information on top of 3D data however, it should be noted that already the acquisition should ideally incorporate additional sample information regarding the temporal domain. In this sense and with respect to vascular applications, we limit ourselves to methods for the detection of cardiac and breathing phase information, as these are the effects which are primarily reliable for alterations in the observed anatomy over time for vascular applications.

2.2 Medical Applications

Three-dimensional ultrasound information with an extension to the temporal domain enables a variety of specific applications in the vascular area, in particular as physical and physiological models are gaining increasing interest. In the following, we categorize applications in methods i) enabling temporal analysis, and ii) improving diagnosis for single points in temporal domain, and will describe possible approaches in detail.

Vessel Dynamics

Focusing on vascular applications, the evaluation of the vessel wall over time is certainly a promising area, where 3D+t information can facilitate the advancement of technology and medical knowledge. In this context, the arterial stiffness is known to correlate with atherosclerosis, and can be assessed locally

from arterial cross-sections with reference to the blood pressure, for example by distensibility or compliance [46]. Recently, it was shown that local evaluation can yield an improved detection of hypertension accompanied by a significant increase of local stiffness parameters [49]. Besides hypertension, an estimation of local vessel wall parameters for a whole arterial segment could provide important information for vascular surgeons in order to decide on optimal treatment.

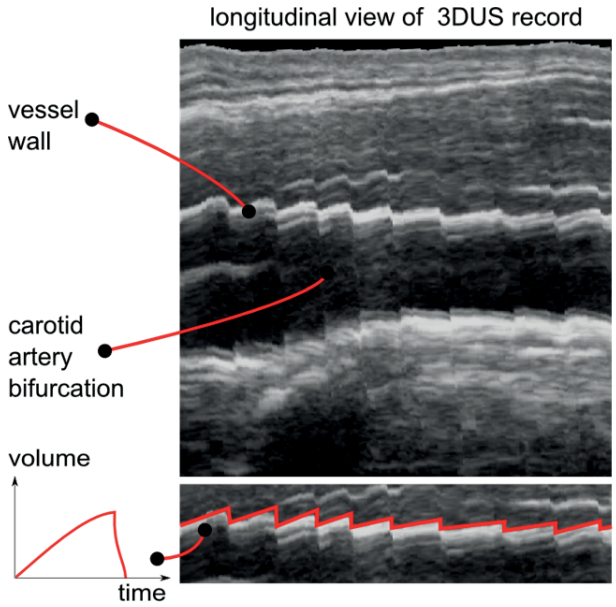

Figure 2.5: Slice through a transverse 3D-ultrasound scan of the Carotid artery. The red line marks the border between Intima-Media and Adventitia, showing significant vessel expansion and compression. In this case, non-constant velocity of the sweep results in non-periodic steps.

In clinical routine, such techniques could be used to determine the effect of alternative treatment strategies, such as different stent types versus bypasses, as increased arterial stiffness reduces the compliance of the vessel wall. In today's practice, however, estimation of stiffness and distensibility remain mostly experimental [88], which is also why methods to estimate pulse-wave-velocity as an indirect measure of arterial stiffness have evolved in the last years. Utilizing the dynamic behavior of the vessel wall over the period of a cardiac cycle however, local stiffness values of an arterial segment can be potentially obtained with high precision and reliability, *cf.* Fig. 2.5.

Besides evaluating the dynamics of vessel walls, also the diagnosis of the blood flow itself can profit from temporal information. Color-Coded-Duplex (CCD) acts as a standard tool in order to diagnose the progression of stenosis by evaluating flow velocities in narrowed arterial regions. Despite the strong inter-operator-variation between untrained and experienced sonographers, it was shown in retrospective studies that CCD provides the same quality as high-resolution MRA, and a superior quality in comparison to CTA [22],

where US was compared to both modalities in reference to intra-operative validation. Moreover, there has been a variety of research in the context of CA stenosis grading in the past [39, 55, 96]. The utilization of ultrasound imaging as a main diagnostic tool was thereby recently anchored in the guidelines for vascular surgeons in Germany. With the possibility of acquiring reliable 3D+t information for arterial segments, such data can be used for 3D blood-flow reconstruction over time, showing the full flow dynamics which could potentially be used as a quantity to evaluate the severity of disease progression on a per-patient basis. This would not only overcome the limitations of today's pulsed-wave measurements, but also resolve the angle-dependency of current methods. Furthermore, appropriate adjustments by the physician enable an integration of such information into the processing chain as well as their utilization for physiological modeling of diseases.

Improving Image Quality

Contrary to approaches for intrinsically dynamic scenarios, methods designed for the assessment of static structures such as inelastic cysts subject to motion due to the movement of adjacent structures can profit from the acquisition of 3D+t data as well. Particularly 3D compounding and reconstruction methods could directly benefit from a restriction of the compounding to a certain time step, as artifacts due to anatomical changes can be, roughly speaking, averaged out, as shown in Fig. 2.5. In practice, neglecting time information can result either in distortions due to pulsation-artifacts, or in a significant motion blur when samples of different time phases overlap in the same region. It becomes evident from this observation that appropriate compounding can resolve these problems by considering only points within a certain time frame for volumetric reconstruction. In addition to compounding, post-processing methods could profit equally well of the above-mentioned considerations. In the case of image segmentation for instance, gradient information is an important cue for many available methods. As a consequence, the segmentation of target structures may become more challenging in case of distorted gradients, *i.e.* due to washed-out image information caused by motion blur.

In contrast to external motions, *i.e.* transducer movement, also internal motions such as arterial expansion and compression should be considered. For the example of vessel tracking, the contour of a vessel wall should be localized in subsequent frames, *e.g.* by employing Kalman-filters, which are often used in order to initialize the contour tracked on a previous frame at similar positions at the current one. If the contours are drastically changing, for example due to an instantaneous expansion of the vessel between subsequent frames, the quality of such approaches might however decrease.

Finally, even if a segmentation or tracking may result in accurate outcomes, the comparability to other acquisitions of the patient or to records of other patients is particularly difficult as there is no reference to the utilized phase of cardiac pulsation as basis for the segmentation. The comparison of estimated quantitative values such as aneurysm or plaque volume [34] could thus be falsified by the comparison of results for different pulse phases.

2.3 Challenges in 3D+t Ultrasound

With respect to a full acceptance and integration into the clinical workflow, several challenges have to be overcome in the context of 3D+t ultrasound acquisitions, which will be described next.

Improving Diagnostic Value

The improvement of the diagnostic value is of predominant importance in order to facilitate the clinical acceptance, which directly relates to the spatial and temporal accuracy of 3D+t data. While the spatial resolution is restricted by physical limitations, such as the usable wave-length and the ultrasound beam properties, temporal sampling can be influenced by both the imaging hardware as well as the acquisition protocol itself (*i.e.* scanning of a volume of interest within a certain time frame). Furthermore, the robustness with respect to noise and varying quality for different target anatomies has to be verified and maintained from a practical point of view, in order to ensure a continuously high quality in the clinical routine. As ultrasound is considered as an imaging modality with high intra-observer-variability, the reliability of all processing steps has to be evaluated carefully, *i.e.* by exhaustive tests with different patient groups and target applications. In line with this, possible calibration steps have to be assessed carefully and with respect to the achieved precision and accuracy, as well as their clinical feasibility.

Operator-Dependency

Up to now, ultrasound imaging is manually guided by physicians and experts and, thus, is heavily user-dependent. Due to all the imaging characteristics and the considerably large influence of acquisition parameters on the resulting image quality, achieving a low intra and inter-operator-dependency remains as a major challenge for freehand 3D+t ultrasound systems. In order to account for these effects, either an automatic optimization of the acquisition parameters, or alternatively a fixation of scanning protocols has to be considered on the one hand. On the other hand, ultrasound imaging requires extensive training of the operator, which is why an additional feedback should be given to physicians during US guidance. Alternatively, a (semi)-automatic acquisition process needs to be taken into consideration.

Clinical Integration

Besides an improved accuracy, the practical applicability and usability of introduced methods remains a key challenge in all ultrasound-related methods. Given the support of ECG in most of today's ultrasound devices for example, the comparably high additional effort, *i.e.* the placement of several electrodes on the patient's skin, prevents this technology from being applied more often. The acceptance of technologies with a more complicated acquisition setup or protocol usually depends on the gained diagnostic value or the reduced examination costs, *e.g.* due to subsequent examinations becoming superfluous.

Thus, technologies providing additional diagnostic information or precision, while adding minimal complexity in terms of the clinical setup will become accepted more easily. This is of special importance for screening applications or initial diagnosis, where the available examination time is limited, and thus, additional practical restrictions for an examination comprise a significant impact to diagnostic costs.

Sparse sampling

Today's freehand 3D ultrasound systems imply the acquisition of individual 2D images and thus suffer from the aforementioned trade-off between the temporal and the spatial resolution. As a consequence of this sparse sampling, additional challenges are imposed for the interpolation of the 3D+t data. Even for a potential integration of matrix-array transducers in future freehand systems, sparse sampling may be inevitable in image regions, where the transducer is moved. Thus, data sparsity will probably remain as a main challenge also in future technology platforms.

Data Visualization and Processing

Based on the acquisition of 3D+t information, processing and especially visualization of acquired data in 3D+t is a demanding task. Mainly due to the high amount of data, high computational requirements need to be imposed in order to allow for fast and intuitive processing for different applications. In this sense, additional methods for dynamic and adaptive sub-sampling strategies have to be incorporated for optimal data processing. Furthermore, new visualization methods have to be developed as well, as a volumetric dataset may have a differing appearance in the temporal domain. As an example, a focus has to be put onto the visualization of changing structures over time, *i.e.* vessel dynamics, while static structures might be less important for a diagnosis.

2.4 Related Work

Based on the general concepts of freehand ultrasound, related work can be categorized into i) methods without consideration of temporal information, ii) systems utilizing secondary devices to retrieve such information, and iii) approaches extracting temporal information directly from the acquired image data.

Neglecting Temporal Information

Due to its simplicity, time-information is even today not commonly considered for 3D freehand ultrasound. With respect to systems presented in the early 2000s [38], basic concepts remained identical up to now, such that a regular 2D ultrasound system is usually connected to a tracking device in order to acquire pose information for the maneuvered transducers. As an alternative to tracking systems, some 3D approaches are capable of steering/moving the

arrays mechanically, *e.g.* by stepper motors. In recent works it was shown that by using such systems, the progression of atherosclerosis in form of plaque evaluation can be monitored successfully [89, 136]. For quasi inelastic structures such as plaques, the assumption of a static structure subject to periodical movements obviously seems to be more appropriate. For application areas where pulsation plays a minor role, such as bone traumatology, the anatomy is entirely static and thus triggering (gating), or additional time information is not necessary. As soon as changes are induced by breathing or pulsation however, neglecting the dynamic behavior can hamper subsequent processing and quantification steps. Since such applications are generally characterized by higher intra- and inter-observer variability, additional pulse-phase information can be used to reduce this variability, *e.g.* for plaque volume measurements [28]. In case of intravascular ultrasound, several works also considered the effect of cardiac pulsation for volume quantification, showing that volume estimates are affected by coronary pulsation without respective pulse-phase gating, *e.g.* [134].

External Sensors Providing Temporal Information

As a consequence of the limitations given by discarding temporal information completely, gating methods for compensating cardiac pulsation have been introduced for several systems. The most wide-spread technology is ultrasound-gating by means of Electro-Cardiograms (ECG) acquiring ultrasound images only for a given time point during the cardiac cycle. ECG-triggered ultrasound acquisition is by now integrated in most commercially available systems, with a focus on the cardiac and intravascular area [10], where a first research in the field was already conducted in the late 1960s [149]. Many freehand ultrasound systems in literature enable the storage of ECG information for certain applications, facilitating retrospective gating [6]. For freehand ultrasound, breathing motion can also be acquired by placing additional tracking sensors on the patient's chest in order to directly acquire signals of chest movement as an indicator for breathing phases. For this application, ultrasound was also utilized directly to perform estimates of cardiac motion, and results have been evaluated within the field of biomechanical simulations [5] as well as gated radiotherapy [70]. With respect to cardiac pulsation and the broad availability of ECG systems, their utilization is still not widely accepted in clinical practice, as the placement of multiple electrodes with proper skin-contact is very time consuming and cumbersome. Thus, it is of high practical value to develop techniques which do not impose a significant overhead to the clinical workflow, but still achieve an accurate diagnosis when the placement of multiple electrodes is not feasible in the clinical routine.

Image-Based Techniques

Restrictions due to the practical usability and the integration into the clinical workflow are the main reasons, why many researchers are aiming at developing fully image-based methods for the determination of phase information. Among these methods, early attempts directly utilized the gray-scale data over

time within a selected region of interest to determine pulse-phase curves [133], or extracted pulse information from Doppler acquisitions for the gating of MRI sequences [118]. Others tried to extract secondary signals such as diameter or area curves over time and performed temporal filtering of these signals [48], or even used a second ultrasound device in order to record pulse phase information via pulsed-wave flow curves [29]. Moreover, the tracking of certain diaphragm features over time was employed to detect breathing phases automatically [152]. Alternatively, independent component analysis on sequences of contrast-enhanced ultrasound images was also used to retrieve pulse components [114]. Finally, recent methods also looked into the utilization of manifold learning to estimate breathing phases from 3D wobbler ultrasound acquisitions [140].

Concerning the interpolation of acquired spatio-temporal information with respect to a regular 3D+t representation, most systems focus on single time points without a separate subsequent temporal analysis. Only a few methods tried to reconstruct full 3D+t -information from ultrasound imagery so far. For instance, [13] included the concept of normalized-convolution in order to reconstruct 3D+t ultrasound data of the heart from images acquired with a fast-rotating probe. For the same data, another approach showed improved reconstruction quality [95] in comparison to the original method, utilizing all available spatio-temporal information for the determination of respective spline interpolation components in order to perform full compounding of datasets in the 3D+t domain.

2.5 Contributions

2.5.1 Vascular 3D+t Freehand Ultrasound using Correlation of Doppler and Pulse-Oximetry Data (IPCAI 2014)

Due to the potential applications for an analysis of arterial expansion and compression throughout cardiac phases, estimates of vessel dynamics from 3D+t data could facilitate early-detection and screening applications leading to a stronger clinical integration of these methods. For the acquisition of 3D+t ultrasound data, image-based methods for detecting cardiac pulsation provide promising results for healthy conditions. However, underlying assumptions of a constant pulse frequency or steady ultrasound probes are often not valid in practice. As explained before, ECG-based gating methods suffer from limited clinical usability, because several electrodes have to be placed on the patient's chest, resulting in a both time-consuming and error-prone setup.

In order to overcome such limitations, in [64] a method for the acquisition and reconstruction of 3D+t data from freehand ultrasound information is proposed, *cf.* appendix A. Instead of only relying on the acquired image information, a pulse-oximetry sensor is used for recording information about the total blood volume (in the fingertip) over cardiac cycles. Pulse-oximetry provides a convenient alternative to ECG monitoring; only a single clip needs to be attached to one of the patient's fingers, allowing for a monitoring of pulsation, pulse frequency, and oxygen saturation. These signals directly

correlate with vessel expansion and compression and thus give an indirect measure of cardiac pulsation. Due to its comparably low usability overhead, these sensors are used as a standard tool for patient monitoring in clinics to detect acute events, *e.g.* while patients are transported to different stations or acquisition sites. However, pulse-oximetry signals may face a temporal delay from the location of measurement (finger) to the anatomical region where the ultrasound data is acquired. To overcome this varying temporal lag, a time-calibration step is performed on a per-record basis, enabling direct correlation of the ultrasound imaging data to the retrieved pulse phase values. With respect to a clinical application in vascular diagnosis, Color-Coded Duplex ultrasound is used as a standard tool for the evaluation of vascular blood flow, and color-coded flow velocities are superimposed on top of normal B-mode images. Consequently, both B-mode and flow information is presented simultaneously in this scenario, facilitating the direct correlation of the flow information to the acquired pulse-oximetry signals. Recalling the theoretic principle for pulsed-waved flow estimation in ultrasound in Sec. 1.2.4, the color-coded signals correspond to velocities of scatterers within the blood. Pulse-oximetry measures the amount of oxygenated blood over time by evaluating the absorption of light through the skin. As the observed signals are quasi-static between distinct periods of cardiac pulsation, changes of pulse-oximetry signals in short periods are modeling the total volume of oxygenated blood absorbing some of the light emitted from the pulse-oximetry diode. The volumetric flow rate can thus be approximated by

$$p'_k = \frac{p_k - p_{k-1}}{\partial k}, \tag{2.2}$$

where ∂k denotes the sampling time interval and p_k the amount of oxiginated blood passing through a fixed volume with surface area A during ∂k, *i.e.*

$$p_k \approx \int_A v(t)\, dA \cdot \partial k. \tag{2.3}$$

For the CCD data, an arterial flow signal d_k is extracted from all non-zero flow values present in the ultrasound data. Then, for every patient acquisition, the cross-correlation of the signals is evaluated in order to estimate the offset between both signals

$$o_{d\to p} = \arg\max_l \sum_{k=0}^{K-l-1} d_{k+l} * p'_k. \tag{2.4}$$

In this view, the time offset $o_{d\to p}$ comprises the processing times for ultrasound and pulse-oximetry data, the transmission lag for all information as well as varying pulse wave delays from the finger-tip to the site of the ultrasound acquisition. Using the determined offset values, a normalized pulse phase signal, representing the phase of vessel expansion and compression, can then be extracted from the calibrated pulse signals. This allows for a subsequent 3D+t compounding of ultrasound image information with respect to desired phases of vessel expansion and compression, utilizing i) the time phase information provided by pulse-oximetry, and ii) the resolution of the natively acquired

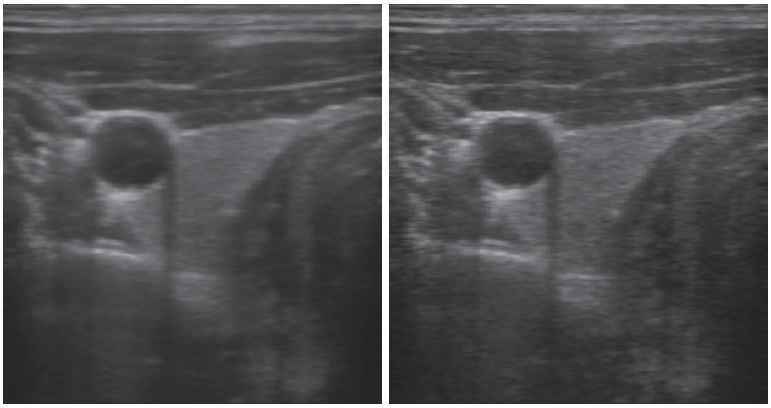

Figure 2.6: Impact of resolution-preserving compounding using temporal information. Discarding pulse phase information results in blurred images with fuzzy boundaries (left), while pulse-oximetry signals incorporated into the compounding preserve the image content for a given time phase (right).

ultrasound data by modeling the beam shape and size along each acquired scanline. In detail, compounding is performed as a two-step process, where first all samples contributing to a target voxel position in the 3D+t domain are selected. This selection includes the distance of the ultrasound samples to the voxel position with respect to the native resolution of the ultrasonic beam dimensions. The voxel intensity values are then reconstructed from all collected samples by using a Gaussian weighting of the samples according to their distances to the target position in the 3D+t domain.

Resulting 3D+t volume information preserves more details in the images compared to today's state of the art, neglecting temporal information for ultrasound compounding, *cf.* Fig. 2.6. Furthermore, by reconstructing information for distinct time steps, dynamics of vessels during expansion and compression can be visualized and studied. For the corresponding full publication, the reader is referred to appendix A.

3

Modality-Specific Modeling for Information Processing in Vascular Ultrasound

While the last chapter focused on an accurate and reliable acquisition and reconstruction of 3D+t data, approaches for incorporating domain-specific models as well as knowledge about the image formation process into the processing chain are the main interest of this chapter. These are aiming at overcoming the limitations of today's methods in order to provide additional diagnostic value.

3.1 Problem Definition and Motivation

The landscape of ultrasound processing methods dealing with vascular applications is extensive, where the major areas are image segmentation, registration, and extraction of quantitative information from the acquired medical data. The general motivation for these approaches can be roughly characterized in methods

1. augmenting acquired information by further image processing, such that these steps can benefit from the processed data.

2. extracting additional diagnostic information directly from the data, *e.g.* in the classical sense of computer vision.

3. improving the visualization for physicians and medical experts.

While this categorization is intuitive and often considered as a sequential pipeline in commercial solutions (consisting of submodules for each part), it is vague at the same time from a technological point of view, because the aforementioned categories are not disjoint. As such, data enrichment is usually performed first, followed by an extraction of quantitative information and its visualization to the expert performing the diagnosis.

Data Enrichment

The augmentation of data with the help of image processing methods is commonly considered as data post-processing, with typical sub-categories being distortion-correction or noise-reduction. The underlying assumption of these methods is that the image data is subject to the imperfections of the image formation process, such as distortions caused by varying probe pressure, ultrasound artifacts, electronic noise, or quantization artifacts. Thus, the ideal image I is altered by some kind of distortion, and only the distorted image I' can be observed by the sensor, *i.e.* the ultrasound probe:

$$I' = g \circ I, \tag{3.1}$$

where g models the distortion. The goal is then to recover the original image data by reversing g, in order to remove the alterations introduced by the distortions. A common example for post-processing is the removal of noise

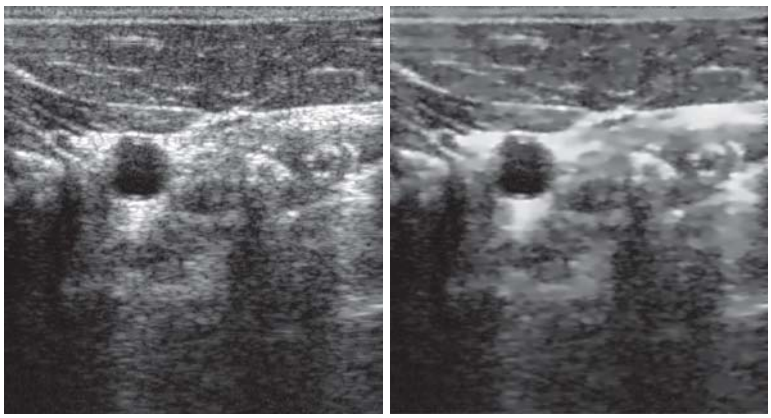

Figure 3.1: An example for ultrasound speckle removal using anisotropic diffusion filtering [2] (right) shows suppressed speckle and noise while the main image structures are preserved. In contrast to this, the raw input image (left) shows significant noise and speckle across the image.

from the data, *e.g.* by Gaussian or Speckle filtering. In case of noise removal for ultrasound data, g refers to a combination of additive and multiplicative noise, resulting in the observed intensity $I'_x = I_x \cdot \eta_m + \eta_a$ for an image point x, with η_m, η_a being the multiplicative and additive noise terms. While the additive terms can be removed by classical noise-reduction methods, multiplicative terms usually refer to the task of Speckle reduction, where the main goal is to remove diffuse scattering from the image data while preserving the anatomical information such as small interfaces and other image features.

Besides the removal of noise and speckle, further post-processing methods are used in order to improve contrast, sharpness, or image quality in general. Thereby, the necessity for different approaches and their parametrization varies based on the final goals in terms of data processing. For instance, while a subsequent visualization of data may be improved by a sharp and crisp presentation of the image data, automatic processing methods could be

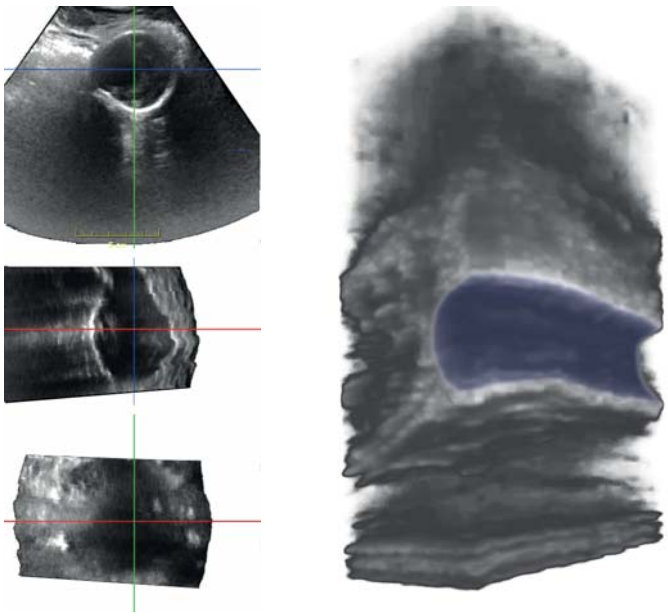

Figure 3.2: Left: Multiplanar reconstruction of an aortic aneurysm, showing axial, sagittal and coronal views. Right: Shaded 3D-visualization of a common carotid artery (manually highlight in blue).

hampered by such fine-scale details. In such cases a coarse representation could be sometimes favorable.

Quantification and Visualization

The latter two information processing categories, namely the extraction of quantitative information and data visualization, serve for the goal of helping the physician or the medical expert in performing a more accurate and reliable diagnosis. Although the respective goals are similar, the employed concepts often vary significantly for both categories. On the one hand, visualization facilitates a direct interaction with the data, such that the expert can retrieve added value. Quantification, on the other hand, utilizes processing tools in order to retrieve measurable values for given indications, which could for example be the volume of an aneurysm or the elasticity of a tumor lesion.

In the area of medical visualization, multiplanar reconstruction (MPR), showing three orthogonal cuts through a 3D volume, and direct rendering of the volumetric data still belong to the most frequently used visualization techniques (*cf.* Fig. 3.2), because they provide a fast anatomical overview of structures. Besides these rather basic visualization techniques, which were mostly adapted from other imaging domains, additional information can be included into visualization approaches in order to enable enhanced visibility of the structures of interest within the acquire data. In this context, segmented objects can be blended with the 3D intensity data, or combined directly to provide improved 3D visualization, *cf.* [120]. As a consequence, modern

visualization methods often require additional information as a prerequisite for visualization, *e.g.* geometric primitives, segmented organs, or a registered set of other images. Based on this additional input, they then allow the medical experts to compose more intuitive representations of the data, facilitating improved diagnosis. In summary, we can identify general processing methods, which are used for both quantification and visualization of image data.

Regarding the processing and extraction of quantitative information, there is a large body of literature available, with image segmentation and registration probably being the most prominent examples for such processing approaches. For the segmentation of an object in a medical image, the interest lies in the delineation of the object boundaries, such as contours in 2D or surfaces in 3D, in order to enable a visualization of the structure and an extraction of quantitative measures such as its volume or diameter. As opposed to this, the main challenge for image or model-based registration lies in aligning two or multiple sets of points, shapes, or images to each other, facilitating the overlay and detection of certain structures in the corresponding sets of data. More formally, the goal of registration is to find a transformation τ mapping corresponding points x, x' into each other, *i.e.* $x' = \tau x$. Thereby, transformation models can be categorized with respect to the type of mapping (rigid, affine, projective, or deformable) the dimensionality (2D-2D, 2D-3D, 3D-3D), or their spatial sampling, *i.e.* dense or sparse. This not only enables an overlay of multiple images for one patient, but also an analysis of the progression of anatomical regions over time. By image registration, complementary information can be further combined for visualization, often referred to as image fusion. For both fields described, a multitude of approaches was presented in the past, where [101] gives a good overview of segmentation methods for ultrasound imaging, and [157] for the field of medical image registration.

3.2 Modality-Specific Modeling for Improved Ultrasound Processing

In the area of medical image processing, the majority of methods in literature was developed with a focus on tomographic modalities such as CT and MRI, while an application to (3D) ultrasound imaging was often not considered. As a result of these developments, methods were directly applied to US imaging without modification as such, often yielding unsatisfactory results. Instead, a modality-specific modeling, inspired by both imaging physics and physiology would lead to an improved performance of general processing methods, such that specific properties could be used in order to improve the final outcome. At this point, we recall the modeling categories, namely physical and physiological modeling, as introduced in Sec. 1.1.

Physical Modeling

Physical modeling tries to account for all properties and effects during the modality-specific image formation process. Thereby, the main motivation for

physical modeling is to account for the characteristics of the different image modalities. In the case of ultrasound, such properties are, among others, the specific acoustic attenuation, the anisotropic nature of ultrasound due to the directionality of the beam as well as the formation of ultrasonic speckle. The image acquisition properties and processes can differ fundamentally across modalities however, which becomes obvious when imaging the same anatomical structures. When comparing CT, MRI, and ultrasound for example, CT reconstructs tissue attenuation given by Hounsfield units, while MRI uses the relaxation of hydrogen atoms, and ultrasound the differences in acoustic impedance as basic physical imaging properties. As a consequence of the differences in image acquisitions, resulting images of the same anatomy can be used to obtain complementary information about the target structure, which is often utilized in clinical routine.

With regard to the detailed image formation process of sonography, the specific image appearance and its properties include for example appropriate noise and distortion models as well as modeling of ultrasonic speckle as Rayleigh scattering. Furthermore, information about the attenuation of ultrasonic waves for deeper tissue regions can improve the quality for generic processing methods, as due to the loss of wave energy, the confidence of imaged features decreases in heterogeneous tissue with increasing distance to the transducer. Finally, modeling can also incorporate knowledge about the specific parameters used for image acquisition, *i.e.* the choice of the ultrasound transducer geometry, its layout, and the emitted ultrasonic wave front. This includes again wave and beam modeling, which influence not only the overall image appearance and confidences, but also the image resolution as a function of the penetration depth. Moreover, the focal length and the frequency of emitted waves can be used effectively to model a full ultrasound acquisition performed by a physician.

Besides the characteristics described above, physical modeling can also be used to address further parameters and effects, such as the direct interaction of ultrasonic waves with solids and tissues. This refers to ultrasound simulation, where, based on known physical parameters and target material properties, the appearance of a resulting image can be simulated fully. In this context, however, also information about the target tissue is required for simulation, which is why usually information given by other sources (*e.g.* CT, histology) is used as a basis to simulate data, which is directly leading to physiological modeling approaches.

Physiological Modeling

Physiological modeling uses knowledge about the target structures (*e.g.* organs, vessels) in order to model the anticipated shape or appearance of the respective structures in the image data. While physical modeling differs among imaging modalities, physiological modeling can be applied in a similar way to different modalities, as the biological and physiological principles of the imaged objects do not depend on the modality. In this sense, knowledge about organs and their dynamic behavior, or whole anatomical regions can be related to the

cognition of human operators, as outlined in Sec. 1.1.

More precisely, physiological modeling utilizes prior knowledge about the construction and composition of anatomical structures as well as their function for geometric and deformable models. A vessel for example can be represented as a tubular structure with bifurcations and a varying diameter along the vessel. Similarly, assuming a deformable model, the tubular structure would be compressed over time due to cardiac pulsation, leading to phases of minimal and maximal expansion. In daily routine, such information is used by the physicians in order to find and analyze target regions of interest in the image data. By considering multiple patients for the creation of such models, statistical models of different vascular structures and anatomical regions can also be computed. More precisely, the vessel diameter and its dynamic behavior over time will heavily depend on both the anatomy and the time of observation, while the underlying assumption of a tubular structure with narrower/wider regions and bifurcations can be used to model all vessels in a uniform fashion.

Beyond geometrical and deformable models, information about human physiology can allow for a compensation of dynamical changes due to motion. For the example of flow estimation with ultrasound, the changes of blood flow velocities over cardiac cycles can be correlated with changes in the patient's condition, such as a potential malfunction of the heart, or a localized damage of the vessel (stenosis, aneurysm) respectively. By comparing observed information with respect to their accordance to previously generated (dynamic) models, diseases and malfunctions can be detected directly, or confidence values can be derived. Furthermore, not only the dynamics of single objects and organs, but also their relation to each other can be modeled. This includes the coupling of adjacent organs, as well as their dynamic behavior. In such a scenario, whole anatomical regions such as the abdomen can be modeled, consisting of several different structures including the arteries, the liver, kidneys, the lung and the like. Today, complex models incorporating biological, mechanical and dynamic properties for certain anatomies are summarized as biomechanical models and enable a full simulation of single and multi-organ behavior.

3.3 Challenges

While the points described above indicate different methods and possibilities for an integration of physical and physiological models into data processing, several challenges are still evident in this context. It has to be noted that the decision on the type and extent of modeling heavily depends on the specific goals and applications.

Quality of Ultrasound Data

Most importantly, proper modeling always requires a certain level of quality of the input data. While the main goal for physical models is to compensate for a degenerated quality of the acquisition, variations among different examiners (operator-dependency) may influence the performance heavily and are difficult to model. Furthermore, any type of modeling usually poses high requirements

in terms of additional meta-information for each recording. These include among others the acquisition protocol with its parameters, the trajectory associated to the sweep or the tissue types. For an appropriate modeling of ultrasound waves and beam profiles in homogeneous tissue, for instance, a detailed knowledge about the used imaging parameters such as transducer properties, transmit and sampling frequency, and focal points may be required. Consequently, acquisitions and recording of data has to be performed carefully, ensuring that the required information is collected in sufficient quality.

Dependency on Acquisition Settings

In addition to the quality of the acquired data, varying acquisition settings may have an impact on the modeling results. For the example given above, a change in parameters would result in different beam profiles and consequently in changed image appearance, influencing the visibility of noise and ultrasonic speckle. Thus, the dependency on acquisition settings has to be taken into account throughout all processing steps, either by generating models parametrized based on those, or restricting the modeling to a specified combination of imaging and acquisition parameters.

Model Complexity

When comparing highly realistic models to basic ones, a balance of accuracy and complexity versus runtime has to be found. While for the example of ultrasound image simulation complex models enable realistic estimations, the computation of a single image can easily take up to several hours, which is simply not feasible for an incorporation into real-time scenarios. On the other hand, too simplistic models may not be suitable for accounting for a varying image quality and the presence of noise. As a consequence, the selection of an appropriate model has to be made with care and with a focus on the desired balance between complexity and runtime.

Quality and Quantity of Available Data

Similar to the runtime, the quantity of available data for constructing models impacts the (possible) choice of models. While basic anatomical priors can be incorporated in many approaches, complex biomechanical or deformable models often require a considerable amount of information for training or parametrization. Furthermore, the acquisition of geometric models as well as the annotation of respective meta-data usually requires a considerable amount of manual interaction or input, restricting the generation of high amounts of datasets in practice. While this point is certainly less evident for leading companies in the field of medical technology, which have access to databases of several thousands of patients, the non-commercial generation of such a collection remains challenging. In addition to this, it has to be noted that it is usually much easier to obtain data exhibiting pathologies than data from healthy subjects. This can both cause a bias in the generated models and hamper the generation of these models as such, because the variability of

pathological organs or structures is in general higher than the variability of healthy collections.

Model Validation

Proving the accuracy and robustness of the developed methods remains a further challenge, especially with respect to other approaches. The reason for this fact is that the concept of reproducible research has not been fully established yet in the area of computer science, *e.g.* by providing source code, reference implementations, or ground truth data. To enable a validation using ground truth information, manual segmentation of objects in a series of images may be required in many cases. Alternatively, computationally generated phantom datasets can be used for evaluation. However, the quality and realism of such phantoms suffers from certain limitations such as imperfect material properties, or the lack of dynamic behavior. In addition to the availability of the evaluation data, choices for appropriate validation strategies have to be made. In practice, a combination of both the comparisons to computational phantoms and a ground truth validation seems to provide a good strategy for many scenarios.

3.4 Related Work

Similar to the last section, we differentiate related work according to physical as well as physiological models. While the areas are partially overlapping, for physical models the emphasis lies on the utilization of ultrasound-specific knowledge, while physiological models focus on incorporating physiological priors into the processing chain.

Physical Modeling

Detailed incorporation of imaging parameters with specific corrective processing steps started in the early 2000s, when expected intensity homogeneities due to changes in attenuation in different tissue types were used for the first time in order to improve segmentation results [150] in ultrasound imaging.

While intensity homogeneity can be observed in acquired ultrasound images, the reasons for this effect are mainly due to ultrasound attenuation in tissue as well as modality-specific peculiarities. Several approaches have focused on the estimation of ultrasound attenuation for a reduction of distortions due to attenuation and enhancement artifacts [131]. More recently, a full beam shape modeling was combined with the estimation of ultrasound backscattering statistics to automatically detect shadows from acoustic interfaces, such as bones [62]. With the similar goal of removing attenuation artifacts in ultrasound images, advanced models for attenuation estimation using partial differential equations to compensate for those artifacts were presented in [154]. As an alternative approach, ultrasound transmission-reflection was also used to directly reconstruct attenuation values from a series of multi-view ultrasound acquisitions [138], enabling both the visualization of attenuation and the

presentation of simulated CT data from these values to the end-user. Moreover, the quality of ultrasound images was evaluated by means of machine learning, allowing for an automatic adjustment of acquisition parameters in an on-line fashion [35].

Beside various research efforts in order to compensate and correct for attenuation and artifacts in imaging, a second trend can be observed with the goal of incorporating more information (specific to each imaging modality) into further processing steps. Thereby, the utilized information is used for both data enrichment and further processing with the goal of improved quality, performance and accuracy of the respective methods. More recently, Rayleigh models targeted to ultrasound scattering [15] as well as general ultrasonic speckle distributions [123] have been included into segmentation methods for improving performance and robustness. Concerning the registration of CT and ultrasound data, ultrasonic reflection-transmission as a basic imaging-principle was also used to simulate US images from CT, facilitating direct registration of both modalities [146]. Besides these speckle models, confidence maps for ultrasound have been presented recently, yielding an estimate of the information-certainty provided by each ultrasound sample [75]. As such, confidence values are estimated by incorporating a Beer-Lambert attenuation model with the image intensity information in order to locally detect shadowing and artifacts.

Physiological Modeling

Within the area of physiological modeling for vascular applications, geometric models are used most-frequently for ultrasound imaging. With a focus on vessel detection and tracking, several methods used geometric assumptions such as a circular and ellipsoidal appearance of vessel cross-sections for their detection [107, 108, 143, 144, 81, 80], relying on the general assumption of tubularity discussed above. As an extension to basic geometrical constraints, statistical shape models for various ultrasound applications have been proposed in literature [101], and partially also specific adaptions to the ultrasonic imaging principles have been included to improve processing outcomes [83, 123].

While the majority of geometric and deformable models is directly used within the respective processing approaches including segmentation and registration, biomechanical models combine geometrical information of the vessels with dynamic changes over time (*i.e.* cardiac pulsation) and are often used for the direct simulation of vascular structures and their behavior. In this field, various models are available for the simulation of pulsatile blood flow in arteries [69, 141], which can directly be mapped to ultrasound flow velocities. To model the propagation of fluids in vessels in a fully realistic fashion, the Navier-Stokes equations have been integrated with appropriate boundary conditions in various methodological setups [103, 156, 129]. Thereby, the fluid dynamics simulations were partially augmented by fluid-structure interactions in order to model the dynamic changes of the vessel wall interacting with the pulsatile blood flow [129]. Furthermore, there have been efforts for incorporating biomechanical models directly into the registration of CT and ultrasound

data [51] in the case of spine. Targeted to vascular applications, extensive biomechanical models were finally utilized to directly improve the quality and accuracy of ultrasound blood flow imaging as such [130, 128].

3.5 Contributions

In the following, all contributions with respect to modality-specific modeling in vascular ultrasound are described. For the detailed versions of the respective contributions, the reader is referred to appendices B to D.

3.5.1 A Quadratic Energy Minimization Framework for Signal Loss Estimation from Arbitrarily Sampled Ultrasound Data (MICCAI 2014)

Incorporating information about the image acquisition process, the ultrasound probe and machine settings can improve image processing significantly, *cf.* Sec. 3.2. As described in [75], ultrasound confidence maps are modeling ultrasonic attenuation and imaging artifacts, which can be useful for further processing as well as visualization of ultrasound confidence values to the physicians. This approach is, however, limited to 2D images, while certain applications demand for 3D information to be incorporated into processing. In order to enable similar estimations in 3D, an approach which directly takes the acquisition process into account is presented in [65]. The main novelty of this approach is two-fold: Firstly, a framework for the modeling of general quadratic energy minimization problems on arbitrary 3D trajectories is presented, which does not require interpolation with respect to a regular grid (compounding-free). Secondly, an extension of [75] for arbitrary geometries is described, enabling the retrieval of confidence values not only for 2D images, but for full acquisitions with a support for arbitrary image geometries such as linear, curvilinear or 3D trajectories.

The structure of a general energy-minimization problem, a re-occurring problem in image processing, is given by

$$E(x) = \frac{1}{2}x^T Ax - x^T b, \tag{3.2}$$

where x is the state vector, A the system matrix, and b the boundary conditions and the source term for a given problem. With respect to the minimization of such problems, current methods usually assume a regular grid, *i.e.* the ultrasound data lying on a 3D volume reconstructed with respect to a rectangular lattice [54, 75]. In practice, however, prior compounding of data may impair the image quality or even lead to a loss of information [110]. In [65], a graph is thus constructed directly from the acquired ultrasound samples in 3D space instead, assuming individual US scanlines as the native form of sampling. As images are generated from a series of individual scanlines (acquired subsequently over time) for the majority of ultrasound systems, such an approach can consequently be used to model any given ultrasound acquisition.

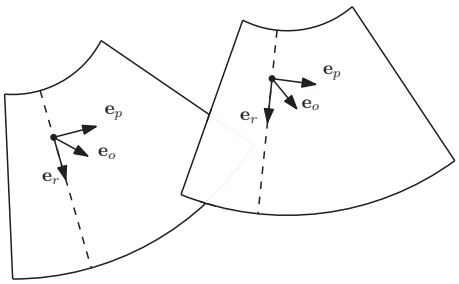

Figure 3.3: Single ultrasound images are modeled as sets of several rays, where neighbors are searched in directions $\mathbf{e}_p, \mathbf{e}_o$ orthogonal to the ray direction $\mathbf{e}_r$

For the graph construction from a whole set of rays, a nearest neighbor search is carried out in orthogonal directions to each ray, such that the six nearest neighbors can be found in the directions $\mathbf{e}_r, \mathbf{e}_p, \mathbf{e}_o \in \mathbb{R}^3$, cf. Fig. 3.3. Based on the selected neighbors for each sample, a fully connected but unstructured graph is assembled, for which directional derivatives $\nabla_\xi p_i := p_\xi - p_i$ can be defined as the difference between a target sample potential p_i and one of its six neighboring potentials p_ξ. By including a potential-dependent activation and update scheme, one can solve energy minimization problems on a directed graph in a descent-like fashion. The activation for an edge connecting two samples is controlled by the potential difference of adjacent samples $\mathbf{1}(p_i > p_\xi) = 1$, if $p_i > p_\xi$, and $\mathbf{1}(p_i > p_\xi) = 0$, resulting in the following update scheme:

$$\Delta p_i = \sum_{\xi \in \mathfrak{N}_i} \left[\mathbf{1}(p_i > p_\xi) w_{i\xi} + \mathbf{1}(p_i \leq p_\xi) w_{\xi i} \right] \nabla_\xi p_i. \tag{3.3}$$

As the computation of Δp_i is only dependent on the local neighborhood, a parallel implementation on the GPU allows for an efficient optimization directly on the assembled graph.

For applying the optimization framework to the task of confidence estimation based on the presented framework, only the weighting function for each graph connection has to be adapted and the boundary conditions have to be set accordingly. More precisely, the angle between two rays determines whether their imaged samples correlate to each other or show complementary information. To account for this ultrasound-specific pecularity, a 3D weighting scheme is presented, incorporating sample intensities, their distance, as well as the angle between the respective rays:

$$w_{\xi i} = exp\left[- \left(\frac{|I_{\theta^{-1}(\xi)} - I_{\theta^{-1}(i)}|}{\sigma} + \gamma(|\mathbf{x}_{\theta^{-1}(\xi)} - \mathbf{x}_{\theta^{-1}(i)}|(1 - \langle \mathbf{e_r}^\xi, \mathbf{e_r}^i \rangle) \right) \right]. \tag{3.4}$$

Thus, the optimization problem yields confidence values for each sample of an arbitrary (3D) acquisition directly in the native sampling space. In comparison to 2D-based methods, our results show improved consistency and homogeneity along the trajectories, also facilitating the application of the proposed framework to other, physically-inspired processing approaches.

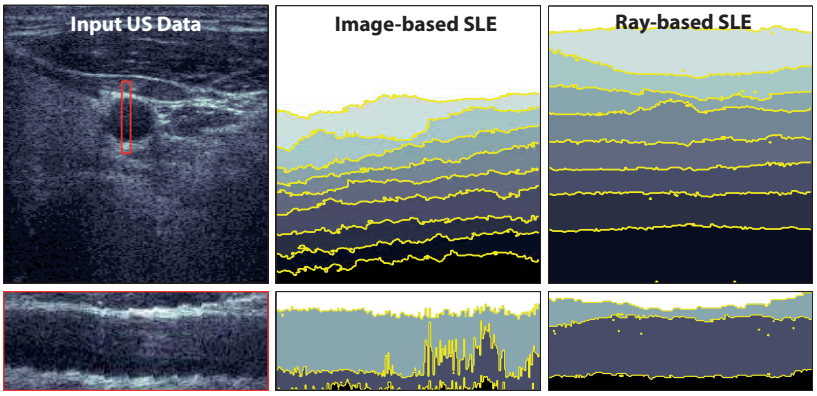

Figure 3.4: **Loss Estimates for Carotid Ultrasound** Transverse (top) and longitudinal (bottom) cuts through a 3D acquisition for [75] (middle) compared to the presented method (right) shows much more consistency along the trajectory by using full 3D information.

The publication as printed in appendix B gives additional information with a detailed description of the optimization problems and strategies, as well as results for two different application fields, namely bone ultrasound and vascular ultrasound.

3.5.2 Multi-Scale Tubular Structure Detection in Ultrasound Imaging (TMI 2014)

Especially with the goal of a quantitative analysis in vascular ultrasound, automatic processing of data, including vessel segmentation, still remains challenging. For an automatic detection of vessels in 2D and 3D ultrasound images, several methods have been presented based on the well-known vesselness filter [42], including a first adaption to ultrasound imagery [142]. In [63] this approach is extended with respect to a full adaption to ultrasound images by means of presenting a generalized method to design second-order derivative filters targeted at specific image structures. Furthermore, general strategies for adapting filter-based techniques to the special appearance of ultrasound images are proposed.

For the classical approach of using Hessian-based techniques to detect vessel-like structures, the second order derivative is equal to the graph Laplacian for the discrete setting in 1D

$$\frac{\partial^2}{\partial x^2} g(x) = \Delta g, \tag{3.5}$$

and serves as a ridge-detector. As the goal is an accurate structural modeling of the target by the second order derivative, filters can be designed directly by prescribing these. In detail, this is realized by defining the desired second order derivate function values as a discrete vector, for which the equality to the graph Laplacian can be used to iteratively optimize for $g(x)$. Using this general

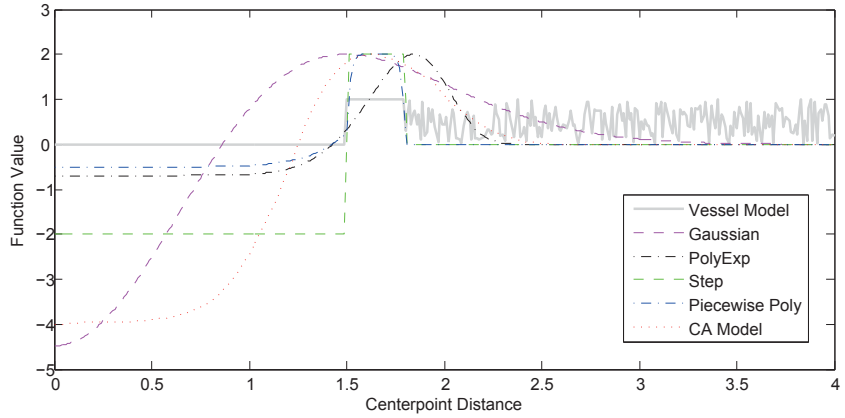

Figure 3.5: Second derivatives for a Gaussian, the kernel proposed in [142] (PolyExp), and our presented method (Piecewise Poly), with the gray line representing an idealized vessel model in ultrasound.

approach, arbitrary structures and shapes can be detected by constructing appropriate derivatives and solving for $g(x)$.

In addition to this generative filter-design method, additional physics-based adaptions are included into the vessel detection method in order to improve the performance and robustness with respect to ultrasound imaging. This includes a compensation for the decaying image confidence caused by the decreasing ultrasound beam energy for deeper image regions. To do so, the respective factor for a discrimination between plate-like and line-like features using the eigenvalues of the Hessian matrix in the images is modified, such that confidence eigenvalues are used instead, being more robust with respect to noise and artifacts. Besides the compensation for ultrasound confidence, the beam-directionality is modeled within the presented work as well. In general, observed gradients in axial directions are more prominent in ultrasound images compared to lateral (and elevational) ones. Based on this assumption, the eigenvector belonging to the highest eigenvalue of the Hessian matrix should point into the beam direction for vessel-like structures. Consequently, the dot product of beam direction and the mentioned eigenvector can be used as an additional factor for vesselness estimation.

The results for this combined method show an improved separation of vessel points from the background compared to basic vesselness implementations and single adaptions, *cf.* Fig. 3.6.

A more thorough explanation of the described components, including a detailed evaluation and additional qualitative results for comparison can be found in the main publication in appendix C.

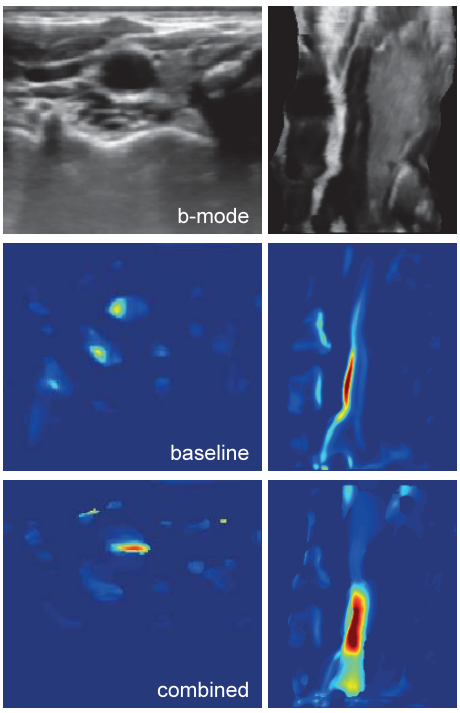

Figure 3.6: Comparison of the proposed method to the classical vesselness filter for a scan of the carotid artery.

3.5.3 3D Velocity Field and Flow Profile Reconstruction from Arbitrarily Sampled Doppler Ultrasound Data (MICCAI 2014)

The reconstruction of 3D flow velocities from multiple freehand Doppler acquisitions can potentially allow for an improved understanding of how changes in local flow behavior in the arteries have an influence on cardiovascular diseases, resulting in a direct impact to diagnostic routines in the future. In order to enable a reconstruction of flow profiles, recent studies have shown combinations of multiple compounded Doppler acquisitions for the estimation of the flow velocities [52].

While these methods focus on the reconstruction of flow profiles from fixed pulse phases, *e.g.* by using ECG-triggered 3D ultrasound acquisitions, [155] presents an approach suitable for the simultaneous reconstruction of flow profiles and their behavior over time. With several 3D Doppler acquisitions from different views and angles to the target structure, a waveform model for blood flow throughout cardiac pulse phases [141] is applied in order to avoid the requirement of triggered acquisitions. Similar to the concept presented in Sec. 3.5.1, the method is compounding-free, such that acquired ultrasound data is processed without requiring a-priori interpolation with respect to a regular grid. Instead, for each sample a 4-tuple consisting of the position $\mathbf{p}$, the ray direction $\mathbf{d}$, the measured Doppler velocity m and normalized pulse phase

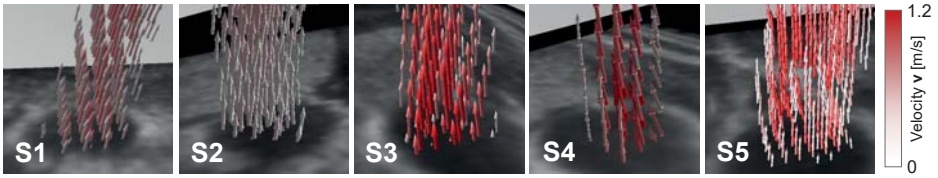

Figure 3.7: Reconstruction for 5 patient records. Shown are the reconstructed velocity fields as an overlay of visualized cross-sectional planes through the arteries.

t is collected for the reconstruction of the flow. For a combined reconstruction of flow velocities and their behavior over time, laminarity of the individual flow direction is assumed, such that only the flow speed can vary over time, while its direction is forced to be constant

$$\mathbf{v}(\mathbf{p}, t) = \varphi(t)\, \mathbf{v}_{max}(\mathbf{p}), \tag{3.6}$$

where $\varphi(t)$ represents the pulsatile flow profile over a cardiac phase. Using the available information for each sample, this results in a cost function depending on a global, relative pulse profile φ and maximum flow $\mathbf{v}$

$$J_{proj}(\mathbf{v}, \varphi) = \sum_{r=1}^{N} \| \varphi(t_r)\, \mathbf{d}_r \cdot \mathbf{v}_{max}(\mathbf{p}_r) - m_r \|_2^2 \qquad \text{s.t.} \quad \max_t |\varphi(t)| = 1, \tag{3.7}$$

where the index r denotes the sample number of the respective quantity. By performing an iterative, alternating optimization for the global pulsatile profile on the one hand, and the respective flow vectors for each resolution cell on the other, both entities can be estimated in a combined fashion. As a reconstruction basis, b-spline grids were used for both the spatial and temporal data sampling, resulting in smooth estimates due to a divergence regularizer enforcing the incompressibility of blood flow.

The manuscript, as shown in appendix D, gives a thorough explanation and discussion of our phantom validation along with a description of the utilized experimental setup and a full explanation of the optimization strategy for a simultaneous reconstruction of flow directions and profiles over time.

4

Conclusion and Outlook

As a conclusion of this dissertation, we finally want to summarize the main contributions and points addressed and use it in order to discuss a possible outlook with respect to the two main fields of 3D+t ultrasound systems and modality-specific modeling for vascular imaging. In this context, a detailed overview of the fundamental principles and physics of ultrasound imaging was provided in the first chapter before focusing on the two separate areas of contributions. This allowed for an understanding of the respective imaging physics and properties as well as important effects, and potential challenges for today's discipline of ultrasound imaging.

Towards 3D+T Freehand Ultrasound

In the second chapter, the field of 3D ultrasound over time was addressed, yielding 3D+t data for processing and visualization. Based on a general problem definition with a focus on different methods for the acquisition of spatio-temporal data with a high quality, freehand and matrix-array systems were described as the two basic approaches to acquire such data. Next, a set of viable clinical application fields was described, and the additional value given by spatio-temporal information was demonstrated, utilizing provided dynamic temporal data. While systems for acquiring 3D+t data are available for some applications, *e.g.* 3D echocardiography, several challenges are evident with regard to a full clinical acceptance, especially concerning their clinical integration, the operator-dependency, as well as the sparsity of resulting data. With respect to an improved acceptance of freehand ultrasound systems for vascular diagnosis, the following contributions towards full 3D+t acquisitions have been introduced:

- A pulse-oximetry sensor for state-of-the art 3D freehand ultrasound systems, avoiding the inconvenient placement of several electrodes by using a single clip attached to one of the patient's fingers, thus facilitating a fast integration into the clinical workflow.

- An automatic correlation of pulse phase data with respect to the ultra-

sound information to enable an individual calibration on a per-record basis exploiting the corresponding signals.

- The reconstruction and visualization of high quality 3D volumetric information over phases of cardiac pulsation (3D+t data).

While the presented methods are a first step towards clinically usable systems, additional analysis regarding the evaluation with different patient groups and pathologies will be required to show the robustness of the developed system. With a broader view in mind, the combination of pulse-phase information could be beneficial for an integration of matrix-array probes with the freehand scanning technique in the future, allowing for cardiac references without requiring ECG systems. Moreover, based on the technological advances as well as increased capabilities for signal processing, the combination of matrix-array probes with accurate tracking, or even a direct extraction of pose information from overlapping volume information will potentially lead to a much higher quality of 3D+t data. In conjunction with additional sensors for pulse-oximetry and breathing, this could ultimately allow for the acquisition of 3D ultrasound information, fully incorporating the dynamic and periodic motions of breathing and cardiac pulsation.

Modality-Specific Modeling for Information Processing in Vascular Ultrasound

In the third chapter, the focus was shifted towards the processing of vascular freehand ultrasound data, utilizing all available domain-specific knowledge. In this context, data enrichment was presented first, followed by visualization and quantification as main goals of this domain, before the possibilities for incorporating specific knowledge were described in detail. With physical and physiological models, two categories including the specific knowledge about the physical processes for the imaging-domain, as well as physiological processes and relations for specific structures were presented. While the utilization of domain-specific knowledge provides high potential, challenges are imposed due to high requirements in terms of quality and quantity of data, the robustness of models, as well as a careful balance between realism and computational complexity as such. The presented contributions in this field include both physical and physiological models:

- A generalized framework for the minimization of quadratic energies on acquired, arbitrary ultrasound trajectories within the domain of physical modeling. The presented framework allows for an optimization directly in the original sampling space and enables a modeling of the underlying imaging principles and properties in a specific fashion.

- The potential of the framework was demonstrated in terms of an estimation of confidence values for each ultrasound sample based on the probe geometry, the beam properties and the different resolutions in axial and lateral/elevational direction.

- An approach for the extraction and detection of vessels in ultrasound images using a geometrical (physiological) model of vessel appearance in US data. The model was incorporated within a general method to design filters for the detection of desired objects based on the desired second order derivatives using the Hessian matrix.

- As a second contribution to the field of physiological models and their application to vascular ultrasound, a wave-form-like constraint was introduced in order to reconstruct 3D+t blood flow velocities together with the corresponding pulsatile profile in a combined fashion, modeling the changes in laminar flow velocities over the cycles of cardiac pulsation. This results in a combined retrieval of pulse phase information along with estimates of flow direction and maximum flow velocities, allowing for a visualization and quantification of blood flow dynamics in arteries using freehand 3D duplex ultrasound.

With respect to future directions in terms of modeling in ultrasound processing, physical models will gain in all likelihood high importance in the future. While thanks to the availability of high quantities of data for processing, physiological models have already became a standard tool throughout the last decades, physical modeling was mostly considered for direct imaging only. The potential of such models with regard to information processing are, however, enormous, especially with emerging fields, such as robotic and automatic acquisitions of ultrasound data in mind. The integration of physical models, for example by utilizing the confidence of acquired information, will be essential to allow for an acquisition and processing of information in a closed-loop, such that image acquisition and processing parameters could be optimized on-line. In this view, the development of a generalized framework for physical modeling is a promising direction to include detailed acquisition- and process-specific information, such that performance, accuracy and robustness of resulting information can be improved.

List of Figures

Bibliography

[1] Abolmaesumi, P., Sirouspour, M., Salcudean, S.: Real-time extraction of carotid artery contours from ultrasound images. In: Computer-Based Medical Systems, 2000. CBMS 2000. Proceedings. 13th IEEE Symposium on. (2000) 181–186

[2] Aja-Fernández, S., Alberola-López, C.: On the estimation of the coefficient of variation for anisotropic diffusion speckle filtering. Image Processing, IEEE Transactions on **15**(9) (2006) 2694–2701

[3] Alvarez, L., Guichard, F., Lions, P.L., Morel, J.M.: Axioms and fundamental equations of image processing. Archive for Rational Mechanics and Analysis **123**(3) (1993) 199–257

[4] Arigovindan, M., Suhling, M., Jansen, C., Hunziker, P., Unser, M.: Full motion and flow field recovery from echo doppler data. Medical Imaging, IEEE Transactions on **26**(1) (2007) 31–45

[5] Ayache, N., Chapelle, D., Clément, F., Coudière, Y., Delingette, H., Désidéri, J.A., Sermesant, M., Sorine, M., Urquiza, J.M.: Towards model-based estimation of the cardiac electro-mechanical activity from ECG signals and ultrasound images. In: Functional Imaging and Modeling of the Heart. (2001) 120–127

[6] Barry, C., Allott, C., John, N., Mellor, P., Arundel, P., Thomson, D., Waterton, J.: Three-dimensional freehand ultrasound: image reconstruction and volume analysis. Ultrasound in Medicine and Biology **23**(8) (1997) 1209–1224

[7] Bauer, C., Bischof, H.: A novel approach for detection of tubular objects and its application to medical image analysis. In: Pattern Recognition. (2008) 163–172

[8] Baust, M.T.: Polar active contours for medical applications. PhD thesis, München, Technische Universität München, Dissertation (2012)

[9] Bigun, J., Granlund, G.H.: Optimal orientation detection of linear symmetry. In: First International Conference on Computer Vision, ICCV (London). (1987) 433–438

[10] von Birgelen, C., de Vrey, E.A., Mintz, G.S., Nicosia, A., Bruining, N., Li, W., Slager, C.J., Roelandt, J.R., Serruys, P.W., de Feyter, P.J.: ECG-gated three-dimensional intravascular ultrasound feasibility and reproducibility of the automated analysis of coronary lumen and atherosclerotic plaque dimensions in humans. Circulation **96**(9) (1997) 2944–2952

[11] Bjaerum, S., Torp, H., Kristoffersen, K.: Clutter filter design for ultrasound color flow imaging. Ultrasonics, Ferroelectrics and Frequency Control, IEEE Transactions on **49**(2) (2002) 204–216

[12] Bonapace, S., Rossi, A., Cicoira, M., Targher, G., Valbusa, F., Benetos, A., Vassanelli, C.: Increased aortic pulse wave velocity as measured by echocardiography is strongly associated with poor prognosis in patients with heart failure. Journal of the American Society of Echocardiography **26**(7) (2013) 714–720

[13] Bosch, J.G., van Stralen, M., Voormolen, M.M., Krenning, B.J., Lancée, C.T., Reiber, J., van der Steen, A.F., de Jong, N.: Improved spatiotemporal voxel space interpolation for 3D echocardiography with irregular sampling and multibeat fusion. In: Ultrasonics Symposium, 2005 IEEE. Volume 2. (2005) 1232–1235

[14] Bouix, S., Siddiqi, K., Tannenbaum, A.: Flux driven automatic centerline extraction. Medical Image Analysis **9**(3) (2005) 209–221

[15] Boukerroui, D.: A local Rayleigh model with spatial scale selection for ultrasound image segmentation. In Richard Bowden, John Collomosse, K.M., ed.: British Machine Vision Conference, Surrey, United Kingdom (September 2012) 84 12 pages.

[16] Bowes, W., Corke, B., Hulka, J.: Pulse oximetry: a review of the theory, accuracy, and clinical applications. Obstretics and Gynecology **74** (1989) 541–546

[17] Brandestini, M., Forster, F.: Blood flow imaging using a discrete-time frequency meter. In: Ultrasonics Symposium, Proceedings of. (1978) 348–352

[18] Brattain, L.J., Howe, R.D.: Real-time 4D ultrasound mosaicing and visualization. In: Proc.14th intern. conf. Medical Image Computing and Computer-Assisted Intervention. (2011) 105–112

[19] Brooks, A., Connolly, J., Chan, O.: Ultrasound in emergency care. John Wiley & Sons (2008)

[20] Carvalho, D.D., Klein, S., Akkus, Z., Gerrit, L., Schinkel, A.F., Bosch, J.G., van der Lugt, A., Niessen, W.J.: Estimating 3D lumen centerlines of carotid arteries in free-hand acquisition ultrasound. International journal of computer assisted radiology and surgery **7**(2) (2012) 207–215

[21] Chien, A., Sayre, J., Viñuela, F.: Quantitative comparison of the dynamic flow waveform changes in 12 ruptured and 29 unruptured ICA–ophthalmic artery aneurysms. Neuroradiology **55**(3) (2013) 313–320

[22] Clevert, D.a., Johnson, T., Michaely, H., Jung, E.M., Flach, P.M., Strautz, T.I., Reiser, M., Schoenberg, S.O.: High-grade stenoses of the internal carotid artery: comparison of high-resolution contrast enhanced 3D MRA, duplex sonography and power Doppler imaging. European journal of radiology **60**(3) (Dec 2006) 379–86

[23] Cobbold, R.S.C.: Foundations of Biomedical Ultrasound. Biomedical engineering series. Oxford University Press, USA (2006)

[24] Cook, L.B.: Extracting arterial flow waveforms from pulse oximeter waveforms. Anaesthesia **56**(6) (2001) 551–555

[25] Cootes, T.F., Taylor, C.J.: Active shape models smart snakes. In: British Machine Vision Conference 1992. Springer (1992) 266–275

[26] Crosby, J.: Ultrasound-based quantification of myocardial deformation and rotation. PhD thesis, Norwegian University of Science and Technology (2009)

[27] Curie, J., Curie, P.: Développement, par pression, de l'électricité polaire dans les cristaux hémièdres à faces inclinées. Comptes Rendus **91** (1880) 294–295

[28] Delcker, A., Tegeler, C.: Influence of ECG-triggered data acquisition on reliability for carotid plaque volume measurements with a magnetic sensor three-dimensional ultrasound system. Ultrasound in Medicine and Biology **24**(4) (1998) 601–605

[29] Deng, J., Yates, R., Sullivan, I., McDonald, D., Linney, A., Lees, W., Anderson, R., Rodeck, C.: Dynamic three-dimensional color Doppler ultrasound of human fetal intracardiac flow. Ultrasound in Obstetrics and Gynecology **20**(2) (2002) 131–136

[30] Dunmire, B., Beach, K., Labs, K., Plett, M., Strandness Jr, D.: Cross-beam vector doppler ultrasound for angle-independent velocity measurements. Ultrasound in Medicine and Biology **26**(8) (2000) 1213–1235

[31] Dussik, K.T.: Über die Möglichkeit, hochfrequente mechanische Schwingungen als diagnostisches Hilfsmittel zu verwerten. Zeitschrift für die gesamte Neurologie und Psychiatrie **174**(1) (1942) 153–168

[32] Dussik, K.T., Dussik, F., Wyt, L.: Auf dem Wege zur Hyperphonographie des Gehirnes. Wiener M **97** (1947) 425–429

[33] Dutt, V., Greenleaf, J.F.: Statistics of the log-compressed echo envelope. The Journal of the Acoustical Society of America **99**(6) (1996) 3817–3825

[34] Egger, M., Spence, J.D., Fenster, A., Parraga, G.: Validation of 3D ultrasound vessel wall volume: an imaging phenotype of carotid atherosclerosis. Ultrasound in Medicine and Biology **33**(6) (Jun 2007) 905–14

[35] El-Zehiry, N., Yan, M., Good, S., Fang, T., Zhou, S.K., Grady, L.: Learning the manifold of quality ultrasound acquisiton. In: Medical Image Computing and Computer-Assisted Intervention–MICCAI 2013. (2013) 122–130

[36] Eyer, M., Brandestini, M., Phillips, D., Baker, D.: Color digital echo/doppler image presentation. Ultrasound in Medicine and Biology **7**(1) (1981) 21–31

[37] Fenster, A., Chiu, B., Landry, A., Spence, J.D., Parraga, G.E.: 3D ultrasound system for analysis of carotid plaque progression and regression. In: 40th Asilomar Conference on Signals, Systems and Computers ACSSC '06, Proceedings of. (2006) 1966–1970

[38] Fenster, a., Downey, D.B., Cardinal, H.N.: Three-dimensional ultrasound imaging. Physics in Medicine and Biology **46**(5) (May 2001) R67–99

[39] Filis, K.a., Arko, F.R., Johnson, B.L., Pipinos, I.I., Harris, E.J., Olcott, C., Zarins, C.K.: Duplex ultrasound criteria for defining the severity of carotid stenosis. Annals of vascular surgery **16**(4) (Jul 2002) 413–21

[40] Forsberg, F.: Ultrasonic biomedical technology; marketing versus clinical reality. Ultrasonics **42** (2004) 17 – 27

[41] Fox, M.D.: Multiple crossed-beam ultrasound doppler velocimetry. Sonics and Ultrasonics, IEEE Transactions on **25**(5) (1978) 281–286

[42] Frangi, A.F., Niessen, W.J., Vincken, K.L., Viergever, M.A.: Multiscale vessel enhancement filtering. In: Medical Image Computing and Computer-Assisted Interventation—MICCAI'98. (1998) 130–137

[43] Freiman, M., Joskowicz, L., Sosna, J.: A variational method for vessels segmentation: algorithm and application to liver vessels visualization. In: SPIE Medical Imaging, International Society for Optics and Photonics (2009) 72610H–72610H

[44] Gómez, A., de Vecchi, A., Pushparajah, K., Simpson, J., Giese, D., Schaeffter, T., Penney, G.: 3D intraventricular flow mapping from colour Doppler images and wall motion. In: Medical Image Computing and Computer-Assisted Intervention–MICCAI 2013. (2013) 476–483

[45] Gülsün, M.A., Tek, H.: Robust vessel tree modeling. In: Medical Image Computing and Computer-Assisted Intervention–MICCAI 2008. (2008) 602–611

[46] Gamble, G., Zorn, J., Sanders, G., MacMahon, S., Sharpe, N.: Estimation of arterial stiffness, compliance, and distensibility from M-mode ultrasound measurements of the common carotid artery. Stroke **25**(1) (1994) 11–16

[47] Garcia, D., del Álamo, J.C., Tanné, D., Yotti, R., Cortina, C., Bertrand, É., Antoranz, J.C., Pérez-David, E., Rieu, R., Fernández-Avilés, F., et al.: Two-dimensional intraventricular flow mapping by digital processing conventional color-doppler echocardiography images. Medical Imaging, IEEE Transactions on **29**(10) (2010) 1701–1713

[48] Gemignani, V., Bianchini, E., Faita, F., Giannarelli, C., Plantinga, Y., Ghiadoni, L., Demi, M.: Ultrasound measurement of the brachial artery flow-mediated dilation without ECG gating. Ultrasound in Medicine and Biology **34**(3) (2008) 385–391

[49] Giannarelli, C., Bianchini, E., Bruno, R.M., Magagna, A., Landini, L., Faita, F., Gemignani, V., Penno, G., Taddei, S., Ghiadoni, L.: Local carotid stiffness and intima-media thickness assessment by a novel ultrasound-based system in essential hypertension. Atherosclerosis **223**(2) (2012) 372–377

[50] Gill, J.D., Ladak, H.M., Steinman, D.A., Fenster, A.: Segmentation of ulcerated plaque: a semi-automatic method for tracking the progression of carotid atherosclerosis. In: Proc. 22nd Annual Int Engineering in Medicine and Biology Society Conf. of the IEEE. Volume 1. (2000) 669–672

[51] Gill, S., Abolmaesumi, P., Fichtinger, G., Boisvert, J., Pichora, D., Borshneck, D., Mousavi, P.: Biomechanically constrained groupwise ultrasound to CT registration of the lumbar spine. Medical Image Analysis **16**(3) (2012) 662 – 674

[52] Gomez, A., Pushparajah, K., Simpson, J.M., Giese, D., Schaeffter, T., Penney, G.: A sensitivity analysis on 3D velocity reconstruction from multiple registered echo Doppler views. Medical Image Analysis **17**(6) (2013) 616–631

[53] Gonçalves, L.F., Espinoza, J., Kusanovic, J.P., Lee, W., Nien, J.K., Santolaya-Forgas, J., Mari, G., Treadwell, M.C., Romero, R.: Applications of 2-dimensional matrix array for 3-and 4-dimensional examination of the fetus - a pictorial essay. Journal o Ultrasound in Medicine **25**(6) (2006) 745–755

[54] Grady, L.: Random walks for image segmentation. Pattern Analysis and Machine Intelligence, IEEE Transactions on **28**(11) (Nov 2006) 1768–1783

[55] Grant, E.G., Benson, C.B., Moneta, G.L., Alexandrov, A.V., Baker, J.D., Bluth, E.I., Carroll, B.a., Eliasziw, M., Gocke, J., Hertzberg, B.S., et al.: Carotid artery stenosis: gray-scale and Doppler US diagnosis–Society of Radiologists in Ultrasound Consensus Conference. Radiology **229**(2) (Nov 2003) 340–6

[56] Grant, E.G., Duerinckx, A.J., El Saden, S.M., Melany, M.L., Hathout, G.M., Zimmerman, P.T., Marumoto, A.K., Cohen, S.N., Baker, J.D.: Ability to use duplex US to quantify internal carotid arterial stenoses: fact or fiction? Radiology **214** (2000) 247–252

[57] Grewenig, S., Weickert, J., Schroers, C., Bruhn, A.: Cyclic schemes for PDE-based image analysis. Technical report, Technical Report 327, Department of Mathematics, Saarland University, Saarbrücken, Germany (2013)

[58] de Groot, E., Hovingh, G.K., Wiegman, A., Duriez, P., Smit, A.J., Fruchart, J.C., Kastelein, J.J.: Measurement of arterial wall thickness as a surrogate marker for atherosclerosis. Circulation **109**(23 suppl 1) (2004) III–33

[59] Guerrero, J., Salcudean, S.E., McEwen, J.A., Masri, B.A., Nicolaou, S.: Real-time vessel segmentation and tracking for ultrasound imaging applications. Medical Imaging, IEEE Transactions on **26**(8) (2007) 1079–1090

[60] Harloff, A., Zech, T., Wegent, F., Strecker, C., Weiller, C., Markl, M.: Comparison of blood flow velocity quantification by 4D flow MR imaging with ultrasound at the carotid bifurcation. American Journal of Neuroradiology **34**(7) (2013) 1407–1413

[61] Hastenteufel, M.: Neue Methoden des 3D Ultraschalls zur Geschwindigkeitsrekonstruktion und intraoperativen Navigation. PhD thesis, Universität Fridericiana, Karlsruhe, Germany (2005)

[62] Hellier, P., Coupé, P., Morandi, X., Collins, D.L.: An automatic geometrical and statistical method to detect acoustic shadows in intraoperative ultrasound brain images. Medical Image Analysis **14**(2) (2010) 195 – 204

[63] Hennersperger, C., Baust, M., Waelkens, P., Karamalis, A., Ahmadi, S.A., Navab, N.: Multi-scale tubular structure detection in ultrasound imaging. Medical Imaging, IEEE Transactions on **34**(1) (Jan 2015) 13–26

[64] Hennersperger, C., Karamalis, A., Navab, N.: Vascular 3D+T freehand ultrasound using correlation of doppler and pulse-oximetry data. In Stoyanov, D., Collins, D.L., Sakuma, I., Abolmaesumi, P., Jannin, P., eds.: Information Processing in Computer Assisted Interventions - IPCAI 2014, Lecture Notes in Computer Science. Volume 8498. (2014) in press.

[65] Hennersperger, C., Mateus, D., Baust, M., Navab, N.: A quadratic energy minimization framework for signal loss estimation from arbitrarily sampled ultrasound data. In: Medical Image Computing and Computer-Assisted Intervention–MICCAI 2014. (2014) 373–380

[66] Hoskins, P.R.: Simulation and validation of arterial ultrasound imaging and blood flow. Ultrasound in Medicine and Biology **34**(5) (2008) 693 – 717

[67] Housden, R.J., Gee, A.H., Treece, G.M., Prager, R.W.: Sensorless reconstruction of unconstrained freehand 3D ultrasound data. Ultrasound in Medicine and Biology **33**(3) (2007) 408–419

[68] Hung, J., Lang, R., Flachskampf, F., Shernan, S.K., McCulloch, M.L., Adams, D.B., Thomas, J., Vannan, M., Ryan, T.: 3D echocardiography: a

review of the current status and future directions. Journal of the American Society of Echocardiography : official publication of the American Society of Echocardiography **20**(3) (Mar 2007) 213–33

[69] Huo, Y., Kassab, G.S.: A hybrid one-dimensional Womersley model of pulsatile blood flow in the entire coronary arterial tree. American Journal of Physiology-Heart and Circulatory Physiology **292**(6) (2007) H2623–H2633

[70] Jacso, F., Kouznetsov, A., Smith, W.L.: Development and evaluation of an ultrasound-guided tracking and gating system for hepatic radiotherapy. Medical physics **36**(12) (2009) 5633–5640

[71] Jaff, M., White, C.: Vascular disease: diagnostic and therapeutic approaches. Cardiotext Publishing (2011)

[72] Kalmus, H., Hedrich, A., Pardue, D.: The acoustic flowmeter using electroric switching. Ultrasonic Engineering, Transactions of the IRE Professional Group on (1954) 49–63

[73] Kannappan, P., Sahoo, P.: Rotation invariant separable functions are gaussian. SIAM Journal on Mathematical Analysis **23**(5) (1992) 1342–1351

[74] Karadayi, K., Hayashi, T., Kim, Y.: Automatic image-based gating for 4D ultrasound. In: Engineering in Medicine and Biology Society, 2006. EMBS '06. 28th Annual International Conference of the IEEE. (2006) 2388 –2391

[75] Karamalis, A., Wein, W., Klein, T., Navab, N.: Ultrasound confidence maps using random walks. Medical Image Analysis **16**(6) (2012) 1101 – 1112

[76] Kass, M., Witkin, A., Terzopoulos, D.: Snakes: active contour models. International Journal of Computer Vision **1**(4) (1988) 321–331

[77] Klein, T., Hansson, M., Navab, N.: Modeling of multi-view 3D freehand radio frequency ultrasound. In: Proc.15th intern. conf. Medical Image Computing and Computer-Assisted Intervention. (2012) 422–429

[78] Knutsson, H., Westin, C.F.: Normalized and differential convolution. In: Computer Vision and Pattern Recognition, 1993. Proceedings CVPR '93., 1993 IEEE Computer Society Conference on. (1993) 515 –523

[79] de Korte, C.L., Hansen, H.H., van der Steen, A.F.: Vascular ultrasound for atherosclerosis imaging. Interface Focus (2011) rsfs20110024

[80] Krissian, K., Ellsmere, J., Vosburgh, K., Kikinis, R., Westin, C.F.: Multiscale segmentation of the aorta in 3D ultrasound images. In: Engineering in Medicine and Biology Society, 2003. Proceedings of the 25th Annual International Conference of the IEEE. Volume 1. (2003) 638–641

[81] Krissian, K., Malandain, G., Ayache, N., Vaillant, R., Trousset, Y.: Model-based detection of tubular structures in 3D images. Computer vision and image understanding **80**(2) (2000) 130–171

[82] Kuppler, C.S., Christie, J.W., Newton III, W.B., Ghanami, R.J., Craven, T.E., Berry, J.L., Hansen, K.J.: Stent effects on duplex velocity estimates. Journal of Surgical Research **183**(1) (2013) 457–461

[83] Leung, K., van Stralen, M., van Burken, G., de Jong, N., Bosch, J.: Automatic active appearance model segmentation of 3D echocardiograms. In: Biomedical Imaging: From Nano to Macro, 2010 IEEE International Symposium on. (April 2010) 320–323

[84] Li, B., Acton, S.T.: Active contour external force using vector field convolution for Image segmentation. Image Processing, IEEE Transactions on **16** (2007) 2096–2106

[85] Lindeberg, T.: Scale-space theory: a basic tool for analyzing structures at different scales. Journal of Applied Statistics **21**(1-2) (1994) 225–270

[86] Liu, S., Padfield, D., Mendonca, P.: Tracking of carotid arteries in ultrasound images. In: Medical Image Computing and Computer-Assisted Intervention–MICCAI 2013. (2013) 526–533

[87] Loizou, C.P., Pattichis, C.S., Pantziaris, M., Nicolaides, A.: An integrated system for the segmentation of atherosclerotic carotid plaque. Information Technology in Biomedicine, IEEE Transactions on **11** (2007) 661–667

[88] Mackenzie, I., Wilkinson, I., Cockcroft, J.: Assessment of arterial stiffness in clinical practice. Qjm **95**(2) (2002) 67–74

[89] Makris, G.C., Lavida, A., Griffin, M., Geroulakos, G., Nicolaides, A.N.: Three-dimensional ultrasound imaging for the evaluation of carotid atherosclerosis. Atherosclerosis **219**(2) (Dec 2011) 377–83

[90] Mason, W.P.: Sonics and ultrasonics: Early history and applications. Sonics and Ultrasonics, IEEE Transactions on **23**(4) (1976) 224–231

[91] Matangi, M., Armstrong, D., Jurt, U., Johri, A., Brouillard, D.: The sensitivity, specificity and accuracy of a screening carotid examination compared to a formal carotid study. Canadian Journal of Cardiology **29**(10) (2013) S310–S310

[92] Matter, C.M., Stuber, M., Nahrendorf, M.: Imaging of the unstable plaque: how far have we got? European Heart Journal **30**(21) (2009) 2566–2574

[93] Miller, J.V., Breen, D.E., Lorensen, W.E., O'Bara, R.M., Wozny, M.J.: Geometrically deformed models: a method for extracting closed geometric models form volume data. In: 18th Annual Conference on Computer Graphics and Interactive Techniques, Proceedings of. (1991) 217–226

[94] Misaridis, T., Jensen, J.: Use of modulated excitation signals in medical ultrasound. Part I: basic concepts and expected benefits. Ultrasonics, Ferroelectrics and Frequency Control, IEEE Transactions on **52**(2) (Feb 2005) 177–191

[95] Morozov, O., Unser, M., Hunziker, P.: Reconstruction of large, irregularly sampled multidimensional images. A tensor-based approach. Medical Imaging, IEEE Transactions on **30**(2) (2011) 366–374

[96] Motsch, L., Gaull, M.: Three-dimensional power-mode ultrasound for quantification of the progression of carotid artery atherosclerosis. Journal of Neurology **247** (2000) 106–111

[97] Muñoz, D.R., Markl, M., Mur, J.L.M., Barker, A., Fernández-Golfín, C., Lancellotti, P., Gómez, J.L.Z.: Intracardiac flow visualization: current status and future directions. European Heart Journal–Cardiovascular Imaging **14**(11) (2013) 1029–1038

[98] Nanda, N.C.: History of echocardiographic contrast agents. Clinical Cardiology **20**(S1) (1997) 7–11

[99] Ng, A., Swanevelder, J.: Resolution in ultrasound imaging. Continuing Education in Anaesthesia, Critical Care & Pain **11** (2011) 186–192

[100] Noble, J.: Ultrasound image segmentation and tissue characterization. Proceedings of the Institution of Mechanical Engineers, Part H: Journal of Engineering in Medicine **224**(2) (2010) 307–316

[101] Noble, J., Boukerroui, D.: Ultrasound image segmentation: a survey. Medical Imaging, IEEE Transactions on **25**(8) (Aug 2006) 987–1010

[102] van den Oord, S.C., ten Kate, G.L., Sijbrands, E.J., van der Steen, A.F., Schinkel, A.F.: Effect of carotid plaque screening using contrast-enhanced ultrasound on cardiovascular risk stratification. The American Journal of Cardiology **111**(5) (2013) 754–759

[103] Oshima, M., Torii, R., Kobayashi, T., Taniguchi, N., Takagi, K.: Finite element simulation of blood flow in the cerebral artery. Computer Methods in Applied Mechanics and Engineering **191**(6–7) (2001) 661 – 671

[104] Pain, H.J.: The physics of vibrations and waves. John Wiley and sons (2005)

[105] Pellerito, J., Polak, J.F.: Introduction to vascular ultrasonography. Elsevier Health Sciences (2012)

[106] Pereira, V.M., Ouared, R., Brina, O., Bonnefous, O., Satwiaski, J., Aerts, H., Ruijters, D., van Nijnatten, F., Perren, F., Bijlenga, P., et al.: Quantification of internal carotid artery flow with digital sustration angiography: validation of an optical flow approach with doppler ultrasound. American Journal of Neuroradiology **35**(1) (2014) 156–163

[107] Pock, T., Beichel, R., Bischof, H.: A novel robust tube detection filter for 3d centerline extraction. In: Image Analysis. (2005) 481–490

[108] Pock, T., Janko, C., Beichel, R., Bischof, H.: Multiscale medialness for robust segmentation of 3D tubular structures. In: 10th Computer vision winter workshop. (2005) 93–102

[109] Postema, M.: Fundamentals of medical ultrasonics. CRC Press (2011)

[110] Prager, R., Gee, A., Treece, G., Berman, L.: Freehand 3D ultrasound without voxels: volume measurement and visualisation using the Stradx system. Ultrasonics **40**(1–8) (2002) 109 – 115

[111] Prager, R., Ijaz, U., Gee, A., Treece, G.: Three-dimensional ultrasound imaging. Proc. Institution of Mechanical Engineers, Part H: Journal of Engineering in Medicine **224** (2010) 193–223

[112] Rayleigh, J.W.S.: The theory of sound. McMillan Co., London (1877)

[113] Reinertsen, I., Descoteaux, M., Siddiqi, K., Collins, D.L.: Validation of vessel-based registration for correction of brain shift. Medical Image Analysis **11** (2007) 374–388

[114] Renault, G., Tranquart, F., Perlbarg, V., Bleuzen, A., Herment, A., Frouin, F.: A posteriori respiratory gating in contrast ultrasound for assessment of hepatic perfusion. Physics in Medicine and Biology **50**(19) (2005) 4465

[115] Rim, J.H., Lee, H.Y., Yoo, S.M., Jung, H.Y., White, C.S.: Carotid doppler ultrasonography as a surrogate for coronary CT angiography to exclude subclinical coronary atherosclerosis in asymptomatic patients with a negative coronary calcium score. Journal of Clinical Ultrasound **41**(3) (2013) 164–170

[116] Rohling, R., Gee, A., Berman, L.: A comparison of freehand three-dimensional ultrasound reconstruction techniques. Medical Image Analysis **3** (1999) 339–359

[117] Round, W., Bates, R.: Modification of spectra of pulses from ultrasonic transducers by scatterers in non-attenuating and in attenuating media. Ultrasonic imaging **9**(1) (1987) 18–28

[118] Rubin, J.M., Brian Fowlkes, J., Prince, M.R., Rhee, R.T., Chenevert, T.L.: Doppler US gating of cardiac MR imaging. Academic Radiology **7**(12) (2000) 1116–1122

[119] Sakalihasan, N., Limet, R., Defawe, O.: Abdominal aortic aneurysm. The Lancet **365**(9470) (2005) 1577–1589

[120] Schulte zu Berge, C., Baust, M., Kapoor, A., Navab, N.: Predicate-based focus-and-context visualization for 3D Ultrasound. Visualization and Computer Graphics, IEEE Transactions on **20**(12) (Dec 2014) 2379–2387

[121] Shankar, P.M.: Ultrasonic tissue characterization using a generalized Nakagami model. Ultrasonics, Ferroelectrics and Frequency Control, IEEE Transactions on **48**(6) (2001) 1716–1720

[122] Singaraju, D., Grady, L., Vidal, R.: Interactive image segmentation via minimization of quadratic energies on directed graphs. In: Computer Vision and Pattern Recognition, 2008. CVPR 2008. IEEE Conference on. (June 2008) 1–8

[123] Slabaugh, G., Unal, G., Wels, M., Fang, T., Rao, B.: Statistical region-based segmentation of ultrasound images. Ultrasound in Medicine and Biology **35**(5) (2009) 781 – 795

[124] Soergel, U.: Radar remote sensing of urban areas. Volume 15. Springer (2010)

[125] Solberg, O.V., Lindseth, F., Torp, H., Blake, R.E., Nagelhus Hernes, T.A.: Freehand 3D ultrasound reconstruction algorithms - a review. Ultrasound in Medicine and Biology **33** (2007) 991–1009

[126] Stoitsis, J., Golemati, S., Kendros, S., Nikita, K.: Automated detection of the carotid artery wall in B-mode ultrasound images using active contours initialized by the Hough transform. In: Engineering in Medicine and Biology Society, 2008. EMBS 2008. 30th Annual International Conference of the IEEE, IEEE (2008) 3146–3149

[127] Sundar, H., Khamene, A., Yatziv, L., Xu, C.: Automatic image-based cardiac and respiratory cycle synchronization and gating of image sequences. In: Proc.12th intern. conf. Medical Image Computing and Computer-Assisted Intervention. (2009) 381–388

[128] Swillens, A., De Santis, G., Segers, P., Lovstakken, L., Degroote, J., Vierendeels, J.: Multiphysics modeling in support of ultrasonic image development: Integration of fluid-structure interaction simulations and Field II applied to the carotid artery. In: Ultrasonics Symposium (IUS), 2011 IEEE International. (Oct 2011) 1587–1590

[129] Swillens, A., Lovstakken, L., Kips, J., Torp, H., Segers, P.: Ultrasound simulation of complex flow velocity fields based on computational fluid dynamics. Ultrasonics, Ferroelectrics and Frequency Control, IEEE Transactions on **56**(3) (March 2009) 546–556

[130] Swillens, A., Segers, P., Degroote, J., Vierendeels, J., Lovstakken, L.: Improving ultrasonic imaging of the vascular wall and blood flow using a multiphysics simulation tool integrating fluid-structure interaction and ultrasound simulations. In: Ultrasonics Symposium (IUS), 2010 IEEE. (Oct 2010) 1657–1660

[131] Treece, G., Prager, R., Gee, A.: Ultrasound attenuation measurement in the presence of scatterer variation for reduction of shadowing and enhancement. Ultrasonics, Ferroelectrics and Frequency Control, IEEE Transactions on **52**(12) (Dec 2005) 2346–2360

[132] Treece, G.M., Gee, A.H., Prager, R.W., Cash, C.J., Berman, L.H.: High-definition freehand 3-D ultrasound. Ultrasound in Medicine and Biology **29**(4) (Apr 2003) 529–546

[133] Treece, G.M., Prager, R.W., Gee, A.H., Cash, C.J., Berman, L.: Grey-scale gating for freehand 3D ultrasound. In: Biomedical Imaging, 2002. Proceedings. 2002 IEEE International Symposium on, IEEE (2002) 993–996

[134] Tsutsui, H., Schoenhagen, P., Crowe, T.D., Klingensmith, J.D., Vince, D.G., Nissen, S.E., Tuzcu, E.M.: Influence of coronary pulsation on volumetric intravascular ultrasound measurements performed without ECG-gating. Validation in vessel segments with minimal disease. The international Journal of Cardiovascular Imaging **19**(1) (2003) 51–57

[135] Ukwatta, E., Buchanan, D., Parraga, G., Fenster, A.: Three-dimensional ultrasound imaging of carotid atherosclerosis. In: Intelligent Computation and Bio-Medical Instrumentation (ICBMI). (2011) 81–84

[136] Ukwatta, E., Buchanan, D., Parraga, G., Fenster, A.: Three-dimensional uUltrasound imaging of carotid atherosclerosis. Intelligent Computation and Bio-Medical Instrumentation, 2011 International Conference on (Dec 2011) 81–84

[137] Wachinger, C., Klein, T., Navab, N.: Locally adaptive nakagami-based ultrasound similarity measures. Ultrasonics **52**(4) (2012) 547–554

[138] Wachinger, C., Shams, R., Navab, N.: Estimation of acoustic impedance from multiple ultrasound images with application to spatial compounding. In: Computer Vision and Pattern Recognition Workshops, 2008. CVPRW'08. IEEE Computer Society Conference on. (2008) 1–8

[139] Wachinger, C., Yigitsoy, M., Navab, N.: Manifold learning for image-based breathing gating with application to 4D ultrasound. In: Proc.13th intern. conf. Medical Image Computing and Computer-Assisted Intervention. (2010) 26–33

[140] Wachinger, C., Yigitsoy, M., Rijkhorst, E.J., Navab, N.: Manifold learning for image-based breathing gating in ultrasound and MRI. Medical image analysis **16**(4) (2012) 806–818

[141] Waechter, I., Bredno, J., Hermans, R., Weese, J., Barratt, D.C., Hawkes, D.J.: Model-based blood flow quantification from rotational angiography. Medical Image Analysis **12**(5) (2008) 586–602

[142] Waelkens, P., Ahmadi, S.A., Navab, N.: Frangi goes US: multiscale tubular structure detection adapted to 3D ultrasound. In: Medical Image Computing and Computer-Assisted Intervention–MICCAI 2012. (2012) 625–633

[143] Wang, D., Klatzky, R., Amesur, N., Stetten, G.: Carotid artery and jugular vein tracking and differentiation using spatiotemporal analysis. In: Medical Image Computing and Computer-Assisted Intervention–MICCAI 2006. (2006) 654–661

[144] Wang, D.C., Klatzky, R., Wu, B., Weller, G., Sampson, A.R., Stetten, G.D.: Fully automated common carotid artery and internal jugular vein identification and tracking using B-mode ultrasound. Biomedical Engineering, IEEE Transactions on **56**(6) (2009) 1691–1699

[145] Weickert, J., Romeny, B., Viergever, M.: Efficient and reliable schemes for nonlinear diffusion filtering. Image Processing, IEEE Transactions on **7**(3) (Mar 1998) 398–410

[146] Wein, W., Brunke, S., Khamene, A., Callstrom, M.R., Navab, N.: Automatic CT-ultrasound registration for diagnostic imaging and image-guided intervention. Medical image analysis **12**(5) (2008) 577–585

[147] Wein, W., Pache, F., Röper, B., Navab, N.: Backward-warping ultrasound reconstruction for improving diagnostic value and registration. In Larsen, R., Nielsen, M., Sporring, J., eds.: Medical Image Computing and Computer-Assisted Intervention – MICCAI 2006. Volume 4191 of Lecture Notes in Computer Science. (2006) 750–757

[148] Wild, J.J., Reid, J.M.: Application of echo-ranging techniques to the determination of structure of biological tissues. Science (1952) 226–30

[149] WOLFE, S.B., Popp, R.L., FEIGENBAUM, H.: Diagnosis of atrial tumors by ultrasound. Circulation **39**(5) (1969) 615–622

[150] Xiao, G., Brady, M., Noble, J., Zhang, Y.: Segmentation of ultrasound b-mode images with intensity inhomogeneity correction. Medical Imaging, IEEE Transactions on **21**(1) (Jan 2002) 48–57

[151] Xu, C., Prince, J.L.: Gradient vector flow: A new external force for snakes. In: Computer Vision and Pattern Recognition, 1997. Proceedings., 1997 IEEE Computer Society Conference on, IEEE (1997) 66–71

[152] Xu, Q., Hamilton, R.J.: A novel respiratory detection method based on automated analysis of ultrasound diaphragm video. Medical physics **33**(4) (2006) 916–921

[153] Yu, Y., Acton, S.: Speckle reducing anisotropic diffusion. Image Processing, IEEE Transactions on **11**(11) (Nov 2002) 1260–1270

[154] Yu, Y., Wang, J.: Backscatter-contour-attenuation joint estimation model for attenuation compensation in ultrasound imagery. Image Processing, IEEE Transactions on **19**(10) (Oct 2010) 2725–2736

[155] Zettinig, O., Hennersperger, C., zu Berge, C.S., Baust, M., Navab, N.: 3D velocity field and flow profile reconstruction from arbitrarily sampled doppler ultrasound data. In: Medical Image Computing and Computer-Assisted Intervention–MICCAI 2014. Springer (2014) 611–618

[156] Zhao, S., Xu, X., Hughes, A., Thom, S., Stanton, A., Ariff, B., Long, Q.: Blood flow and vessel mechanics in a physiologically realistic model of a human carotid arterial bifurcation. Journal of Biomechanics **33**(8) (2000) 975 – 984

[157] Zitová, B., Flusser, J.: Image registration methods: a survey. Image and Vision Computing **21**(11) (2003) 977 – 1000

A

Vascular 3D+T Freehand Ultrasound using Correlation of Doppler and Pulse-Oximetry Data

Christoph Hennersperger[1], Athanasios Karamalis[1], and Nassir Navab[1]

[1] Chair for Computer Aided Medical Procedures (CAMP), Technische Universität München, Germany.

Contribution. The author's contribution to this publication comprise the main idea, the complete implementation, all tests as well as the construction of the experimental setup and its validation. After initial drafting by the thesis' author, the paper was revised jointly with the indicated co-authors.

Abstract. We present a new system to acquire and reconstruct 3D freehand ultrasound volumes from arbitrary 2D image acquisitions over time. Motion artifacts are significantly reduced with a novel gating approach which correlates pulse oximetry data with Doppler ultrasound. The reconstruction problem is split into a ray-based sample selection on a per-scanline basis and a backward algorithm which is based on the concept of normalized convolution. We introduce an adaptive derivation of time-domain interpolation from the correlated pulse-oximetry and Doppler signals as well as an ellipsoid kernel size for spatial interpolation based on the physical resolution of the ultrasound data. We compare pulse-oximetry to classical ECG gating and further show the suitability of our normalized pulse signal for 3D+T reconstructions. The ease of use of the setup without the need of uncomfortable triggering via ECG provides the ability to use 3D+T ultrasound in every day clinical practice.

A.1 Introduction

Ultrasound imaging is an essential part of clinical imaging and plays a crucial role in diagnosis of cardiovascular diseases. Three dimensional (3D) ultrasound imaging is already used in obstetrics for diagnosis of facial abnormalities and has high potential for vascular imaging [4]. While 2D matrix array probes are providing 3D and 4D (3D+T) ultrasound information in realtime [10], they are - as conventional 1D array probes - limited in their field of view with respect to transducer design. Freehand ultrasound as an alternative or add-on technique allows the acquisition of high quality 3D ultrasound of steady anatomy; providing an extended field-of-view [11] and thus enables a better overview for physicians. For vascular applications though, the data is acquired over a certain period of time, in which the anatomy changes due to pulsating blood flow.

One major area where avoiding these artifacts is of crucial importance is 3D and 4D volume reconstruction (compounding). The goal here is to interpolate the acquired, irregulary sampled data onto a regular spatial 3D grid to enable an extraction of diagnostic indices (e.g. vessel volume from a segmentation) and visualization of the data in 3D. We propose the use of a fingertip pulse oximetry device, in addition to a 3D freehand ultrasound setup, recording B-Mode and Doppler ultrasound data, to reconstruct 3D volumes for desired cardiac pulse phases. This offers the possibility to accurately reconstruct pulse phase information while avoiding the cumbersome placement of electrodes for ECG gating, which is not applicable in many every-day screening applications with short investigation periods. Pulse oximeters are used as a standard tool in hospitals and allow the monitoring of the patient's oxygen saturation and heart frequency by analyzing the light absorption due to oxygenated red blood cells through thin tissue (i.e. finger or earlobe). However, as the sensors are measuring the local pulsation, which is not synchronous to cardiac excitation due to different patient anatomy, the signals cannot be used for interpolation without a reference to the ultrasound data.

To provide high-quality reconstructions and make full use of the discussed system setup we propose a novel approach to correlate pulse oximetry with

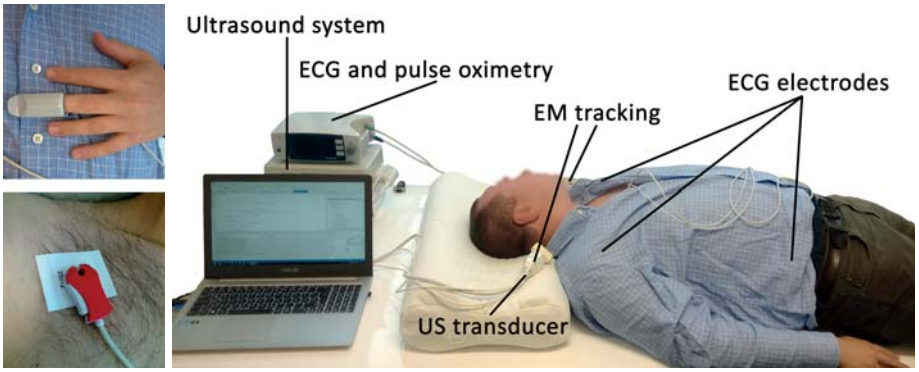

Figure A.1: The experimental setup consists of a combined pulse oximetry / ECG device, an open-access ultrasound system and two electomagnetic trackers mounted on the ultrasound probe. For ECG gating, three electrodes (left bottom) have to be mounted on three torso positions to retrieve a ECG curve, while for pulse-oximetry (left top), only a fingertip is required.

Doppler ultrasound information. This allows an automatic and accurate calibration of the pulse oximetry sensor individually for every acquisition. Thus, the pulse oximetry data can be used as a reference for constructing normalized pulse phase signals. The reconstruction of 3D+T volume data from single ultrasound scanlines is computed using a concept similar to normalized convolution [8] for $0 - th$ order interpolation. We propose the selection of samples for the reconstruction of every voxel based on an ellipsoid region defined by the US properties around every sample in a backward transformation step. Therefore, we are able to split the sample-selection from the voxel interpolation to reconstruct smooth volumes with respect to the local spatial resolution of the original ultrasound sample data. We compare pulse-oximetry to ECG gating and further demonstrate the advantages of using adaptive time-domain interpolation for the application of carotid artery freehand ultrasound.

A.2 Related Work

Although ECG can be used to accurately detect cardiac phases for freehand ultrasound [2], the equipment needed is relatively cumbersome and consequently several alternative methods were developed relying on the ultrasound data only. First approaches based on filtering of intermediate signals containing cardiac information calculated from intensity values [13] or via the centroid algorithm [6] demonstrated good performances but needed either user input or were limited to certain areas. Further approaches based on phase correlation [12] and manifold learning with Laplacian eigenmaps [14] were successfully applied to US data for detection of both cardiac and respiratory motion. However, most of the proposed image-based methods rely on a constant pulse frequency for detection [13, 6, 12] and provide rough estimates of cardiac pulse phases [13, 6, 12, 14] which could introduce artifacts in 4D reconstruction with

time-domain interpolation.

3D volume reconstruction methods can be grouped into pixel-based methods, voxel-based methods and function-based methods [11]. Pixel-based methods transform pixel values with a forward transformation into corresponding voxels. Voxel-based methods traverse every voxel and map back corresponding pixel values. Function-based methods estimate an interpolation function from the input data and evaluate the function at a regular grid. Recent advances in reconstruction methods also led to improvements by modeling US statistics in a physical way by using Nakagami distributions [7]. Although these methods provide volumetric data of exceptional quality, the computational demands prevent their application in time-critical applications. In [1] a similar reconstruction approach is used to carry out interpolation in the spatio-temporal (4D) domain. However they apply interpolation only in forward direction and do not consider adaptive interpolation in both spatial and temporal domain.

A.3 Methods

Our goal is to obtain an instensity value $I(v_i, \phi)$ for every voxel $v_i \in V$ in the Cartesian equidistant volume $V \in \mathbb{R}^3$ for a given timepoint ϕ in the cardiac pulse phase. We separate the ultrasound sample selection in spatial and temporal domain from the actual voxel reconstruction, as a sample selection in voxel coordinates (i.e. searching for the k nearest neighbours in the 4D volume) would ignore the physical and temporal information of our acquisition. Instead, we supply temporal and spatial weights for every sample-voxel relation to the reconstruction step. These weights are defined based on either the (temporal) pulse phase information, or the (spatial) ultrasound beam information. Therefore, the reconstruction approach is split into three parts: i) the retrieval of a normalized pulse phase signal for every acquisition; ii) a physics-based selection of ultrasound samples contributing to each voxel; and iii) the reconstruction of the final voxel intensity value from the selected samples.

A.3.1 Retrieval of Normalized Pulse Signal

We aim to reconstruct 4D data for different points within the cardiac pulse phase and thus introduce a fingertip pulse oximetry device as a reference sensor in the setup, which provides a measure of the oxygen saturation throughout the cardiac pulse phase. As pulse oximetry values are influenced by the percentage of blood that is loaded with oxygen [3], the measured signal changes during cardiac pulse phases and is related to changes in vessel diameter caused by volume-deviations. This is exactly what we are aiming for as changes in vessel diameter are the cause of ”pulsatile” artifacts in ultrasound acquisitions. Consequently, the pulse-oximetry signal can not only be used for gating, as it is currently also done with ECG, but also to reconstruct a normalized pulse shape signal. This shape signal can then be used directly within the reconstruction.

In order to be able to utilize the pulse oximetry signal, we first have to carry out a calibration to the ultrasound data, as due to different anatomy and pulse-

wave-velocities, the temporal offset between fingertip and target ultrasound location will vary among different acquisitions. For vascular applications, a second signal containing pulse phase information can be retrieved from the Doppler ultrasound components belonging to non-stationary, moving scatterers within the volume of interest. These components can be identified as the sum of all non-zero Doppler data components after clutter filtering of the ultrasound ensemble, where stationary and slowly moving components are removed from the signal. By having two signals containing pulse information, we can automatically map US data to cardiac pulse phases for individual acquisitions without any preconditions of a constant pulse frequency or the absence of arrhythmia. To enable a direct correlation, we extract an arterial flow velocity signal - corresponding to Doppler signals - from the pulse oximetry data by taking the gradient of the signal [3] (see Fig. A.2a). Consequently, the time offset $o_{d\to p}$ between the corresponding data can be retrieved by finding the maximum cross-correlation of both real signals as:

$$o_{d\to p} = \arg\max_{l} \sum_{k=0}^{K-l-1} d_{k+l} * p'_k \quad w.r.t. \quad p'_k = \frac{\partial p_k}{\partial k}, \tag{A.1}$$

with p'_k and d_{k+l} representing the pulse derivative and shifted Doppler data with offset l respectively. Based on the calibration, we can use the pulse-oximetry signal to reconstruct a normalized pulse shape signal $\bar{p}$. Therefore, we first automatically detect the set of M pulse periods $[m_1, \ldots, m_M]$ in the pulse oximetry signal corresponding to the sets of pulse samples $p^m_{i\to j} = [p_i; p_j]$ as follows. As the distance $j - i$ between the peaks varies even within one acquisition, we use the average peak-to-peak distance $D = mean(j - i) \quad \forall i, j$ with $0 \leq i < j \leq K$ to map all pulse periods $p_{i\to j}$ to the same interval

$$\overline{p^m_{i\to j}} = p_i \ldots p_j \to p_1 \ldots p_D. \tag{A.2}$$

To preserve the shape of every pulse signal in an optimal way, we use cubic spline interpolation to conduct this mapping to the normalized pulse shapes. To reconstruct a normalized pulse shape $\hat{p}$ from $m = 1 \ldots M - 1$ pulse periods $\overline{p_{i\to j}}$, we use a weighted average of all normalized pulse shapes, where the weight is defined by the deviation of the original shape period length to the average peak-to-peak distance

$$\hat{p} = \frac{1}{\Omega} \sum_{\forall m \in M} w_m \cdot \overline{p^m_{i\to j}} \tag{A.3}$$

$$w_m = 1 - \frac{|D - (j - i)|}{D}, \quad \Omega = \sum_{\forall m \in M} w_m. \tag{A.4}$$

The normalized pulse phase signal $\overline{p}$ can then be retrieved by mapping $\hat{p}$ to every peak-to-peak interval of M accordingly by spline-interpolation. Figure A.2b shows an example for resulting normalized pulse phases from given input data.

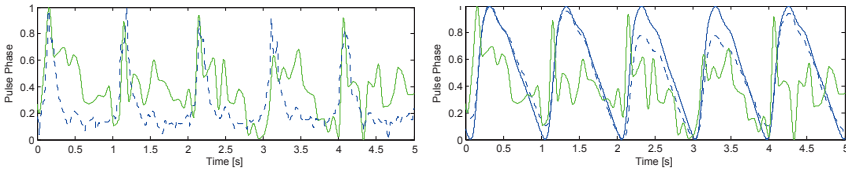

(a) Signal Calibration (b) Normalized Pulse Signal

Figure A.2: Left: arterial flow signal extracted from pulse oximetry (blue, dashed) used for time calibration with the Doppler signal (green, solid). Right: normalized pulse phase $\overline{p}$ (blue, solid) retrieved from Doppler data (green solid) and pulse oximetry (blue, dashed) for a freehand scan of the carotid artery.

A.3.2 Ultrasound Sample Selection

Before reconstructing a final intensity value, we have to select and weight contributing samples for every voxel based on spatial and temporal constraints. Every sample has a position s_j, normalized pulse value $\bar{p}_j$ and an intensity value $I(s_j)$. We first select samples for every voxel based on the voxel position in the sample coordinates. To do so, we set an ellispoid around every sample, representing its corresponding influence region

$$G_s(v_i, s_j) = \begin{cases} K(v_i, s_j) & \text{if } \frac{\left(v_{i,x}^{s_j} - s_{j,x}\right)^2}{d_{mx}^2} + \frac{\left(v_{i,y}^{s_j} - s_{j,y}\right)^2}{d_{my}^2} + \frac{\left(v_{i,z}^{s_j} - s_{j,z}\right)^2}{d_{mz}^2} \leq 1 \\ 0 & \text{otherwise,} \end{cases} \tag{A.5}$$

where s_j is the position of sample j in volume coordinates and $v_i^{s_j}$ the i-th voxel position in coordinates of sample j. The maximum spatial distances d_{mx}, d_{my}, d_{mz} to the sample location are set according to the axial, lateral and elevational resolution of the ultrasound data, defined by the transducer and acquisition properties [9] given by our US system (see Sec A.3.4). We define the spatial weight of every US sample with respect to a target voxel based on the voxel position in relation to a three-dimensional exponential decay centered at the sample position $s_{j,x}, s_{j,y}, s_{j,z}$ of the current scanline ray sample j

$$K(v_i, s_j) = \frac{1}{(2\pi)^{\frac{3}{2}} |B|^{\frac{1}{2}}} e^{-\frac{1}{2}(v_i^{s_j} - s_j)^T B^{-1} (v_i^{s_j} - s_j)}, \quad B = diag(\sigma_x^2, \sigma_y^2, \sigma_z^2). \tag{A.6}$$

The spatial variances are set to $\sigma_x = \frac{1}{2} d_{mx}, \sigma_y = \frac{1}{2} d_{my}, \sigma_z = \frac{1}{2} d_{mz}$ to assure the ellipsoid cut-off at 2σ (95.4%). By specifying these distances based on the physical properties, only samples fullfilling these prior information are contributing to the final voxel intensity.

For the temporal selection of samples, weights are retrieved from a linear decay, according to the distance of the normalized pulse phase sample point $0 \leq \phi \leq 1$ to the desired reconstruction point ϕ with

$$G_t(\overline{p_j}, \phi) = \begin{cases} 1 - \frac{|\overline{p_j} - \phi|}{d_{mt}} & \text{if } |\overline{p_j} - \phi| \leq d_{mt} \\ 0 & \text{otherwise} \end{cases}, \tag{A.7}$$

which enables a reconstruction for any pulse point ϕ throughout the cardiac pulse phase.

A.3.3 Normalized Backward Reconstruction

In order to obtain the final intensity value $I(v_i, \phi)$ from our (sparse) set of samples, we make use of the concept of normalized convolution. Therefore, we modifiy the orginal concept [8] and apply it as a backward-transformation. By doing so, we can incorporate our spatial and temporal weights directly, while for a forward normalized convoluation, the weights would be retrieved from the convolution of the sample space with a fixed kernel, which would be unrelated to the ultrasound physics. We calculate the cumulative intensities $I_{cum}(v_i, \phi)$ and certainties $C_{cum}(v_i, \phi)$ by traversing all input samples $S = \{s_1, \ldots, s_j, \ldots, s_N\}, s_j \in \mathbb{R}^3$ for every voxel as

$$C_{cum}(v_i, \phi) = \sum_{\forall j \in S} G_s(v_i, s_j) \cdot G_t(\overline{p_j}, \phi) \cdot C(s_j) \tag{A.8}$$

$$I_{cum}(v_i, \phi) = \sum_{\forall j \in S} G_s(v_i, s_j) \cdot G_t(\overline{p_j}, \phi) \cdot I(s_j) \cdot C(s_j). \tag{A.9}$$

Here, $C(s_j) \in [0 \ldots 1]$ is a given certainty value for every input sample s_j, representing the reliability of the underlying data sample and G_s and G_t are the spatial and temporal weighting functions. Once all voxels have been traversed, $C_{cum}(v_i, \phi)$ states the total certainty of the individual voxels. It is noteworthy that $|G_s(v_i, s_j)| \leq \frac{1}{(2\pi)^{3/2}\sigma_x\sigma_y\sigma_z}$ for a single sample contributing to the surrounding voxels, thus $C_{cum}(v_i, \phi)$ is not limited to a specific value range. Consequently, the final volume intensity values can be reconstructed as:

$$I(v_i, \phi) = \frac{I_{cum}(v_i, \phi)}{C_{cum}(v_i, \phi)}. \tag{A.10}$$

A.3.4 Experimental Setup Protocol

All experiments in this work were carried out with an open access ultrasound system (Aurotech ultrasound AS, model MANUS) with a linear array probe (128 elements - single element width 0.27 mm, height 4 mm, focal depth 30 mm, 45 aperture elements) operating at 8 MHz. For every dataset, pulse-oximetry as well as ECG data was acquired synchroneously with a combined POX-ECG system (Medlab GmbH, model P-OX100). An overview of the whole system is shown in Fig. A.1.

ECG Cross-Validation:

As ECG gating still is mostly considered as the only alternative to achieve an accurate pulse gating, we validated our calibrated pulse-oximetry signals versus ECG slopes. For 6 subjects, 2 records each were acquired. As the total blood volume in the fingertip is influenced by the relative position of the finger w.r.t. the heart, signals could change for varying positions. In

our experimental setup the overall patient position (lying on table, similar to conventional ultrasound examinations) was kept constant throughout the experiments, but the position of the fingertip changed for the two recordings to analyze POX signal changes. For the first records, the fingertip was placed at a relaxed position at the table, while for the second recordings the patients had to lift their fingers as high as possible. Scans of about $10\,s$ were acquired for each position. Subsequently, automatic pulse-oximetry to ultrasound calibration was carried out and additionally, a vessel-tracking method based on [5] employed to the ultrasound data to extract a vessel lumen diameter signal from the recorded 2D frames as an index of vessel expansion and compression. For validation, the pulse peaks were extracted manually from the ECG, the lumen diameter and our normalized pulse signals to compare the distances between the diameter signal and the ECG and POX signals respectively.

Evaluation of Resolution-Preserving Reconstruction:

Without time-domain interpolation, cardiac pulsation will either cause the appearance of a "pulsating" vessel in the 3D volume for low frame density or a loss of contour sharpness in regions where deformation is visible throughout the cardiac cycle. The consequence is that a potential diagnostic value would be falsified and the robustness and accuracy of image processing methods affected in general. Thus we evaluate the suitability of our novel normalized pulse phase signal for both cases and compare it to i) a constant volume without time-domain consideration; ii) a linear monotonic increasing pulse phase signal between subsequent pulse peaks, and iii) a linear pulse signal from mininmum to maximum peaks and vice versa. As before, scans of 6 volunteers were conducted, where for every subject both a slow (mean length 58.48s) and a fast scan (mean length 22.32 s) of the carotid artery was acquired. For all datasets, volumes were reconstructed with a spacing of $0.25\,mm$ for the four compared methods. The maximum temporal distance d_{mt} was decreased stepwise to $d_{mt} = [\frac{1}{2}, \ldots, \frac{1}{20}] = \frac{1}{2n_s}, n_s = 1 \ldots 10$, which is equivalent to a subdivision of each cardiac pulse phase in n_s steps. We compare how well the original US data is preserved in the reconstructed 3D volumes by evaluating the Mean Squared Error (MSE) of the reconstructed volumes $\in [0, 1]$ with respect to the input samples at their corresponding locations.

A.4 Results and Discussion

The results for the POX-ECG validation of all compared distances are shown in Table A.1. It can be seen that i) the peak to peak distance of the normalized pulse signal is almost identical to the ECG data (mean distance of 1.2 ms), and ii) the calibrated pulse signals have a mean deviation to the extracted diameter signal of $-34\,ms$. As the temporal resolution of the diameter signal extracted from the ultrasound data is low compared to the other signals (12 Hz compared to 100 Hz for POX and ECG signals), a standard deviation approximately equal to the ultrasound sampling period (83.3 ms) is considered as optimal, which is facilitated by the standard deviation of the peak-to-peak distances in the vessel

Distance Comparison	Finger Position			
	Relaxed		Lifted	
	$\mu[s]$	$\sigma[s]$	$\mu[s]$	$\sigma[s]$
Δ Area	-	0.1049	-	0.1023
Δ $\overline{p}$ to ECG	0.0009	0.0187	0.0016	0.0229
Δ $\overline{p}$ to Area	-0.0341	0.0774	-0.0285	0.0799
Δ ECG to Area	-0.2178	0.0858	-0.1349	0.1348

Table A.1: Signal pulse period results. Shown are the peak distances between the pulse oximetry and ECG signal, as well as the distance from the pulse oximetry and ECG signals respectively to the vessel diameter signal.

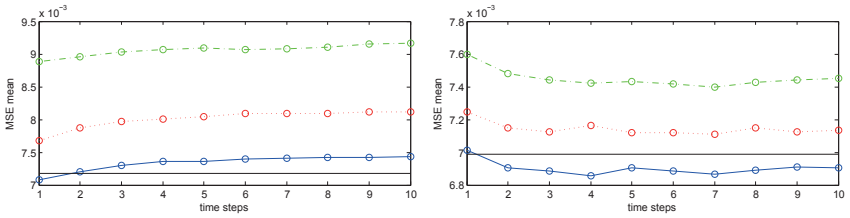

(a) Fast Scans (b) Slow Scans

Figure A.3: Reconstruction sample preservation. Shown is the mean MSE averaged over all fast/slow scans. The black solid line equals the baseline error without time-domain consideration. Compared is our method (blue, solid) to the linear pulse phase (red, dotted) and the min-to-max linear (green, dash-dotted).

diameter signal (104.9 ms). As the deviation of the normalized pulse peaks is perfectly within this range, the extracted ultrasound signal is the limiting factor to the general accuracy. This suggests that the pulse oximetry signal is well-suited for gating of ultrasound acquisitions.

Results for the evaluation of the time interpolation scheme are shown in Fig. A.3 for all methods. When comparing slow and fast ultrasound scans, it becomes clear that for the fast scans, the input ultrasound information is preserved best without time domain consideration. Disregard of the pulse information is still not recommendable, as this would potentially distort diagnostic values extracted from the volume datasets. For both slow and fast scans it can be observed that our normalized pulse phase provides the lowest errors for the different number of time steps and further preserves the input information better as a static reconstruction for slow scans. This preservation is visualized in Fig. A.4, where a reconstruction without considering pulse information is compared to our method considering pulse information. For the former, edges are appearing less sharp and details get lost by using all input samples from different pulse phases for the reconstruction. With our method, details and edges are preserved much better. Beyond that also a time-domain analysis is enabled by having distinct volume datasets for every point along the cardiac pulse phase.

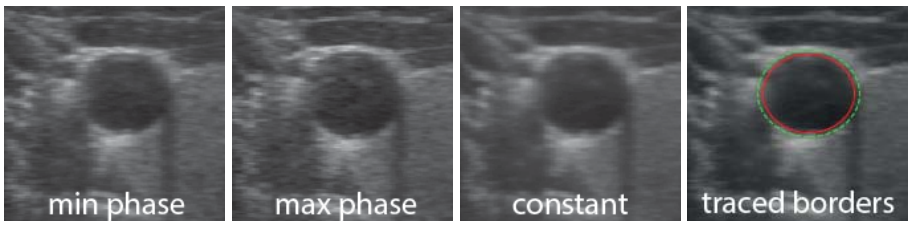

Figure A.4: Reconstruction for different pulse phases. Shown are cross-sectional slices through the vessel for min./max. vessel expansion, a volume without consideration of pulse data (constant) and overlaid contours for min./max. expansion.

Setup Robustness: In respect of the presented experiments, we did not notice significant distortions of the pulse oximetry signals as long as the patients did not move their fingers during acquisition. However, as opposed to pulse oximetry, for placement of the ECG electrodes, full attention was necessary in all experiments to provide useful signals. Thus we suggest that especially for time-critical situations, our technique could be a promising and robust alternative to classical gating. However to confirm these assumptions w.r.t to a direct clinical application, a thorough validation of the presented system is neccessary; especially in regard to different patient conditions (e.g. arrythmia or calloused finger skin) and working environments with possible distortions such as operating lights.

A.5 Conclusion

We presented a new system to reconstruct 3D+T volume data from freehand ultrasound in combination with a pulse oximetry sensor. We introduced a novel method for correlating pulse oximetry with Doppler ultrasound, enabling an accurate time-calibration on a per-record basis. We further showed how a normalized pulse phase signal can be defined based on the pulse oximetry data to be used directly within time-domain interpolation. The setup can be used to reconstruct 3D volume data for cardiac pulse phases superior compared to today's freehand approaches and delievers improved capabilities for vascular ultrasound reconstruction compared to classical ECG gating. Furthermore, the uncomfortable use of ECG electrodes can be circumvented, which allows a more extensive use of 3D+T in every-day clinical scenarios.

A.6 References

[1] Bosch, J.G., van Stralen, M., Voormolen, M.M., Krenning, B.J., Lancée, C.T., Reiber, J., van der Steen, A.F., de Jong, N.: Improved spatiotemporal voxel space interpolation for 3D echocardiography with irregular sampling and multibeat fusion. In: Ultrasonics Symposium, 2005 IEEE. Volume 2. (2005) 1232–1235

[2] Brattain, L.J., Howe, R.D.: Real-time 4D ultrasound mosaicing and visualization. In: Proc.14th intern. conf. Medical Image Computing and Computer-Assisted Intervention. (2011) 105–112

[3] Cook, L.B.: Extracting arterial flow waveforms from pulse oximeter waveforms. Anaesthesia **56**(6) (2001) 551–555

[4] Forsberg, F.: Ultrasonic biomedical technology; marketing versus clinical reality. Ultrasonics **42** (2004) 17 – 27

[5] Guerrero, J., Salcudean, S.E., McEwen, J.A., Masri, B.A., Nicolaou, S.: Real-time vessel segmentation and tracking for ultrasound imaging applications. Medical Imaging, IEEE Transactions on **26**(8) (2007) 1079–1090

[6] Karadayi, K., Hayashi, T., Kim, Y.: Automatic image-based gating for 4D ultrasound. In: Engineering in Medicine and Biology Society, 2006. EMBS '06. 28th Annual International Conference of the IEEE. (2006) 2388 –2391

[7] Klein, T., Hansson, M., Navab, N.: Modeling of multi-view 3D freehand radio frequency ultrasound. In: Proc.15th intern. conf. Medical Image Computing and Computer-Assisted Intervention. (2012) 422–429

[8] Knutsson, H., Westin, C.F.: Normalized and differential convolution. In: Computer Vision and Pattern Recognition, 1993. Proceedings CVPR '93., 1993 IEEE Computer Society Conference on. (1993) 515 –523

[9] Ng, A., Swanevelder, J.: Resolution in ultrasound imaging. Continuing Education in Anaesthesia, Critical Care & Pain **11** (2011) 186–192

[10] Prager, R., Ijaz, U., Gee, A., Treece, G.: Three-dimensional ultrasound imaging. Proc. Institution of Mechanical Engineers, Part H: Journal of Engineering in Medicine **224** (2010) 193–223

[11] Solberg, O.V., Lindseth, F., Torp, H., Blake, R.E., Nagelhus Hernes, T.A.: Freehand 3D ultrasound reconstruction algorithms - a review. Ultrasound in Medicine and Biology **33** (2007) 991–1009

[12] Sundar, H., Khamene, A., Yatziv, L., Xu, C.: Automatic image-based cardiac and respiratory cycle synchronization and gating of image sequences. In: Proc.12th intern. conf. Medical Image Computing and Computer-Assisted Intervention. (2009) 381–388

[13] Treece, G.M., Prager, R.W., Gee, A.H., Cash, C.J., Berman, L.: Grey-scale gating for freehand 3D ultrasound. In: Biomedical Imaging, 2002. Proceedings. 2002 IEEE International Symposium on, IEEE (2002) 993–996

[14] Wachinger, C., Yigitsoy, M., Navab, N.: Manifold learning for image-based breathing gating with application to 4D ultrasound. In: Proc.13th intern. conf. Medical Image Computing and Computer-Assisted Intervention. (2010) 26–33

B

A Quadratic Energy Minimization Framework for Signal Loss Estimation from Arbitrarily Sampled Ultrasound Data

Christoph Hennersperger[1], Diana Mateus[1,2], Maximilian Baust[1], and Nassir Navab[1]

[1] Chair for Computer Aided Medical Procedures (CAMP), Technische Universität München, Germany.
[2] Institute of Computational Biology, Helmholtz Zentrum München, Germany.

Our contribution. The main contributions of this publication, including the main idea, the reconstruction of confidence maps, implementation, tests, and validation, were done by the author of this thesis. Discussions of implementations, refinements of utilized optimization-concepts, as well as the revision of the publication was done jointly together with the co-authors.

Abstract. We present a flexible and general framework to iteratively solve quadratic energy problems on a non uniform grid, targeted at ultrasound imaging. Therefore, we model input samples as the nodes of an irregular directed graph, and define energies according to the application by setting weights to the edges. To solve the energy, we derive an effective optimization scheme, which avoids both the explicit computation of a linear system, as well as the compounding of the input data on a regular grid. The framework is validated in the context of 3D ultrasound signal loss estimation with the goal of providing an uncertainty estimate for each 3D data sample. Qualitative and quantitative results for 5 subjects and two target regions, namely US of the bone and the carotid artery, show the benefits of our approach, yielding continuous loss estimates.

B.1 Introduction

Many algorithms in computer vision and image processing, such as diffusion image filtering [7] or random walks for image segmentation [1], require the minimization of quadratic energy terms of the form

$$E(x) = \frac{1}{2}x^T Ax - x^T b, \tag{B.1}$$

where $x \in \mathbb{R}^m$ denotes the solution vector, given a positive definite system matrix $A \in \mathbb{R}^{m \times m}$ and a vector $b \in \mathbb{R}^m$. Such energies are usually defined on a graph shaped as a square lattice resembling the spatial structure of the image data. However today, and especially in medical imaging, the concept of an image extends to sensor readings that sample the space arbitrarily, e.g. in SPECT and ultrasound data. For the latter, single 1D rays, so-called *scanlines*, are processed independently and get converted into 2D images subsequently. This scan-conversion step is based on the transducer geometry, which is often non-rectangular, e.g. in case of curvilinear or phased-array transducers. Furthermore, the image planes of 3D freehand sweeps are hardly parallel, as straight trajectories are difficult to maintain. Therefore, the irregularly sampled data is usually *compounded* prior to further processing, i.e. image intensities are interpolated w.r.t. a rectangular grid. We argue that for the minimization of a quadratic energy involving US data, such as for segmentation [1], signal loss estimation (SLE) [3], or Speckle reduction [8], compounding is not only unnecessary, but also counterproductive, as interpolation can imply a potential loss of information [4]. The main contribution of this work is therefore a framework for solving arbitrary quadratic energy minimization problems in a ray-based and thus compounding-free manner. Moreover, we propose an ultrasound-specific construction of directed graphs allowing for the definition of direction and potential dependent edge weights (e.g. weights that resemble the direction of propagation of the US rays). The aforementioned generalizations pose additional challenges: i) A specialized neighbor search is

This work was partially supported by the EU 7th Framework, No. 270460 (ACTIVE), and the Bavarian state program Leitprojekte Medizintechnik (BayMED).

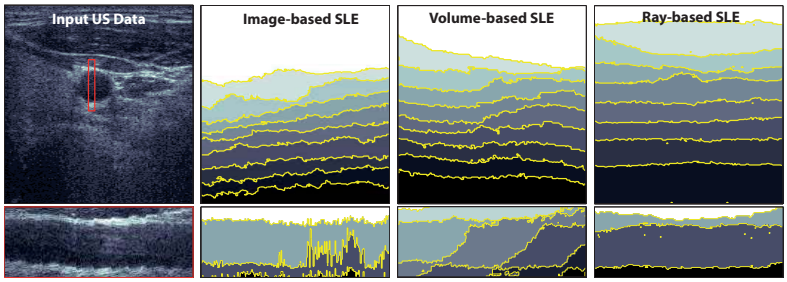

Figure B.1: **Signal Loss Estimation for Carotid Artery 3D US** From left to right: Original ultrasound data, loss estimates obtained by a frame-based and a compounding-based application of [3], as well as our method. Shaded areas show confidence values quantized into 10 equidistant steps. The red window in the US image marks the longitudinal view shown in the second row. It can be clearly observed that ray-based SLE are the most consistent along the sweep direction.

required, as a straightforward nearest neighbor (NN) search does not reflect the US specific image formation process. ii) The symmetry and the linearity of Eq. (B.1) are not necessarily preserved, which requires adaption of the employed optimization algorithms. In this regard, there has been previous work where most relevant is the one of Singaraju *et al.* [5], who employed a Newton-descent like iterative algorithm. Here, we also propose to deal with the problem in an iterative fashion using a modified version of the conjugate gradient method, with re-initialization, cf. Sec. D.2.

To demonstrate its applicability, the proposed framework is used for signal loss estimation in three-dimensional US sweeps, where a value of "confidence" is estimated for each pixel following a random walker formulation [3], cf. Sec. B.3. As observed in Fig. B.1 and in contrast to the proposed method, the naive application of the approach of [3], either frame-wise, or via a compounding, leads to either discontinuities, or compounding-related artifacts in frame direction, respectively. Thanks to the construction of a directed graph network on the spatially irregular samples and through the proper definition of graph weights, our method instead achieves continuity along the trajectory.

B.2 Quadratic Energies on Irregular Ultrasound Graphs

The proposed framework consists of two main steps: i) building a connected graph from arbitrary US samples in 3D space, and ii) making use of this graph structure to effectively minimize quadratic energy terms in an iterative update scheme directly on the graph.

Directed Graph-Network for 3D Ultrasound. For 3D ultrasound data, a graph can be constructed from either a *compounded* dataset or directly from the original ultrasound samples lying in 3D space. Although the graph construction is easier in the former case, the latter is by far better suited to ultrasound data, as

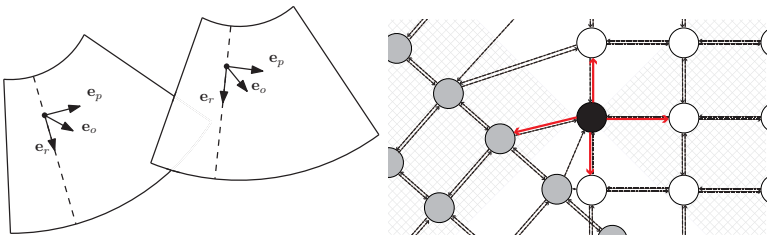

Figure B.2: **Graph construction** from two views, simplified to a 2D plane. **Left:** Two views with exemplary local coordinate systems defining the orthants. **Right:** Graph constructed from the two views (white and grey nodes) at their intersection area. The bold red arrows show all *outgoing* edges from one specific node (black), and the grey grid areas indicate the orthants for the marked node.

in US imaging, single 1D rays are acquired independently. With an irregular graph built from individual samples in 3D space, minimization problems can be solved efficiently, yielding results directly corresponding to the input data.

Thus, we aim to construct a graph directly from K arbitrarily spaced US rays (*scanlines*), where each of them consists of N ultrasound sampling points. The sampling points will be denoted by $\mathbf{x}_{k,l} \in \mathbb{R}^3$ with corresponding intensity values $I_{k,l}$, where $k = 1,\dots,K$ and $l = 1,\dots,N$. Each of these sampling points will be associated to a node n_i ($i = 1,\dots,M$; $M = KN$) in the graph $\mathcal{G} = (\mathcal{N},\mathcal{E},\mathcal{W})$, where $\mathcal{N}$, $\mathcal{E}$, and $\mathcal{W}$ denote the set of nodes, edges, and weights, respectively. Further, we introduce the bijection

$$\Theta : \{1,\dots,N\} \times \{1,\dots,K\} \to \{1,\dots,M\}, \quad (k,l) \mapsto i = \Theta(k,l) \tag{B.2}$$

in order to number all nodes. We call two nodes n_i and n_j *connected* if there exists an edge $e_{i,j}$ or $e_{j,i}$ in $\mathcal{E}$. It is important to note that we construct a *directed* graph, as ultrasound imaging is directional by nature with ultrasonic waves traversing through tissue originating from the transducer. Thus we explicitly make a difference between $e_{i,j}$ going from n_i to n_j and $e_{j,i}$ going from n_j to n_i. Each node is connected to six neighbors via *six outgoing* edges. As US samples are lying arbitrarily in 3D space, a naive nearest neighbor search does not resemble the US-specific image formation process. Thus, we propose a different approach and endow every node (or equivalently every sampling point) with a local coordinate system which is given by the orthonormal vectors $\mathbf{e}_r, \mathbf{e}_p, \mathbf{e}_o \in \mathbb{R}^3$, cf. Fig. B.2. The vector $\mathbf{e}_r$ is pointing into the direction of the ray, $\mathbf{e}_p$ is orthogonal to it and lies within the acquisition plane, and $\mathbf{e}_o$ is orthogonal to both of them. Given a node n_i we can now define its six neighboring nodes as follows. At first we connect it to its upper and lower neighbors n_U and n_L w.r.t. the scan line direction $\mathbf{e}_d$. Let $(k,l) = \Theta^{-1}(i)$, then $n_U = n_{\Theta(k,l-1)}$, and

$n_L = n_{\Theta(k,l+1)}$. Based on $\mathbf{e}_p$ and $\mathbf{e}_o$ we define the four orthants

$$\Omega_N = \left\{(k',l') : \mathbf{e}_o = \arg\min_{\mathbf{p}=\pm\mathbf{e}_o,\pm\mathbf{e}_p} \angle(\mathbf{x}_{k',l'} - \mathbf{x}_{k,l}, \mathbf{p})\right\}, \tag{B.3}$$

$$\Omega_S = \left\{(k',l') : -\mathbf{e}_o = \arg\min_{\mathbf{p}=\pm\mathbf{e}_o,\pm\mathbf{e}_p} \angle(\mathbf{x}_{k',l'} - \mathbf{x}_{k,l}, \mathbf{p})\right\}, \tag{B.4}$$

$$\Omega_E = \left\{(k',l') : \mathbf{e}_p = \arg\min_{\mathbf{p}=\pm\mathbf{e}_o,\pm\mathbf{e}_p} \angle(\mathbf{x}_{k',l'} - \mathbf{x}_{k,l}, \mathbf{p})\right\}, \tag{B.5}$$

$$\Omega_W = \left\{(k',l') : -\mathbf{e}_p = \arg\min_{\mathbf{p}=\pm\mathbf{e}_o,\pm\mathbf{e}_p} \angle(\mathbf{x}_{k',l'} - \mathbf{x}_{k,l}, \mathbf{p})\right\}, \tag{B.6}$$

in which we aim to find the nearest neighbors in the different search directions and choose n_N, n_S, n_E, and n_W as the nodes corresponding to the samples with minimal Euclidean distance to $\mathbf{x}_{k,l}$ within the corresponding orthants. The orthants can be seen as search regions defined by the coordinate quadrant bisections, which are used to find neighbors orthogonal to the rays. It is important to note that the search in these local spaces results in an irregular directed graph, as for different local coordinates, neighbors will be found differently (see Fig. B.2).

Minimization of Quadratic Energies on a Directed Graph. Recall that the minimization of the general quadratic energy in (B.1) corresponds to solving the equation system $Ax = b$, where A represents the graph Laplacian. In order to do so, we propose a meta-algorithm that can be combined with any iterative solution technique, which only requires a method implementing the matrix-vector multiplication Ax, such as the well-known conjugate gradient method. We note that the solution vector x contains the so-called node potentials defined by $p_i = P(n_i)$, where $P : \mathcal{N} \to [0,1]$, and the interpretation of these potentials depends on the application (cf. Sec. B.3). In order to derive a method implementing Ax, we first introduce the directional derivatives w.r.t. its local neighborhood

$$\nabla_\xi p_i := p_\xi - p_i, \quad \text{where} \quad \xi \in \mathfrak{N}_i = \{U, L, N, S, E, W\}. \tag{B.7}$$

This definition allows us to write the directed and potential dependent graph Laplacian (corresponding to $\mathcal{G}$) at p_i as

$$\Delta p_i = \sum_{\xi \in \mathfrak{N}_i} \left[\mathbf{1}(p_i > p_\xi) w_{i\xi} + \mathbf{1}(p_i \leq p_\xi) w_{\xi i}\right] \nabla_\xi p_i, \tag{B.8}$$

where $\mathbf{1}(p_i > p_\xi) = 1$, if $p_i > p_\xi$, and $\mathbf{1}(p_i > p_\xi) = 0$ otherwise, which activates or deactivates the directed edges based on sign of the potential difference. The computation of Δp_i can be parallelized and thus efficiently implemented on a GPU. As Δp_i corresponds to the $i-$th row of Ax, the proposed operation essentially represents a GPU-based *black box* for this matrix vector multiplication. The next step for solving (B.1) consists now of selecting an appropriate iterative solver which can be combined with the aforementioned black box. An obvious, but slow candidate would be a classical gradient descent, i.e., $x^{t+\tau} = x^t - \tau(Ax^t - b)$. In contrast to this, we employed a conjugate gradient method.

It is important to note that in case of a regular grid of voxels, symmetric edge weights, and no dependency on the potentials, the corresponding graph

Laplacian A would be symmetric positive definite. Thus, the plain application of the conjugate gradient method would already be sufficient for minimizing (B.1). The symmetry of A is, however, not preserved in the case of potential-dependent edge weights in a directed graph. From a theoretical point of view, this would prohibit the application of the conjugate gradient method without any further modification. Thus, we propose to augment the selected iterative solver, in our case the CG method, with an additional outer iteration loop. For each outer cycle, a set of active edges is determined by evaluating the indicator function in (B.8) once for the whole graph. This set of active edges is then kept constant for the next η iterations of each inner cycle, where the CG update scheme is started from the initial node potentials first and then updated accordingly with the result of the previous cycle. As for the normal descent-like approach, the update-scheme is repeated until the residual is below a threshold ϵ. We found experimentally that this procedure yields satisfactory results, as demonstrated in Fig. B.3 and Fig. B.4.

B.3 Signal Loss Estimation from Ultrasound

We show how the proposed framework can be applied to the specific task of signal loss (or uncertainty) estimation for 3D ultrasound imaging, where the goal is to retrieve a coefficient describing the reliability of the ultrasound signals at the different sample positions. The reliability of the ultrasound signal drops with depth as the signal is attenuated and absorbed in tissue. However, it is also partially scattered at small interfaces, and thus the reliability is also depending on neighboring tissue and surrounding interfaces. Although similar to attenuation estimation, signal loss estimates do not represent an absolute value, but the *relative confidence* of the correspdonding sample, in reference to a certainty of 100% at zero depth. As the SLE are retrieved globally for the whole acquisition, application fields for these values are extensive, with the most obvious ones being visualization, registration and segmentation of ultrasound data, where the values can be directly incorporated as a weighting term based on the confidence values assigned to the ultrasound samples.

The first step to use the proposed framework is to define weights and border conditions, such that the result of the minimization scheme yields a mapping of every ultrasound sample position to a reliability factor $\in [0, 1]$. The edge weights w_{ij} are defined to model ultrasound properties in an effective way, as inspired by [3]. To account not only for varying distances between connected nodes, but also for different incision angles of the ultrasound beams, we additionally make use of the unit vector $\mathbf{e}_r$, indicating the direction of every US ray, to evaluate the angles between compared nodes. This essentially accounts for the inherent directionality of ultrasound, where signals are similar for ray orientations which are parallel, but represent complementary information for rays which are perpendicular to each other. We define our weighting function

We also conducted experiments with the fast Jacobi method proposed by [2], but results were less convincing.

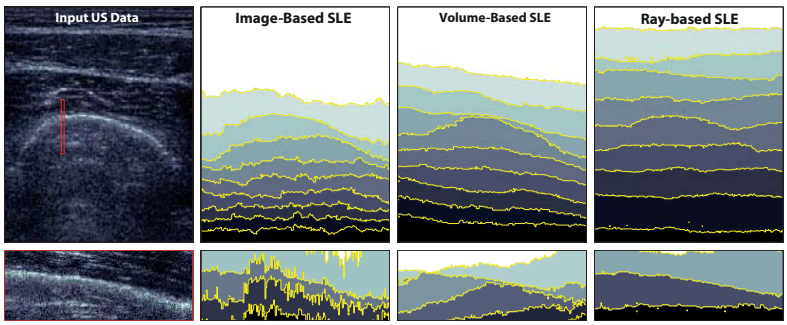

Figure B.3: **Loss Estimates for Bone Ultrasound** As for the carotid datasets (cf. Fig. B.1), cross-sectional and longitudinal slices for the compared methods (second and third column) exhibit a strong variation for image and volume bases estimates, while our ray-based method provides consistent estimates, properly modeling the bone structure also in elevational direction.

as

$$w_{\xi i} = exp\left[-\left(\frac{|I_{\theta^{-1}(\xi)} - I_{\theta^{-1}(i)}|}{\sigma} + \gamma(|\mathbf{x}_{\theta^{-1}(\xi)} - \mathbf{x}_{\theta^{-1}(i)}|(1 - \langle \mathbf{e_r}^{\xi}, \mathbf{e_r}^{i} \rangle)\right)\right], \tag{B.9}$$

where σ controls the edge weight based on the image information, γ is a penalty for nodes with high distances and inter-scanline angles, and $\mathbf{e_r}^i$ is the ray direction for node i, extending the weights in [3] to arbitrary samples in space.

For the resulting loss estimates, it is known a priori that the relative signal strength at the transducer surface should be 1, while it is expected to be ≈ 0 for all regions which are outside of the US image in axial direction. To model this conditions, two virtual nodes n_t and n_s, the transducer (source) and sink, with $p_t = 1, p_s = 0$, are added [3]. To account for these virtual nodes, the right hand side b in (B.1) is initialized with zeros except for the the entries corresponding to the first row which are initialized with $b_{\Theta(k,1)} = -w_{N\Theta(k,1)}$ in order to satisfy the transducer-related boundary conditions. With these constraints in place, we calculate all weights for the edges constructed during graph setup, and apply the optimization scheme presented in the last section to retrieve a global solution for all undefined node potentials, representing the desired loss estimates.

B.4 Results and Discussion

We provide qualitative and quantitative results for SLE in case of 3D freehand ultrasound based on the presented framework for ultrasound scans of the carotid arteries, as well as the femoral bone. While in the former case, the lumen of the vessel is mostly surrounded by soft tissue, bone structures are strong reflectors which should result in clear steps in the signal loss estimates. For both applications, we acquired 5 datasets from different subject, each with

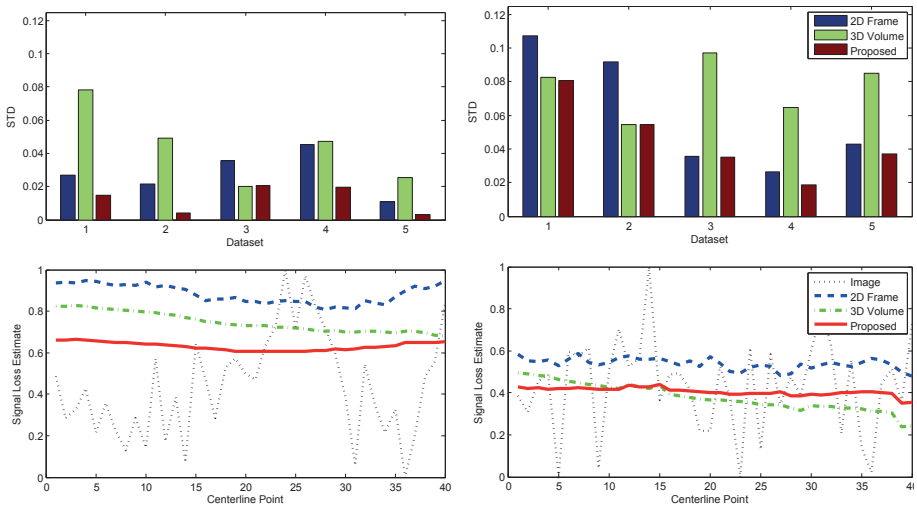

(a) Carotid Artery (b) Bone

Figure B.4: **SLE Variations along centerlines** The first row shows the standard deviations of SLE based on 2D images (blue), 3D volumetric (green) and 3D ray based (red) methods, respectively. The second row shows the actual SLE values for all methods along the centerline for carotid and femoral bone datasets 4.

a freehand US setup consisting of an Ultrasonix RP scanner providing scanline data coupled with an Ascension electromagnetic tracking device.

In terms of a quantitative evaluation, we compare estimates obtained using our approach to a method for uncertainty estimation from linear 2D ultrasound images [3] and to an extension of this method, which is applied on a volumetric (compounded) grid, where we used a backward-warping algorithm [6] prior to loss estimation. Qualitative results for exemplary cases are shown in Fig. B.1 for the carotid artery, and in Fig. B.3 for the femoral bone. We manually extract centerlines for the target structures of interest (carotid artery / bone) and evaluate the standard deviation of the extracted loss values along the acquired trajectories, as these should stay constant within the target structures. Fig. B.4 shows the deviations of SLE values for the individual datasets, for which the standard deviation of all analyzed carotid records yields 0.00144 for the proposed method compared to 0.0483 and 0.0300 for volume and frame based approaches, as well as 0.0487 compared to 0.0780 and 0.0657 for the bone datasets.

The results show that our method provides continuous results, modeling target structures better than the two compared methods. In regard of the applicability of our proposed framework, the results show that the graph-structure is well-suited for its application to ultrasound, and may yield better performance due to avoiding compounding of the data. Besides the presented application, other fields can be directly considered, where the already mentioned SRAD [8] and graph-based segmentation [1] are just two examples.

B.5 Conclusion

While today, processing methods reyling on compounding-based US are still common, interpolation of the data on a regular grid is unneccessary and potentially destroys useful information. In this work, we presented a completely compounding-free optimization framework for general quadratic energies. By constructing an irregular, directed graph from the ultrasound data, US-specific properties can be modeled effectively, as shown for the application of signal loss estimation. Our proposed optimization scheme is directly applied on the graph structure in a parallel fashion and thus facilitates the global optimization of energies in an efficient way. As the framework enables a fast adaption to other problems in ultrasound imaging, we hope that this work helps to start a paradigm change to fully compouding-free processing of ultrasound data. Future research might include the application of this technique to other modalities comprising irregular sampling, as well as the investigation of different iterative solvers.

B.6 References

[1] Grady, L.: Random walks for image segmentation. Pattern Analysis and Machine Intelligence, IEEE Transactions on **28**(11) (Nov 2006) 1768–1783

[2] Grewenig, S., Weickert, J., Schroers, C., Bruhn, A.: Cyclic schemes for PDE-based image analysis. Technical report, Technical Report 327, Department of Mathematics, Saarland University, Saarbrücken, Germany (2013)

[3] Karamalis, A., Wein, W., Klein, T., Navab, N.: Ultrasound confidence maps using random walks. Medical Image Analysis **16**(6) (2012) 1101 – 1112

[4] Prager, R., Gee, A., Treece, G., Berman, L.: Freehand 3D ultrasound without voxels: volume measurement and visualisation using the Stradx system. Ultrasonics **40**(1–8) (2002) 109 – 115

[5] Singaraju, D., Grady, L., Vidal, R.: Interactive image segmentation via minimization of quadratic energies on directed graphs. In: Computer Vision and Pattern Recognition, 2008. CVPR 2008. IEEE Conference on. (June 2008) 1–8

[6] Solberg, O.V., Lindseth, F., Torp, H., Blake, R.E., Nagelhus Hernes, T.A.: Freehand 3D ultrasound reconstruction algorithms - a review. Ultrasound in Medicine and Biology **33** (2007) 991–1009

[7] Weickert, J., Romeny, B., Viergever, M.: Efficient and reliable schemes for nonlinear diffusion filtering. Image Processing, IEEE Transactions on **7**(3) (Mar 1998) 398–410

[8] Yu, Y., Acton, S.: Speckle reducing anisotropic diffusion. Image Processing, IEEE Transactions on **11**(11) (Nov 2002) 1260–1270

C

Multi-Scale Tubular Structure Detection in Ultrasound Imaging

Christoph Hennersperger[1], Maximilian Baust[1], Paulo Waelkens[1], Athanasios Karamalis[1], Seyed-Ahmad Ahmadi[1], and Nassir Navab[1,2]

[1] Chair for Computer Aided Medical Procedures (CAMP), Technische Universität München, Germany.
[2] Department of Neurology, Klinikum Grosshadern, Ludwig-Maximilians-Universität München, Germany.

Contributions. The author of this thesis was responsible for the main ideas of a generalized framework for filter design from second order derivatives, the incorporation of confidence values for vesselness detection, as well as for the writing of the manuscript as well as all validations and tests respectively. Co-authors contributed to the solution of the generalized filter-design using the 1D Laplacian, as well as for the revision of the manuscript.

Abstract. We propose a novel, physics-based method for detecting multi-scale tubular features in ultrasound images. The detector is based on a Hessian-matrix eigenvalue method, but unlike previous work, our detector is guided by an optimal model of vessel-like structures with respect to the ultrasound-image formation process. Our method provides a voxel-wise probability map, along with estimates of the radii and orientations of the detected tubes. These results can then be used for further processing, including segmentation and enhanced volume visualization.

Most Hessian-based algorithms, including the well-known Frangi filter, were developed for CTA or MRA; they implicitly assume symmetry about the vessel centerline. This is not consistent with ultrasound data. We overcome this limitation by introducing a novel filter that allows multi-scale estimation both with respect to the vessel's centerline and with respect to the vessel's border.

We use manually-segmented ultrasound imagery from 35 patients to show that our method is superior to standard Hessian-based methods. We evaluate the performance of the proposed methods based on the sensitivity and specificity like measures, and finally demonstrate further applicability of our method to vascular ultrasound images of the carotid artery, as well as ultrasound data for abdominal aortic aneurysms.

C.1 Introduction

Ultrasound is one of the most widely used imaging techniques in clinical routine, especially in case of initial diagnosis. This is mainly due to its wide availability and ease of use. Applications are wide spread, as specialized ultrasound machines and probes are available for most fields. For trained experts, ultrasound further provides unique possibilities, compared to other imaging modalities such as Computed Tomography (CT) and Magnetic Resonance Imaging (MRI), because it facilitates real-time imaging of the patient while providing the physician with the possibility of directly controlling the image acquisition process and selecting the region of interest. Due to the interactive nature of this imaging modality, detecting and highlighting target structures, such as vessels, is of crucial importance not only for guiding novice users, but also for alleviating the daily routine of experienced examiners. In addition to this, many clinical applications, including diagnosis and treatment planning, require proper anatomical models, i.e. segmentations. However, as stated by Noble [21], ultrasound imaging still exhibits many challenges regarding the segmentation and characterization of tissue. Various approaches, including snakes [16] and active-shape models [7], rely on proper initializations to yield correct segmentations. Moreover, not only vascular procedures could greatly benefit from a visualization of vessel-like structures based on extracted tubular features [9], as this could provide physicians with similar possibilities for diagnosis as current CT-angiography, without exposing the patient to nephrotoxic contrast agents and X-ray radiation at the same time.

In order to understand why there still exist so many challenges, particularly in the case of vascular applications, it is useful to recall the basic working principle of medical ultrasound imaging. After emitting directed ultrasonic

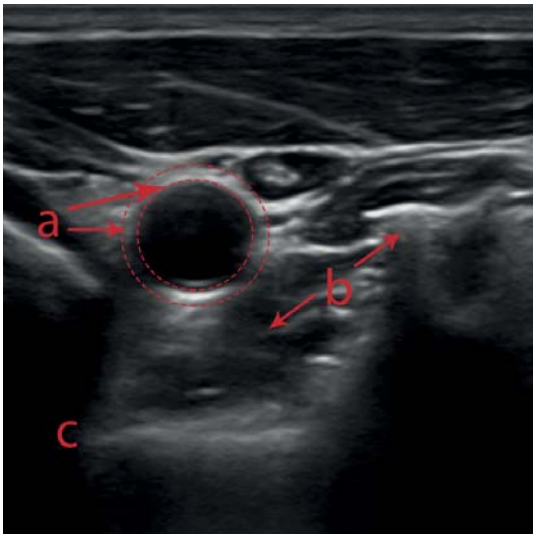

Figure C.1: Ultrasound image appearance: a) differences between horizontal and vertical gradients, where gradients perpendicular to the ultrasound beam are stronger, b) attenuation/shadowing artifacts by strong reflectors or vertical edges, resulting in beam attenuation, c) characteristic attenuation in ultrasound images for deep regions. The region marked by the dashed lines shows the bright outer border ring around the vessel lumen.

waves via a transducer into the patients' body, these waves get partially reflected at tissue interfaces, which are characterized by a change in physical properties such as the tissue density. The reflected waves are then received by the transducer again, and the final image is eventually reconstructed based on these reflections. As a consequence, this means that no separate receiver behind the target volume is necessary (in contrast to CT imaging). The main drawbacks of this image formation process are, however, that i) the signal attenuation influences the overall image appearance, resulting in deteriorated image quality for deeper regions, ii) the resolution and contrast in axial, lateral and elevational directions is not uniform, resulting in lower visibility of vertical borders compared to horizontal ones, cf. Fig. C.1, and iii) because of these distinctions, classic tubular structure detection approaches proposed for CT/MR images often do not deliver usable results for ultrasound images.

Motivated by this observation, Waelkens *et al.* [24] proposed a Hessian-based multi-scale tubular structure detection algorithm adapted to the imaging properties of carotid (3D) ultrasound. In this paper, we extend this approach in several aspects:

1. We introduce a multi-scale estimation not only with respect to the inner diameter, but also to the outer border ring thickness (see Fig. C.1). To the best of our knowledge, in all prior work, the outer ring was either not considered at all, or assumed to have a constant radius.

2. We propose a general framework for designing filter kernels for arbitrary

vascular models.

3. We further incorporate confidence maps [15] as prior information to be able to compensate for ultrasonic attenuation and artifacts within the structure detection approach.

4. Finally, we evaluate our combined structure detection approach extensively on healthy and diseased patient datasets. As these sets were acquired with ultrasound devices of different vendors (using different post-processing chains and filters), we show the applicability of our method to general (3D) ultrasound imaging.

The remainder of this article is structured as follows: in Section C.2) we discuss related work and recent advances regarding tubular structure detection approaches using different beam forming and filtering processes. We introduce our detection algorithm in Section D.2. Section C.4 then provides a quantitative comparison of our filter to the classical Hessian matrix based estimation on several carotid artery ultrasound datasets. Finally, we discuss our results (Section C.5), present important conclusions as well as future research directions (Section D.5).

C.2 Related Work

Various methods for enhancement and detection of tubular structures have been proposed. In this section, however, we focus on methods for the automatic enhancement of tubular structures and exclude those aiming at a direct segmentation or focusing on specific applications. For a recent survey on methods for ultrasound segmentation, the reader is referred to the excellent article of Noble [21]. Furthermore, we categorize prior work for enhancement of tubular structures into Hessian-based methods and methods which aim at computing certain kinds of medialness measures. While Hessian-based methods extract information directly from the second order derivatives of the image data, medialness functions try to detect the medial axis of structures with circular cross-sections, mostly by evaluating the intensity information on 1D rays emitted from seed points.

C.2.1 Medialness Measures

Pock *et al.* [22, 23] extract the cross-sectional planes of vascular structures from the two largest eigenvectors and define a medialness function based on the average gradient information sampled along a circle, which is contained in this plane. They further define a confidence weighting for the cylindrical symmetry of this measure and include an automatic parameter estimation yielding more robust estimates for cylindrical structures. Wang *et al.* [25, 26] extract vessel centerline points based on the evaluation of intensity information on radially emitted rays around a focus point (Star-algorithm), but they require the definition of intensity thresholds in order to initialize an ellipse fitting. Other, similar approaches deal with outliers on these rays by removing too low

and high radius values [5], or evaluate gradient information on the emitted rays [10, 1, 13]. Based on gradient information, vessel radius probability estimates [1, 13] and contrast-independent medialness measures [10] can be computed to extract 3D centerlines from different imaging modalities.

Methods based on initial seed point selection are usually very efficient as far as the tracking on subsequent images is concerned, but they are typically quite sensitive with respect to the choice of the seed point itself. Moreover, it should be noticed that all these methods have not been specifically adapted to ultrasound imaging and assume a homogeneous appearance of the vessel border.

C.2.2 Hessian-based Approaches

The second group of methods employs the Hessian matrix in order to retrieve "vesselness" information as initially proposed by Frangi *et al.* [8]. Frangi *et al.* use the eigenvalues of the Hessian matrix in order to identify tubular structures of various scales in two and three dimensions.

Krissian *et al.* [18, 17] combine the Hessian matrix with the structure tensor [4] to compute more continuous direction estimates. In addition to this, Bauer and Bischof [3] showed that the isotropic Gaussian smoothing used in the original vesselness measure prevents a separation of neighboring structures for higher scales. To overcome this limitation, they introduce Gradient Vector Flow [28] as anisotropic diffusion process to preserve edges at higher scales. Their assumption is, however, that the feature of interest is brighter or darker the surrounding area.

From a general point of view, it should be noticed that most approaches based on the Hessian matrix, such as [8, 18, 17, 3], make use of scale space theory, cf. Lindeberg [19] by employing $\gamma-$normalized derivatives to facilitate a direct comparison of results from different scales.

C.2.3 Proposed Approach

Although some of the aforementioned approaches have been applied to ultrasound images, cf. [18, 17, 1, 13, 5, 25, 26], none of those integrates adaptations specific to ultrasound imaging. Such an adaption is exactly the goal of this work, where we try to show how tubular structure detection algorithms can be redefined for ultrasound imaging by incorporating information about the specific characteristics of this imaging modality. A first step in this direction was presented by Waelkens *et al.* [24], who introduced a method for vessel detection in ultrasound imaging by defining an adapted filter kernel along with other ultrasound-specific modifications. In the present work, we not only extend and generalize these adaptations, but also introduce a different filter kernel approach which also accounts for different outer border ring radii adjacent to the lumen, as shown in Fig. C.1. Furthermore, we incorporate ultrasonic attenuation information by means of ultrasound confidence maps into our detection approach, which further improves vessel detection and separation.

C.3 Methods

In the following section we first briefly review the Frangi filter [8], as it can be regarded as the prototype of Hessian-based vessel filters. We then discuss the necessity to adapt vesselness approaches specifically to ultrasound and present in this context the approach of [24]. Next, we describe in detail how we can derive smoothing kernels for matched second order derivatives directly based on the Laplacian, which is the basis of our ultrasound-adapted vesselness measure (C.28) to be discussed in detail in Section C.3.3.

C.3.1 Classic Vesselness Filter by Frangi *et al.*

In the following we assume that a vessel is characterized by a dark lumen surrounded by brighter tissue. For all definitions, the Hessian matrix's eigenvalues are sorted in increasing order $|\lambda_1| \leq |\lambda_2| \leq |\lambda_3|$ and their associated eigenvectors v_1, v_2 and v_3 are assumed to be normalized, i.e. $\|v_i\| = 1$.

Let us consider the input image data I at a certain scale, i.e.,

$$I_s(p) := (K(\zeta_r) * I)(p), \tag{C.1}$$

where p denotes a pixel location and ζ_r denotes the scale parameter of a Gaussian kernel K. The subscript r indicates that the scale to be selected depends on the radius r of the "vessels of interest". In order to compute the Hessian, we have to calculate the second order derivatives. Thanks to the associativity of convolution, we can write the computation of the second derivative at a certain scale as a convolution with the second derivative of K, or more formally with a Mexican hat wavelet:

$$\frac{\partial^2}{\partial p^2}(K(\zeta_r, p) * I)(p) = \frac{\partial^2}{\partial p^2}(K(\zeta_r, p)) * I(p). \tag{C.2}$$

Let us further denote the Hessian at point p computed at a certain scale ζ_r by $H_{\zeta_r}(p)$. If p lies within a tubular structure, the eigenvalues of $H_{\zeta_r}(p)$ are non-negative and satisfy the following conditions:

$$0 \approx \lambda_1 << \lambda_2 \approx \lambda_3. \tag{C.3}$$

At a centerline point, the curvature of the smoothed data in the directions v_2 and v_3 is large, due to the intensity changes at the vessel wall, while the curvature in the direction v_1 is considerably smaller. As a consequence, v_2 and v_3 span the cross-sectional plane of the vessel and v_1 is tangential to the centerline direction.

In order to evaluate whether the criteria in (C.3) are met, Frangi *et al.* proposed the following measures:

$$F_{bl} = \frac{|\lambda_1|}{\sqrt{|\lambda_2\lambda_3|}}, \quad F_{pl} = \frac{|\lambda_2|}{|\lambda_3|}, \quad F_{st} = \sqrt{\lambda_1^2 + \lambda_2^2 + \lambda_3^2}. \tag{C.4}$$

F_{bl} indicates whether λ_1 is small in comparison to λ_2 and λ_3. F_{pl} measures that $|\lambda_2| \approx |\lambda_3|$ and thus helps to discriminate between plate-like and line-like

structures. Finally, F_{st} evaluates whether the eigenvalues are large, i.e. their relative significance compared to noise.
Finally, these expressions are combined into a *vesselness* measure

$$V(p;r) = e^{-\frac{F_{bl}^2}{2\beta^2}}(1 - e^{-\frac{F_{pl}^2}{2\alpha^2}})(1 - e^{-\frac{F_{st}^2}{2s^2}}) \in [0;1], \tag{C.5}$$

where $V(p;r) = 0$, if $(\lambda_2 \leq 0) \vee (\lambda_3 \leq 0)$, because we are only looking for a dark lumen surrounded by bright tissue.

Higher values in $V(p;r)$ indicate that p is probably a centerline point at the selected scale ζ_r. To be able to compare detection results for different scales ζ_r, the vesselness measures is computed for a given range of scales, i.e. the radii, and the total vesselness is defined as $V(p) = \max_r \; V(p;r)$. It is important to note that for comprising vesselness results computed at different scales, γ-normalized partial derivatives have to be used as proposed by Lindeberg [19].

C.3.2 Challenges for Vessel Detection in Ultrasound

Ultrasound images are composed out of individual scan lines. To image a single ultrasound scan line, an acoustic wave is emitted by the ultrasound transducer into the target tissue. The emitted waves travel through the tissue and get partially reflected at interfaces between tissues of different acoustic impedance. This reflection is the basis of diagnostic ultrasound imaging, as the reflected acoustic energy can be transformed into electric signals by the transducer and therefore eventually converted into intensity values. Modern ultrasound machines feature transducers which usually consist of not only one, but multiple piezoelectric elements which are aligned in an array. These elements are then combined in order to transmit and receive focused ultrasonic beams facilitating the enhancement of the spatial resolution at a selected depth. However, it is important to keep in mind that the formation of an ultrasound image is still based on single scan lines which are processed individually. These scan lines are finally interpolated in order to obtain the output image, which is displayed to the physician. As a consequence, ultrasound imaging differs from CT or MRI in several aspects:

1. Ultrasound imaging visualizes differences of physical properties rather than visualizing the physical tissue properties themselves. Small changes of tissue properties (scatterers), however, cause the characteristic speckle pattern in regions of homogeneous tissue, which can be used for tissue classification and characterization.

2. As the waves are partially reflected at tissue interfaces and the signal is attenuated as it traverses through homogeneous tissue, a characteristic signal drop-out is observed for deeper regions.

3. Ultrasound images typically have a higher spatial resolution in axial (beam) direction (limited by wavelength $\lambda = \frac{c}{f}$) in comparison to the lateral and elevational direction (which are limited by beam width/height

which depend on the transducer geometry and the beam focusing procedure).

4. In addition to the omnipresent speckle pattern, diffraction of ultrasonic waves for non-perpendicular incision angles at tissue-interfaces causes special interference artifacts.

As a consequence of these observations, we may draw the following two conclusions:

1. As a fraction of the ultrasonic wave is reflected at every tissue interface, the amount of energy reflected at deeper tissue interfaces will be lower compared to interfaces closer to the transducer array. In fact, this ultrasound-specific attenuation can be modeled by an exponential decay, e.g., by the Beer-Lambert law [6]. This attenuation directly affects the final ultrasound image, where deeper regions appear by default darker due to the attenuation of the signals. Although these effects are partially compensated by modern ultrasound machines (e.g. depth-specific gain compensation), the overall image quality degenerates with higher distance to the ultrasound transducer.

2. As mentioned before, all scanlines are processed individually. As beams are emitted, the resolution in axial direction is limited by the wavelength of the ultrasonic wave, which is small in comparison to the distance between neighboring scanlines. Interfaces perpendicular to the beam direction are directly imaged by reflection, while interfaces parallel to it are only detected implicitly, i.e., by observing changes of neighboring ultrasound scanlines. This results in much lower sharpness and strength of image gradients parallel to the beam direction.

Due to this directional nature of ultrasound and the inevitable signal loss in deeper areas, ultrasound imaging is considerable different to topographic imaging modalities such as CT or MRI. The fact that classical filtering techniques for the detection of tubular structures, such as [8], do not take these peculiarities of ultrasound imaging into account is thus the main motivation for this paper.

C.3.3 Design of Optimal Smoothing Kernel

For most angiographic imaging modalities, the basic assumption is that the target structure appears as a bright tubular region surrounded by darker but homogeneous intensities. In case of ultrasound images, however, the appearance of vascular structures is characterized by a dark lumen region only surrounded by a small but brighter border ring of certain thickness denoted by η. The region outside of this ring is usually characterized by areas of not necessarily homogeneous, but considerably darker intensities, mostly due to speckle patterns. As a consequence, we model all outer image points by noise, cf. Fig. C.2. Based on the aforementioned assumptions we construct an optimal vessel model to design a suitable detection method for ultrasound imaging.

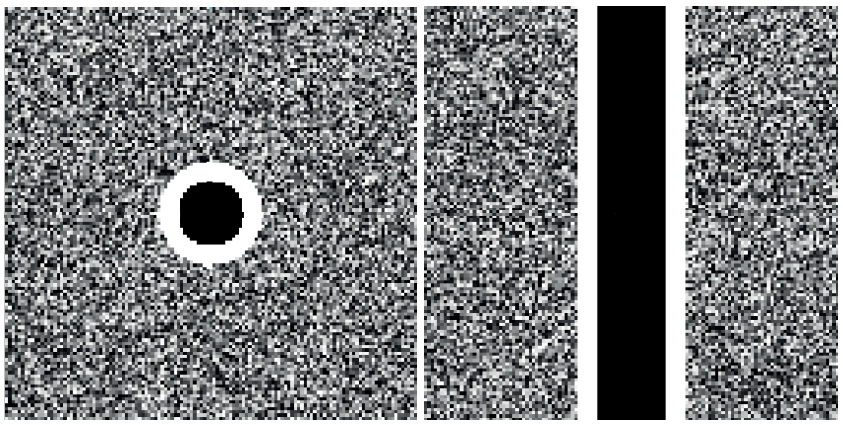

Figure C.2: Optimal ultrasound vessel model. The lumen consists of a dark region which is surrounded by a bright border ring with a given thickness. The region outside the border ring is modeled by noise.

The border width η depends on the application, the specific anatomy, e.g., higher age is associated with rising arterial wall thickness [12], and the scale, i.e., the radius r, of the structure to be detected. As already mentioned, a homogeneous tubular structure appears as a dark region with scale r surrounded by a bright ring with a defined thickness η. Thus, we choose

$$\eta = c_a r, \tag{C.6}$$

where $c_a > 0$ defines the specific relation between the radius and the border thickness.

In order to see how we can define a proper smoothing kernel, we first consider a standard Gaussian filter kernel with its second derivative, where we can observe that the kernel shape changes by adjusting the kernel parameter (i.e. varying σ values) as shown in Fig. C.3. Due to the associativity of convolution, cf. (C.2), we can directly consider the second derivative of our smoothing kernel in order to select the appropriate scale (radius) for the structures of interest. Thus an optimal kernel response should model the inner, border and outer regions in the best possible way.

While the Gaussian kernel is (practically) optimal for a single specific choice of r and η, i.e., a fixed choice of c_a, it is clearly not the best for arbitrary lumen-border relations, i.e., arbitrary choices of c_a.

Our goal is now to derive a filter kernel $g_{r,\eta}$ which is adapted to the model depicted in Fig. C.2. We will assume that $g_{r,\eta}$ is one-dimensional, which means that we want our filter to be separable. Before we start with our considerations we make the following observations:

1. The vessel model in Fig. C.2 is radially symmetric.

2. As a consequence, the filter kernel should also be symmetric, i.e.

$$g_{r,\eta}(x) = g_{r,\eta}(-x). \tag{C.7}$$

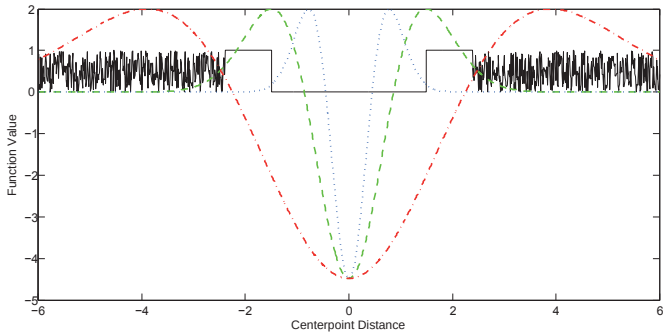

Figure C.3: Modeling of a ultrasound tubular structure with a second order Gaussian derivative. The black signal shows a 1D line through the tubular ultrasound region, where the inner lumen is dark, surrounded by a bright border ring and outside noise. The blue dotted, green dashed and red dash-dotted lines show the second derivative of Gaussians with $\sigma = 0.3$, 0.575, and 1.5.

3. Due to the this symmetry, the convolution of any signal with $g_{r,\eta}$ is equivalent to a correlation of the same signal with $g_{r,\eta}$.

4. Consequently, the same holds true for any derivative of $g_{r,\eta}$ and the convolution of a signal with

$$\frac{\delta^2}{\delta x^2} g_{r,\eta}(x) \tag{C.8}$$

is thus equivalent to a correlation with this filter.

We keep the last observation in mind and recall that the correlation of a filter with a signal attains its maximum at the position where the filter perfectly matches the signal, which is also well observed when computing the autocorrelation of a signal. Thus, our goal is to design a filter such that the second derivative of $g_{r,\eta}(x)$ is close or equal to the model, cf. Fig. C.2

$$\frac{\delta^2}{\delta x^2} g_{r,\eta}(x) \approx \frac{1}{K}(-X_{\{0 \le x < r\}} + \frac{r}{\eta} X_{\{r \le x < r+\eta\}}), \tag{C.9}$$

where X_S denotes the indicator function of a set S, i.e.,

$$X_S(x) = \begin{cases} 1 & \text{if } x \in S, \\ 0 & \text{otherwise,} \end{cases} \tag{C.10}$$

and K is chosen such that the second derivative of $g_{r,\eta}(x)$ sums up to 1. A straightforward way of obtaining a suitable kernel $g_{r,\eta}$ would be to solve the differential equation in (C.9) with appropriate boundary conditions. However, it is important to notice that the regularity of the right hand side in (C.9) directly influences the regularity of the computed filtering kernel and the regularity of it is of crucial importance, because:

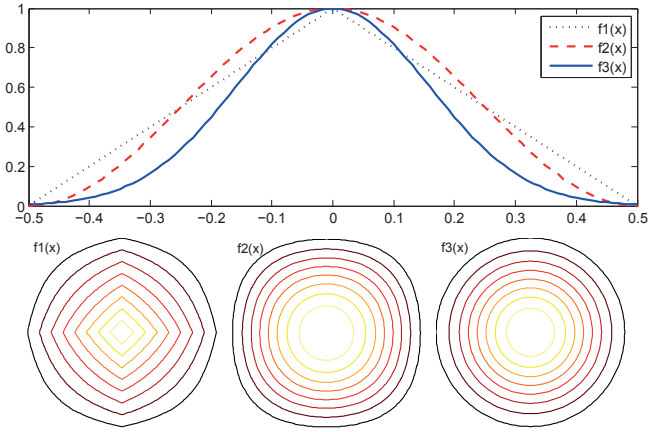

Figure C.4: Regularity and radial symmetry: The three functions $f_1(x) = 1 - |x|$ (black, dotted), $f_2(x) = (\cos(2\pi x) + 1)/2$ (red,dashed), and $f_3(x) = exp(-x^2/0.05)$ (blue, solid) evaluated on the interval $[-0.5; 0.5]$ (upper left) as well as the corresponding contour lines of $f_1(x)f_1(y)$ (lower left), $f_2(x)f_2(y)$ (lower middle), $f_3(x)f_3(y)$ (lower right) evaluated on $[-0.5; 0.5] \times [-0.5; 0.5]$. Please note that the more regular functions f_2 and f_3 cause significantly more symmetric level lines in two dimensions.

1. If the right hand side of (C.9) is not even continuous, as in the case of the proposed vessel model, the entries of the Hessian matrix (computed after filtering the image data with our separable filter) would have discontinuous entries, too.

2. As shown by Kannappan and Sahoo [14], the only rotationally invariant separable filter is the Gaussian kernel. However, by enforcing a certain degree of regularity for the right hand side of (C.9) it is possible to achieve a sufficient (but not perfect) rotation invariance of the resulting separable filter

$$g_{r,\eta}(x)g_{r,\eta}(y)g_{r,\eta}(z) \tag{C.11}$$

   as demonstrated in Fig. C.4.

For this reason we will not directly solve (C.9), but investigate

$$\frac{\delta^2}{\delta x^2} g_{r,\eta}(x) = f(x) \tag{C.12}$$

for different choices of f. We would like to emphasize at this point that we will observe in Sec. C.4 that the regularity of f is directly related to the performance of the resulting vessel filter.

Poly-Exp Kernel

In [24] an exponential of a polynomial function was used to approximate the shape of g_{r,ζ_r} of Eq. (C.9) with a smooth function

$$f(x) = \frac{1}{k} e^{P^*(x,\zeta_r)} \tag{C.13}$$

$$k = |e^{P^*(x,\zeta_r)}|, \tag{C.14}$$

where $P^*(x,\zeta)$ is a polynomial of degree $2N$ with its coefficients $\alpha_2, \alpha_4, \ldots, \alpha_N$ to be adjusted based on the lumen-border relation in (C.6)

$$P^*(x,\zeta_r) \quad = \quad \alpha_2(\frac{x}{\zeta_r})^2 \; + \; \alpha_4(\frac{x}{\zeta_r})^4 \; + \; \ldots \; + \; \alpha_{2N}(\frac{x}{\zeta_r})^{2N}. \tag{C.15}$$

The kernel parameter ζ_r is used to enable a direct correlation between the polynomial and the scale r. This relation can be found by searching for the maximum ζ_r corresponding to a defined radius $r*$ for our model

$$\zeta_r = \frac{\zeta_r^*}{r^*} r. \tag{C.16}$$

A numerical method to obtain the optimal match for this equation can be found in [24], where for the application of carotid 3D freehand ultrasound the relationship between lumen (inner tube) and arterial wall (bright border) was set to $c_a = 0.6$, resulting in $\eta = 0.6r$. For this specific relationship, a polynomial of degree 12 was found as best match while preserving the shape of (C.9)

$$P_{12}^*(x,\zeta_r) = -0.5(c_2(\frac{t}{\zeta_r})^2 + c_4(\frac{t}{\zeta_r})^4 + c_6(\frac{t}{\zeta_r})^6 + c_8(\frac{t}{\zeta_r})^8 + c_{10}(\frac{t}{\zeta_r})^{10} + c_{12}(\frac{t}{\zeta_r})^{12}), \tag{C.17}$$

with $c_2 = 8, c_4 = 16, c_6 = 42.66, c_8 = 128, c_{10} = 409.6, c_{12} = 1$. This results in a kernel-radius relation of $\zeta_r = 0.95r$. For a normal Gaussian kernel, the relationship obtained for the carotid application is $\sigma_r = \zeta_r = 0.575r$ for the best balance between inner tube and outer ring.

Adaptive Smoothing Kernel Design

Although the aforementioned filters yield optimal responses for the specific lumen-border ratio of $c_a = 0.6$, they are not generalizable to arbitrary ratios between lumen and border thickness, which would require a specific nonlinear fitting of the polynomial parameters to exponential curves for every individual tube-border relation. To avoid this fitting problem, we follow a different approach, where we directly solve the differential equation in (C.12).

In order to compute a smoothing kernel from the designed second order derivative $f(x)$, we notice that the second derivative in (C.12) is nothing else but the one-dimensional Laplacian, i.e.,

$$\frac{\delta^2}{\delta x^2} g(x) = \Delta g, \tag{C.18}$$

where we dropped the dependency of g on η and r in order to simplify the notation. The Laplace operator is then approximated using the standard finite differences discretization

$$\Delta g[x] \approx g[x-h] - 2g[x] + g[x+h] \tag{C.19}$$

which can be written as a matrix-vector multiplication:

$$\frac{\delta^2}{\delta x^2} g \approx Lg, \tag{C.20}$$

$$L = \begin{bmatrix} -1 & 1 & 0 & & \dots & & 0 \\ 1 & -2 & 1 & 0 & \dots & & 0 \\ & \ddots & \ddots & \ddots & & & \\ \dots & 0 & 1 & -2 & 1 & 0 & \dots \\ & & & \ddots & \ddots & \ddots & \\ 0 & & \dots & 0 & 1 & -2 & 1 \\ 0 & & \dots & & 0 & 1 & -1 \end{bmatrix}, \tag{C.21}$$

where we used the letter g for both the continuous and the discretized version of g. To prevent aliasing artifacts we enforce homogeneous Neumann boundary conditions such that the kernel fades out smoothly at the boundary. Thus, L is singular, which requires g to be computed with an iterative method for solving $Lg = f$, such as gradient descent, in order to compute the kernel entries[1].

It is important to note that with this approach a broad variety of target structures for second order analysis can be modeled by constructing appropriate smoothing kernels. Based on these models, the kernel can be directly constructed based on the desired lumen-border ratio. Thus, we can extend the multi-scale formulation of our detection method not only to the lumen scale r, but also to the border scale η. However, it is important to keep in mind that in the case of Gaussian kernels, a suitable rescaling of the derivatives can be found based on the concept of γ-normalized derivatives discussed by Frangi *et al.* [8]. In case of the proposed filters, a different normalization is necessary. The reason behind this is that the proposed filters are not only scale-selective with respect to the lumen radius, but also to the thickness of the vessel wall. For this reason, we propose the following normalization strategy. Based on the derivatives for a scale with assumed radius r, we use the tube model presented in Sec. C.3.3 to first compute the second order derivatives used in the Hessian matrix for this optimal model. As the maximum value of the partial derivative (for the respective model) is - based on our matched-filter design approach - estimated to be 1, we can use the maximum value of all partial derivatives as a normalization factor for the smoothed image derivatives used for vesselness estimation.

In the following we briefly describe three filters based on different assumptions, targeted to the detection of the Carotid artery as well as general vessels. A detailed comparison of results for the filters is presented in Sec. C.4.2.

[1] In order to ensure the uniqueness of a solution, an additional constraint such as $\|g\|_2 = 1$ can be enforced.

Step Kernel Inspired by Eq. (C.9), we construct a continuous approximation of the step function, where the noncontinuous steps are replaced by shallow linear transition regions

$$f(x) = \begin{cases} -\beta & for \quad x < r - \epsilon \\ \alpha & for \quad r + \epsilon \leq x < r + \eta - \epsilon \\ 0 & for \quad r + \eta + \epsilon \leq x, \end{cases} , \tag{C.22}$$

where the transition regions between the step regions have a width of 2ϵ with linear terms connecting $-\beta, \alpha$, and $\alpha, 0$, respectively. By using this approach, we avoid discontinuous steps, while enabling an easy and straightforward model which can be easily adapted to different border scales. It becomes apparent in Sec. C.4 that this choice is not optimal due to the poor regularity of f.

Piecewise Polynomial Kernel We construct the second order derivative of our smoothing filter as a piecewise smooth polynomial function with respect to the lumen and border radii r and η.

$$f(x) = \begin{cases} \alpha x^{2N} - 1 & x < r \\ 4 - \beta(x - (r + \frac{\eta}{2}))^{2N} & r \leq x < r + \eta \\ (x - \mu)^{-2N} & r + \eta \leq x \end{cases} , \tag{C.23}$$

where the parameters α, β, μ can be determined analytically with the constraints that the function values at $x = r$ and $x = r + \eta$ have equal values. In practice, we set both values to $\frac{1}{2}$ as we expect to have the highest gradients at these points.

Carotid Artery Model Kernel Recently, a learning-based method for tracking of Carotid arteries was presented [20], using a model of the intensity distribution of the appearance of carotid arteries in ultrasound images. We use this model, extracted from 100 patient scans, to directly derive a smoothing kernel optimized for carotid arteries. The model is used as basis for the kernel estimation is shown in Fig. C.5.

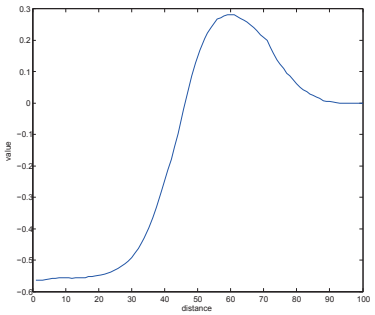

Figure C.5: Carotid artery model extracted from 100 patient datasets, as presented in [20]. To transform the intensity distribution from $[0, 1]$, we manually selected the sample with highest gradient x_{max} and normalized the value range accordingly to $k(x_{max}) = 0$.

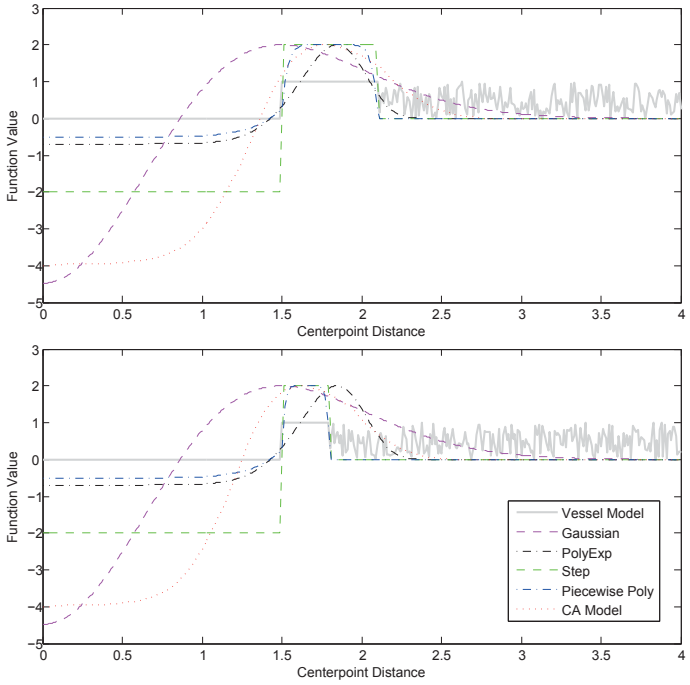

Figure C.6: Comparison of filter kernels. Shown are the second derivatives of the filter responses for a Gaussian kernel, the kernel proposed by [24], and the proposed filter kernels. The gray signal shows a 1D line through our ultrasound tube model, where the inner lumen is dark, surrounded by a bright border ring and outside noise. The Gaussian kernel clearly shows contradicting weighting of the different regions, while the other kernels show a good fitting to the black signal for the tube-border ratio $c_a = 0.6$ (top). For the smaller border ratio $c_a = 0.2$ (bottom), the piecewise polynomial and step kernels still show an optimal fit, while the other kernels cannot model the thinner border thickness properly.

Differences between kernels A comparison of all discussed kernels is depicted in Fig. C.6 for two different lumen-border ratios. The Gaussian kernel is either significantly influenced by noise outside of the vessel or it gives negative or too low positive weights to white ring points for both ratios. The fitted polynomial-exponential as well as the models presented above reflect the tube model better by weighting regions correctly for the ratio of 0.6. For a thinner border ratio, the step and piecewise polynomial kernels can be directly derived based on the different ratios, while the other kernels are static with respect to the lumen-border ratio. Our basic conclusion is here that filter kernels have to be used with care, especially when the border ring is thin compared to the inner radius. While Gaussian kernels deliver a straightforward implementation and good performance for a thick vessel border or areas of very homogeneous intensity values surrounding the lumen, for thinner walls, however, a selection based on the above criteria is preferable.

C.3.4 Physics-based adaptations

Although the choice of appropriate smoothing kernels is important to account for the specific appearance of vessels in ultrasound imaging, additional prior information with respect to the physical imaging process can be used. In the following sections, we briefly describe how the beam acquisition directory, as well as ultrasound confidence can be used to improve vesselness detection methods.

Beam Direction Dependency

As ultrasound waves are emitted in axial directions, we always expect that the received signal changes are stronger in vertical image directions compared to horizontal gradients. Based on this observation, the eigenvector v_3 of highest eigenvalue of the Hessian matrix should always point in a direction parallel to the ultrasonic beam. We propose an additional weighting factor based on the scalar product of v_3 and the ultrasound direction to account for this property:

$$F_{bDir} = |v_3^T b_{us}|, \quad F_{bDir} \in [0;1] \tag{C.24}$$

where b_{us} is the ultrasound beam direction. By evaluating the eigenvector direction, we can weaken false-positive regions, where the ratio of the eigenvalues fullfills the properties in (C.3), although the orientation of the eigenvectors is not valid, i.e. the strongest eigenvector does not point in the beam direction.

Confidence Compensation

The fraction of wave-reflection at tissue-interfaces is related to the difference in acoustic impedances. As a consequence, for example the interface between muscle and bone with a high difference in impedances will cause a higher reflection than the interface between muscle and arterial walls. As the wave traverses homogeneous tissue, subsequent interfaces are causing a characteristic attenuation of the waves. Based on this attenuation and signal drop-out, $|\lambda_2| \approx |\lambda_3| \gg 0$ will not be fulfilled, especially for higher distances to the transducer, since both eigenvalues will be small in absolute value.

For the application of tubular structure detection in ultrasound, it is desirable to integrate information about the attenuation, present in the ultrasound data, to account for these changes in the expected intensity values. A method that computes uncertainty in ultrasound imaging data by modeling the image formation and signal attenuation process was presented by Karamalis et al. [15] by means of ultrasound confidence maps based on random walks. In this work, confidence estimates are derived from the probability of random walker starting from each pixel/sample to first reach virtual transducer elements under ultrasound specific constrains. The random walks problem is formulated with an undirected weighted graph, using following edge weights:

$$w_{ij} = \begin{cases} w_{ij}^H & \text{if} \quad i,j \text{ adjacent and } e_{ij} \in E_H \\ w_{ij}^V & \text{if} \quad i,j \text{ adjacent and } e_{ij} \in E_V \\ w_{ij}^D & \text{if} \quad i,j \text{ adjacent and } e_{ij} \in E_D \\ 0 & \textit{otherwise} \end{cases} \tag{C.25}$$

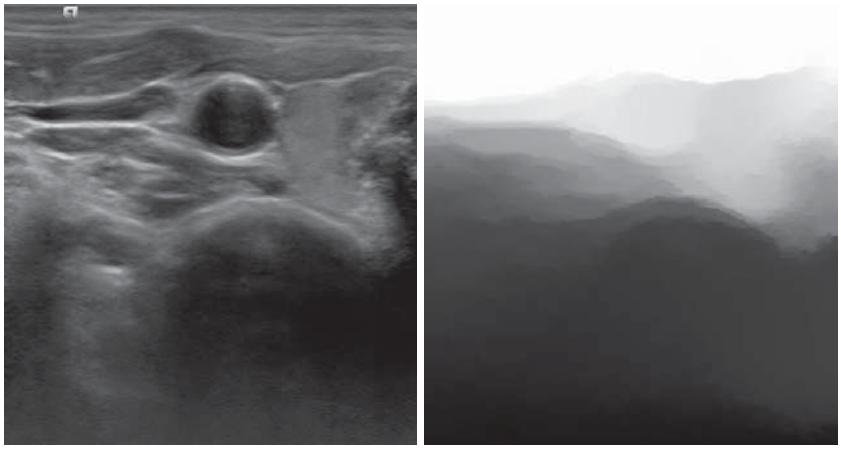

Figure C.7: Confidence map example. Shown are the input image (left) with its corresponding attenuation map (right).

The weights $w_{ij}^H, w_{ij}^V, w_{ij}^D$ for movement along horizontal, vertical and diagonal edges E_H, E_V, E_D are defined as:

$$\begin{aligned} w_{ij}^H &= e^{-\beta(|c_i - c_j] + \gamma)} \\ w_{ij}^V &= e^{-\beta(|c_i - c_j])} \\ w_{ij}^D &= e^{-\beta(|c_i - c_j] + \sqrt{2}\gamma)} \\ c_i &= g_i e^{(-\alpha l_i)}, \end{aligned} \tag{C.26}$$

where the parameter α controls the exponential penalty for depth dependent attenuation that increases with distance l_i to source nodes in the graph. The parameter γ penalizes horizontal and diagonal walks with increasing distance to the originating scanline; effectively modeling image formation along the beam direction. We extend this approach to 3D volumetric datasets in order to incorporate information about the ultrasound confidence values into the detection method. For applying the confidence estimation to a 3D grid, we connect nodes to neighbors not only in horizontal and vertical, but also in the elevational directions. Thus E_H and E_D include all edges orthogonal to the ultrasound scan direction. For all our experiments we use the recommended default values $\alpha = 2, \beta = 90$, and $\gamma = 0.06$ as presented in [15]. The analytic solution to the unknown random walks probabilities (see [11] for details) provides the desired confidence estimates to the range $[0; 1]$ and gives indication about the possible attenuation based on image content and physical properties. An example for a resulting ultrasound confidence map for an image used within our validation is shown in Fig. C.7.

With respect to the originally defined vesselness factors (see Eq. C.4), we can now look at the influence of the ultrasonic attenuation on the respective detection factors. As the factor F_{bDir} is evaluating local intensity variations only to establish a distinction between tubular and non-tubular regions, it is not influenced by global attenuation. F_{bl} compares the smallest to the two high eigenvalues and is still valid in attenuated regions, as the curvature of intensity

values should still be the smallest in tangent direction of the tube.

For F_{pl} however, the ratio of the eigenvalues can change because of speckle, attenuation or shadowing changes, which deteriorates the overall results. To account for this effect, we introduce a modified factor F'_{pl} (c.f. Eq. (C.4)) which evaluates the eigenvalues $\lambda_{c,2}, \lambda_{c,3}$ of the Hessian matrix retrieved from the confidence map instead of the image matrix. For vessel values, the ratio of eigenvalues should be approximately $\lambda_2 \approx \lambda_3$ and $\lambda_{c,2} \approx \lambda_{c,3}$. The image eigenvalues however are affected by attenuation and speckle, thus the ratio $\frac{|\lambda_2|}{|\lambda_3|} \ll 1$. In contrast to this, for confidence data the cross-sections of tubular structures are modeled as circular homogeneous regions, which are less influenced by the changes in speckle and attenuation characteristics. Thus, we set up a modified factor based on the *confidence quotient*

$$F'_{pl} = \frac{|\lambda_{c,2}|}{|\lambda_{c,3}|}, \tag{C.27}$$

which accounts for this sensitivity of the original plate-line discrimination w.r.t to noise and ultrasound speckle.

C.3.5 Combined Structure Filter

The desired result of a combined tubeness measure should give the probability of every point being a centerpoint, along with a radius estimate. The former is given as the maximum tubeness response over all analyzed scales r, η. For determining the combination of all factors, we can observe that $F_{bl}, F'_{pl}, F_{bDir}, \in [0;1]$ while F_{st} is limited by the magnitude of the Hessian eigenvalues of $I(x)$. To enable intuitive changes of all various contributing factors, we combine the individual factors to retrieve our final tubeness measure analog to the original vesselness approach:

$$T(x) = \begin{array}{l} e^{-\frac{F_{bl}^2}{2\alpha^2}}(1 - e^{-\frac{F'^2_{pl}}{2\beta}}) \\ (1 - e^{-\frac{F_{st}^2}{2\gamma}})(1 - e^{-\frac{F_{bDir}^2}{2\theta^2}}) \end{array}. \tag{C.28}$$

All parameters can be used to control the importance of the respective weight and can be adjusted to the application. For all results presented in this work however, we use equal weights $\alpha = \beta = \gamma = \theta$ not to emphasize on one of the parameters and rather focus later on the optimal combination. By setting all values to 0.5, the different factors follow a negative exponential decay, without giving preference to specific terms.

C.3.6 Implementation Considerations

As computational efficiency is one main advantage of Hessian based tubular structure detection methods, modifications should be selected carefully based on this precondition. The original approach by Frangi uses Gaussian kernels for retrieving the smoothed derivatives of the image data. Based on the derivatives, the eigenvalues are evaluated and the vesselness measure constructed. In terms

Type	4.5 10^6 voxels		8.5 10^6 voxels	
	mean [s]	std [s]	mean [s]	std [s]
Frangi	2.734	0.068	4.073	0.038
PolyExp kernel	2.694	0.022	4.532	0.272
Proposed kernels	3.104	0.051	4.939	0.045
Beam direction	2.733	0.095	4.074	0.045
Confidence	3.906	0.041	5.929	0.064
Combined	5.295	0.057	6.996	0.576

Table C.1: time comparison for evaluation of tubeness measures for one scale r.

of computation time, the convolution of the smoothed derivative kernel with the image data poses the highest demand. By using GPU capabilities, however, the required 3D convolution can be carried out efficiently by transforming both image and kernel data from the spatial into frequency domain and simply multiplying both signals there. Major processing steps within this work were implemented directly on the GPU in CUDA. Within this extensive framework, there is also a library readily available (cuFFT[2]) to conduct transformations into the frequency domain in a highly-efficient way.

With respect to our contributions, after calculating the confidence maps once off-line, incorporating the general attenuation weighting and our proposed smoothing kernel do not pose any significant increase in computation time, as our kernel can be used for convolution right away, and confidence values can be incorporated directly without additional preprocessing steps. When using our additional modifications, the modified plate-line factor F'_{pl} requires one additional convolution of the image/confidence data with a smoothing kernel. Table C.1 shows a comparison of computation times of the vesselness evaluation for our implementation with respect to different volume sizes, evaluated within this work. All evaluations were carried out on a notebook with an Intel Core i7-3612QM at 2.1 GHz, 8 GB DDR3 memory and a Nvidia GeForce GTX 650M graphics card (384 CUDA cores) with 2GB DDR5 memory.

C.4 Evaluation

In order to validate the proposed methods, we first quantitatively analyze how the adaptive filter design influences the vesselness results already without incorporation of beam direction or attenuation correction. We then evaluate how these physically motivated extensions can help to further improve results in terms of computed vesselness. Finally, we show qualitative comparisons for image data of the carotid artery as well as aortic aneurysms.

As a baseline for all results in this section, we chose the the classical vesselness filter introduced by Frangi [8] as well as the approach by Waelkens *et al.* [24]. We evaluate two different quality measures and further show -

[2]https://developer.nvidia.com/cufft

based on the dice similarity coefficient - the benefits of our approach for vessel segmentation.

C.4.1 Experimental Setup

For validation, we acquired scans of different vascular regions with US systems of different vendors, including both healthy and diseased datasets. In total, 20 healthy 3D freehand ultrasound records of the neck, 10 scans for patients with diseased carotid vessels, and 5 scans of patients with abdominal aortic aneurysms (AAA) were acquired with a commercial add-on freehand 3D ultrasound system (model CS, Curefab GmbH, Munich, Germany). For the healthy carotid artery datasets, 10 subjects were scanned, each with two different 2D ultrasound machines (GE Loqiq 7, Siemens Acuson S2000) connected to the Curefab system, scanning the carotid artery with linear array transducers and at 4 cm penetration depth. The same protocol was used for the patients with atherosclerotic disease, where five records each were acquired with the Philips IU22, and Toshiba Aplio 500 scanners connected to the Curefab system. For the patients with aortic aneurysms, all scans were taken with a Philips IU22 device and curvilinear transducers.

After acquisitions, all records were exported, and subsequently reconstructed into volumetric datasets with a distance-weighted backward-interpolation approach (voxel spacing of 0.25 mm) [27]. After reconstruction, confidence maps were calculated for the compounded volume datasets.

For ground truth generation, cross-sectional slices were then manually segmented at uniform distances of 2.5 mm per slice. On every slice, contours were manually delineated by drawing polygon border points (similar to the impoly functionality of Matlab) to segment the vessel walls. All segmentations were performed by a trained ultrasound expert, yielding accurate ground truth vessel segmentations as well as centerpoint location for the segmented slices.

Similar to [24], we evaluate the separation of centerline from background points by analyzing the *maximum* tubeness probabilities at the 3D positions extracted from the manually segmented slices:

$$q_{sep} = \frac{1}{N} \sum_{j=1}^{N} \frac{|T(c_j) - \overline{T}|}{\sigma_{T_{out}}}, \tag{C.29}$$

where c_j denotes the j-th centerline point with maximum vesselness response, $\overline{T}$ is the mean tubeness, and $\sigma_{T_{out}}$ the standard deviation of all tubeness values outside of the vessel. The division by the standard deviation is particularly important, as this measure aims for evaluating the possibility to differentiate between foreground points (vessels) and the background (specificity).

In addition to the separation, we define a second measure accounting for the detection of all points within a vessel (sensitivity). To do so, the vesselness probabilities at all inner tube points s_i enclosed by the delineated contours are evaluated based on their distance to the mean vesselness responses

$$q_{detect} = \frac{1}{S} \sum_{s_i=1}^{S} T(s_i) - \overline{T} \tag{C.30}$$

Separation from background						
Type	CA Healhty		CA Diseased		AAA	
	μ	σ	μ	σ	μ	σ
Gaussian	24.0	7.5	11.8	3.8	26.2	8.6
Poly-exp kernel	23.1	8.7	16.0	3.2	17.0	5.4
Step kernel	11.6	3.6	6.8	1.4	23.4	15.3
Piecewise kernel	20.0	7.3	13.3	3.4	24.6	16.2
CA model kernel	20.9	7.2	15.3	3.7	15.8	12.1
Detection of vessel points $[10^{-3}]$						
Gaussian	3.6	1.7	1.3	0.8	0.1	0.1
Poly-exp kernel	32.8	15.5	15.5	3.5	7.1	6.4
Step kernel	68.5	29.1	34.6	9.6	14.9	13.1
Piecewise kernel	51.0	23.4	26.0	5.4	12.7	11.3
CA model kernel	45.1	20.9	21.6	4.6	9.9	9.0

Table C.2: Mean and standard deviation for separation and detection measures. Shown are the results for all compared kernels, divided into healthy and diseased datasets for Carotid artery (CA) as well as abdominal aortic aneurysms (AAA).

with S being the total number of all segmented inner tube points.

While we rely on these two quantitative measures to evaluate the improvements of the proposed method compared to the state of the art, we also evaluate the benefits of the computed vesselness values for vessel segmentation. In order to do so, we use the points of maximum vesselness response together with the estimated vessel radii, which are obtained based on the maximum response (taken over all considered scales), in order to obtain a segmentation of the vessels. We use the dice similarity coefficient (DSC) evaluating the overlapping region of the segmentation with respect to the (manually delineated) ground truth

$$DSC = \frac{2|A \cap B|}{|A| + |B|}, \tag{C.31}$$

where A and B represent binary masks of the segmented foreground/background objects for the segmentation compared to the ground truth delineation.

C.4.2 Comparison of Filter Kernels

In order to evaluate the effects of designing custom tubeness filters targeted to specific applications, we compare the quality measures defined in Sec. C.4.1 for the discussed filter kernels. Fig. C.9 shows the resulting separation statistics and detection levels for all evaluated Carotid artery records including healthy and diseased cases, while Table C.2 lists the mean values with their corresponding standard deviations, subdivided into all the three different anatomical sites evaluated.

The overall results (all 30 datasets) for our proposed kernel as well as for the poly-exponential kernel show a drastic improvement in vessel point detection with approximately $9, 14, 18$, and 13 times higher detection for the polyExp,

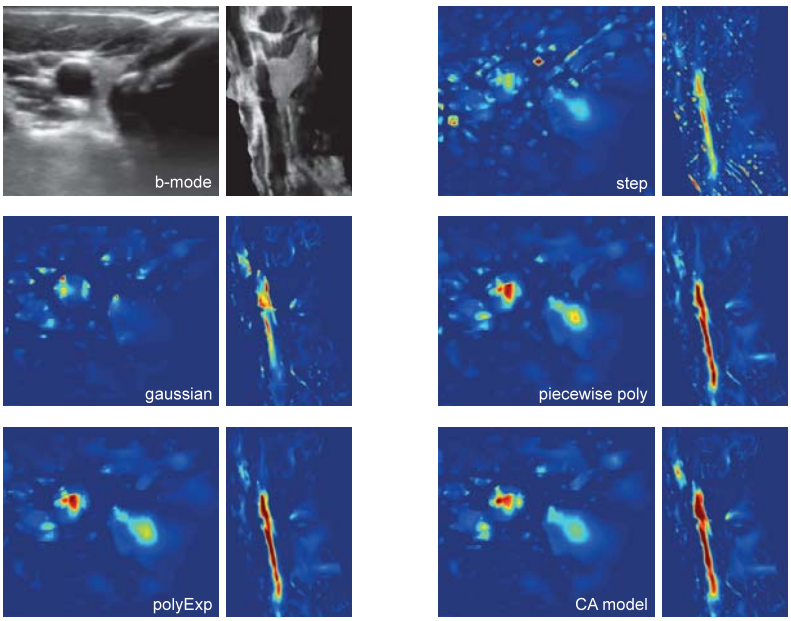

Figure C.8: Comparison of vesselness responses for different filters. Shown are cross-sectional (left images) and longitudinal (right images) slices of the input as well as the evaluated filter kernels for the original Frangi filter, the poly-exponential approach [24], the step kernel, the piecewise poly kernel, and the kernel based on the carotid artery model. When comparing these filters, it becomes visible that the filter responses for original approach are wider and only partially modeling the vessel structure. For the step kernel, false positives negatively influence the separation of the vascular structure from the background. The bad performance of the step kernel might be explained by its poor regularity in comparison to the other kernels, cf. Sec. C.3.3.

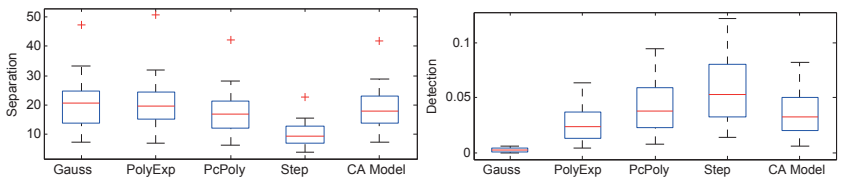

Figure C.9: Quantitative results for healthy and diseased Carotid datasets. Separation (left) and detection (right) measures for the Frangi filter using Gaussian kernels, compared to poly-exponential, step kernel, piecewise polynomial filter, as well as the carotid artery model filter.

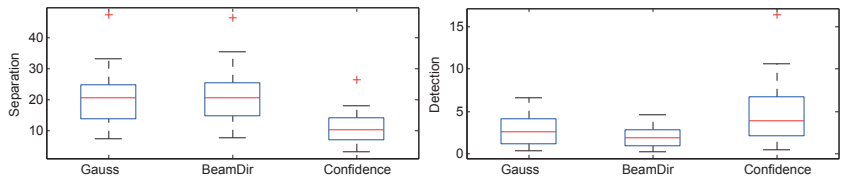

Figure C.10: Quantitative results for the evaluation of the proposed physical adaptations on all Carotid datasets. Separation (left) and detection (right) measures for the original vesselness filter as proposed by Frangi *et al.* , and the same filter augmented with beam direction compensation and confidence values, respectively.

piecewise polynomial, step, and CA model kernels respectively, compared to the original Gaussian based implementation. At the same time, the separation rates remain all within 10% mean deviation to the original implementation, with the exception of the linear step kernel. Based on these evaluations, we conclude that the piecewise polynomial model provides the overall best filter response yielding the best balance between higher detection rates while maintaining the same level of separation as the original Frangi measure.

When comparing the piecewise polynomial kernel to the poly-exponential counterpart, it is important to consider that the polyExp-kernel was designed specifically for the application of Carotid ultrasound with a lumen-border-ratio of $c_a = 0.6$.

C.4.3 Evaluation of Physical adaptations

Similar to the last section, we evaluate both quality measures for our proposed adaptations. We compare the original vesselness approach [8] as well as the piecewise polynomial filter, providing the overall best results throughout the evaluation in the last section, to the adaptations to the beam direction and compensation for different confidence values. Finally, we also evaluate our combined vesselness estimate using the piecewise polynomial kernel combined with beam direction and confidence compensation.

Results for this comparison are shown in Table C.3. It can be observed, that incorporating the beam direction term improves the separation of tube centerline points. Considering the restriction of the main Hessian eigenvector with respect to the beam direction it becomes apparent that this modification is particularly interesting for large vascular structures, such as aneurysms. In contrast to the beam direction, the confidence information clearly improves the detection rate while having partially negative effects on the separation measure. The advantages of the increased detection are, however, predominant due to higher resulting detection rates (see also Fig. C.11.)

C.4.4 Carotid Artery Segmentation

The availability of tubeness (vesselness) estimates facilitates the automatic initialization of segmentation methods, such as active contours, and provides

Separation from background						
Type	CA Healhty		CA Diseased		AAA	
	μ	σ	μ	σ	μ	σ
Gauss	24.0	7.5	11.8	3.8	26.2	8.6
Gauss + BeamDir	24.7	7.5	12.7	4.4	41.3	15.5
Gauss + Attenuation	12.7	4.4	7.7	4.1	17.1	2.2
Piecewise kernel	20.0	7.3	13.3	3.4	24.6	16.2
Combined	15.9	4.3	12.4	2.3	36.2	28.6
Detection of vessel points $[10^{-3}]$						
Frangi	3.6	1.7	1.3	0.8	0.1	0.1
Gauss + BeamDir	2.6	1.2	0.9	0.6	0.1	0.1
Gauss + Attenuation	5.0	1.9	3.8	5.1	0.1	0.1
Piecewise kernel	51.0	23.4	26.0	5.4	12.7	11.3
Combined	61.7	25.0	50.8	36.0	12.6	9.9

Table C.3: Mean and standard deviation for separation and detection measures. Shown are results for the proposed physical adaptations, divided into healthy and diseased datasets for Carotid artery (CA) as well as abdominal aortic aneurysms (AAA).

the possibility to window the volume dataset to contain mainly vascular information. For both steps, it is important that vessel points are separated properly from the background. Figure C.11 shows qualitative results for our method compared to the original Frangi filter. In addition to this, Fig. C.12 shows a quantitative evaluation of our method for the two distinct sets of healthy and diseased acquisitions of the Carotid arteries.

It can be seen that by using the proposed piecewise polynomial kernel together with the physical adaptations, the dice overlap, which indicates the suitability of the methods for the initialization of vessel segmentations, increases significantly compared to the methods proposed by Frangi *et al.* and Waelkens *et al.* . This is also confirmed by the visual inspection of the results, as our method mainly responds to the vessel with a clear maximum, while the responses for the classical method are less prominent, partially yielding responses also for other, non-vascular structures.

C.4.5 Abdominal Aortic Aneurysm Centerline Estimation

Similar to the case of head and neck arteries, estimating the centerlines of abdominal aortic aneurysms is still a challenging task due to the lack of contrast and partial missing borders in the ultrasound image data. We compare the vesselness results for our proposed method in comparison to the original approach by retrieving centerline estimates as initialization of a subsequent segmentation of the aneurysm sack.

As the lumen-border relation is not necessarily identical to the one of Carotid arteries, we use our piecewise polynomial kernel to retrieve the best matches for both radius and tube-border relations of the aneurysms. Qualitative results for one of the evaluated datasets are shown in Fig. C.13. It is clearly

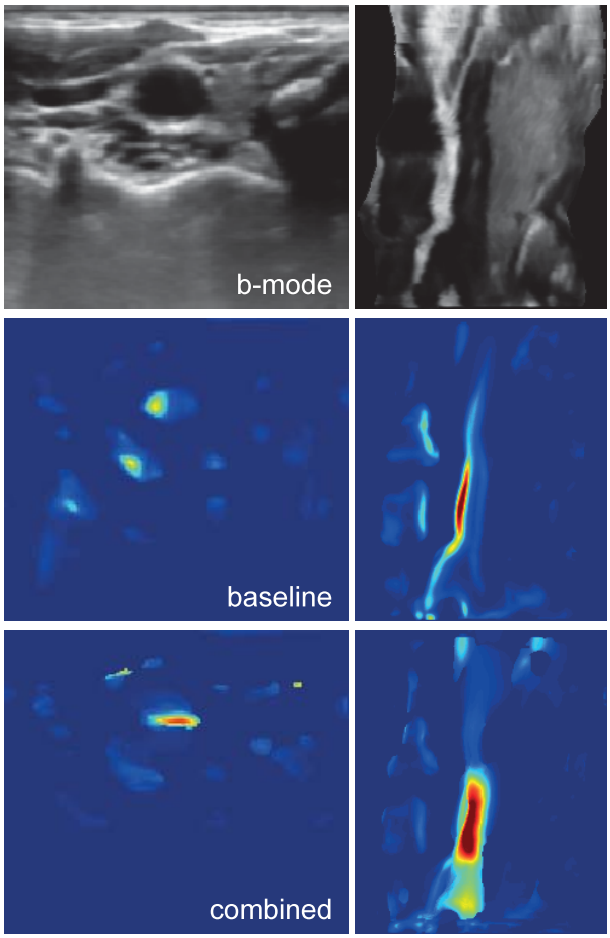

Figure C.11: Qualitative comparison of the Frangi filter (baseline) to to our proposed method using the piecewise polynomial filter combined with beam-direction and attenuation compensation. Shown are cross-sectional (left) and longitudinal (right) slices. Our method mainly responds to the vessel with a clear peak, while the baseline approach is partially also responding to other image regions.

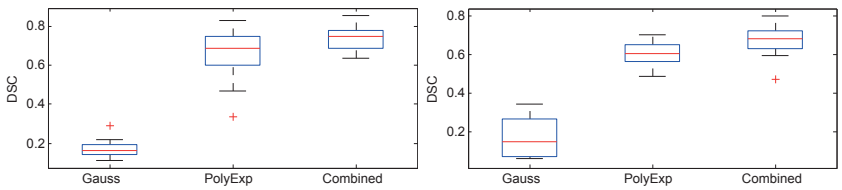

Figure C.12: Dice overlap evaluation results for healthy (left) and diseased (right) Carotid artery datasets. For both it can be observed that by using our proposed methods, the resulting dice scores for segmentation (mean 0.7138 ± 0.0741) are clearly better compared to the poly-exponential kernel (0.6434 ± 0.1059) and the original approach by Frangi (0.1713 ± 0.0643).

visible that the original vesselness approach of Frangi *et al.* fails in identifying the tube centerline points correctly, although the general aneurysm structure can be partially seen in the vesselness estimates. Even more interestingly, the polyExp kernel also fails for this case, as obviously the constant tube-border ratio of 0.6 is not valid, resulting in wrong estimations. This can be intuitively verified, as a fixed border ratio results in too wide border contributions for larger vessels, i.e. for a vessel radius of 25mm, the wall would be assumed to be $0.6 \cdot 25\text{mm} = 15\text{mm}$ thick. For our kernel, the wall thickness can be defined directly in mm, for which we found consistently a wall thickness of 1.5mm to provide highest kernel responses. This is confirmed by clinical indications, where 1.5mm is a reasonable wall thickness for abdominal aortic aneurysms. Fig. C.14 shows radius and wall thickness estimates for an abdominal case. In contrast to this, the piecewise polynomial kernel provides nice and smooth estimates of the AAA centerline. Moreover, it can be observed that background vesselness responses can be suppressed by incorporating the proposed physical adaptations.

This is also confirmed by the quantitative results for all 5 cases, shown in Fig. C.15, where again our proposed solution provides higher Dice estimates compared to the other methods.

C.5 Discussion

The scope of this work is to present modifications for an adaption of a general tubular structure detection method to (3D) ultrasound imaging. We chose Frangi's approach for our evaluations based on its widespread usage and intuitive formulation to demonstrate the advantages of our modifications.

Based on the different filter responses, we conclude that the combined measure gives the best overall performance, as it clearly separates the vessel points, while suppressing high vesselness values in other regions (false positives). This is also confirmed by the quantitative results, where the combined filter reached the best results - also regarding Dice coefficients - indicating its suitability for initializing subsequent segmentation purposes.

When considering the different adaptations separately, the confidence integration showed that the sensitivity of structure detections can be improved clearly. As this adaption uses information from the underlying confidence of the US data, it enables detection of features which would vanish otherwise. It has to be noted however, that the confidence integration is currently still based on a compounded 3D volume, which occasionally introduces small artifacts into the detection. This is why the integration of confidence values will remain as one focus in future work. The beam direction integration mainly focuses on the different appearance of vertical compared to horizontal image gradients, where the former are assumed to be sharper and more pronounced. The validity of these assumptions are justified by both the physics of ultrasound and the experimental results presented in the last section.

Besides the above mentioned modifications, we put a special emphasis on a proper smoothing kernel selection to address border appearance in ultrasound, as this has not been considered in most of the literature so far. Such considera-

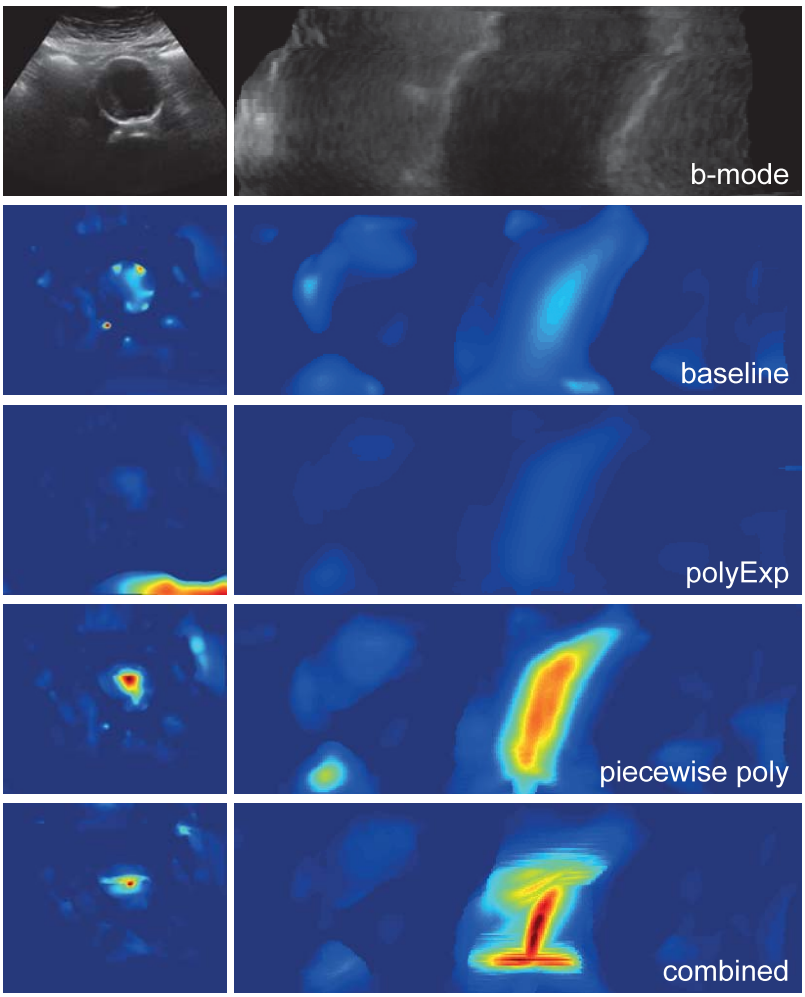

Figure C.13: Comparison of vesselness responses for different filters. Shown are cross-sectional (left) and longitudinal (right) slices of the input as well as the presented filter kernels for the original Frangi filter, the poly-exponential approach [24], the step kernel, the piecewise poly kernel, and and the kernel based on the carotid artery model. When comparing the filters, it becomes apparent that the filter responses for the original approach (and the CA model) are wider and less peaky compared to the other filters and exhibit weaker response for the deeper vessel. The strong response at the bottom of the saggittal image (bottom right) shows an artifact caused by distorted confidence estimations.

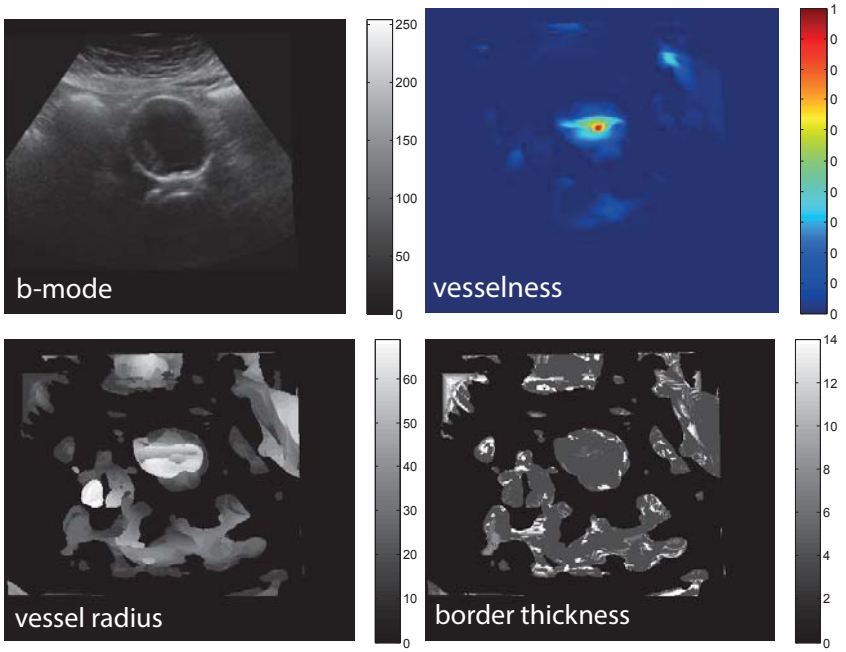

Figure C.14: Vesselness probabilities with corresponding radius and border estimates for AAA scan. Shown are the input data, as well as the combined vesselness measure and the maximum responses for border thickness and lumen radii. The values are given in voxels with a resolution of $0.375\frac{mm}{vox}$. It can be seen that border thickness estimates are consistent within the aneurysm, while radius estimates depend on the maximum response for different filter scales.

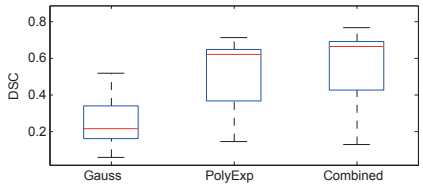

Figure C.15: Dice overlap evaluation results for abdominal aortic aneurysms. For both it can be observed that by using our proposed methods, the resulting dice scores for segmentation (mean 0.5513 ± 0.2250) are better compared to the poly-exponential kernel (0.5122 ± 0.2026) and the original approach by Frangi (0.2572 ± 0.1511).

tions are, however, not only important for any structure detection approach, but also for many other processing steps, as scale selection is an important preprocessing step for many other applications such as edge detection, segmentation, denoising, etc. In contrast to this, Gaussian filters kernels enjoy a solid theoretical justification, cf. Alvarez *et al.* [2], as well as several possibilities for an efficient implementation, but they do not give optimal responses for specific applications as it is demonstrated in this paper.

Within our evaluation, we focused on vascular 3D ultrasound as this is a major application area where tubular structure detection is desirable for a proper initialization of successive processing steps, such as segmentation for instance. As different manufacturers are using different post-processing chains, we recognized a strong variation in overall image appearance and quality, which is why we put special emphasis on evaluating our method with ultrasound systems of different manufacturers (Siemens, GE, Toshiba, Hitachi, and Philips). Unfortunately, still most of the work in the field of medical imaging is validated only based on one specific system and mostly also for a fixed imaging setup and for this reason we conducted our experiments not only based on one, but five different ultrasound systems. During the performed evaluation using these devices, we did, however, not notice an influence of the machine type on the results obtained with our proposed algorithm. This demonstrates the robustness of our approach in a realistic setup even for varying preprocessing pipelines.

With respect to the differences between healthy and diseased cases for the carotid artery datasets, some further observations can be made. By comparing the state of the art with our proposed approach, cf. Table C.3, a decrease of separation is being observed in case of our approach compared to the classical filter as far as the *healthy datasets* are concerned. The detection quality of our method, however, method remains clearly higher. As opposed to this, for the *diseased acquisitions*, the proposed combined filter provides both higher separation and detection than the other methods. This is also confirmed by the (diseased) AAA scans, where again our method provides higher levels of separation and detection. Although the total number of evaluation datasets is still too low in order to make statistically significant conclusions, a trend towards improved vesselness estimates for pathological datasets can be observed for our method in comparison to the classical Frangi filter as well as the method of Waelkens *et al.*

C.6 Conclusion

The main contribution of this work is a novel multi-scale filter that explicitly takes the ultrasound-image formation process into account. We showed that this filter is superior to standard Hessian-based methods using ultrasound imagery from 30 patients. Furthermore, we introduced several adaptations of the filter to take different ultrasound-acquisition characteristics into account, including direction-based and attenuation-based variations. In future work, we will focus on designing filters that are based on a more detailed ultrasound-image formation model. We believe that integrating 3D-based confidence

estimation into the model (based not only on 2D B-Mode frames but on the entire volume) will be especially promising.

C.7 References

[1] Abolmaesumi, P., Sirouspour, M., Salcudean, S.: Real-time extraction of carotid artery contours from ultrasound images. In: Computer-Based Medical Systems, 2000. CBMS 2000. Proceedings. 13th IEEE Symposium on. (2000) 181–186

[2] Alvarez, L., Guichard, F., Lions, P.L., Morel, J.M.: Axioms and fundamental equations of image processing. Archive for Rational Mechanics and Analysis **123**(3) (1993) 199–257

[3] Bauer, C., Bischof, H.: A novel approach for detection of tubular objects and its application to medical image analysis. In: Pattern Recognition. (2008) 163–172

[4] Bigun, J., Granlund, G.H.: Optimal orientation detection of linear symmetry. In: First International Conference on Computer Vision, ICCV (London). (1987) 433–438

[5] Carvalho, D.D., Klein, S., Akkus, Z., Gerrit, L., Schinkel, A.F., Bosch, J.G., van der Lugt, A., Niessen, W.J.: Estimating 3D lumen centerlines of carotid arteries in free-hand acquisition ultrasound. International journal of computer assisted radiology and surgery **7**(2) (2012) 207–215

[6] Cobbold, R.S.C.: Foundations of Biomedical Ultrasound. Biomedical engineering series. Oxford University Press, USA (2006)

[7] Cootes, T.F., Taylor, C.J.: Active shape models smart snakes. In: British Machine Vision Conference 1992. Springer (1992) 266–275

[8] Frangi, A.F., Niessen, W.J., Vincken, K.L., Viergever, M.A.: Multiscale vessel enhancement filtering. In: Medical Image Computing and Computer-Assisted Interventation—MICCAI'98. (1998) 130–137

[9] Freiman, M., Joskowicz, L., Sosna, J.: A variational method for vessels segmentation: algorithm and application to liver vessels visualization. In: SPIE Medical Imaging, International Society for Optics and Photonics (2009) 72610H–72610H

[10] Gülsün, M.A., Tek, H.: Robust vessel tree modeling. In: Medical Image Computing and Computer-Assisted Intervention–MICCAI 2008. (2008) 602–611

[11] Grady, L.: Random walks for image segmentation. Pattern Analysis and Machine Intelligence, IEEE Transactions on **28**(11) (Nov 2006) 1768–1783

[12] de Groot, E., Hovingh, G.K., Wiegman, A., Duriez, P., Smit, A.J., Fruchart, J.C., Kastelein, J.J.: Measurement of arterial wall thickness as a surrogate marker for atherosclerosis. Circulation **109**(23 suppl 1) (2004) III–33

[13] Guerrero, J., Salcudean, S.E., McEwen, J.A., Masri, B.A., Nicolaou, S.: Real-time vessel segmentation and tracking for ultrasound imaging applications. Medical Imaging, IEEE Transactions on **26**(8) (2007) 1079–1090

[14] Kannappan, P., Sahoo, P.: Rotation invariant separable functions are gaussian. SIAM Journal on Mathematical Analysis **23**(5) (1992) 1342–1351

[15] Karamalis, A., Wein, W., Klein, T., Navab, N.: Ultrasound confidence maps using random walks. Medical Image Analysis **16**(6) (2012) 1101 – 1112

[16] Kass, M., Witkin, A., Terzopoulos, D.: Snakes: active contour models. International Journal of Computer Vision **1**(4) (1988) 321–331

[17] Krissian, K., Ellsmere, J., Vosburgh, K., Kikinis, R., Westin, C.F.: Multiscale segmentation of the aorta in 3D ultrasound images. In: Engineering in Medicine and Biology Society, 2003. Proceedings of the 25th Annual International Conference of the IEEE. Volume 1. (2003) 638–641

[18] Krissian, K., Malandain, G., Ayache, N., Vaillant, R., Trousset, Y.: Model-based detection of tubular structures in 3D images. Computer vision and image understanding **80**(2) (2000) 130–171

[19] Lindeberg, T.: Scale-space theory: a basic tool for analyzing structures at different scales. Journal of Applied Statistics **21**(1-2) (1994) 225–270

[20] Liu, S., Padfield, D., Mendonca, P.: Tracking of carotid arteries in ultrasound images. In: Medical Image Computing and Computer-Assisted Intervention–MICCAI 2013. (2013) 526–533

[21] Noble, J.: Ultrasound image segmentation and tissue characterization. Proceedings of the Institution of Mechanical Engineers, Part H: Journal of Engineering in Medicine **224**(2) (2010) 307–316

[22] Pock, T., Beichel, R., Bischof, H.: A novel robust tube detection filter for 3d centerline extraction. In: Image Analysis. (2005) 481–490

[23] Pock, T., Janko, C., Beichel, R., Bischof, H.: Multiscale medialness for robust segmentation of 3D tubular structures. In: 10th Computer vision winter workshop. (2005) 93–102

[24] Waelkens, P., Ahmadi, S.A., Navab, N.: Frangi goes US: multiscale tubular structure detection adapted to 3D ultrasound. In: Medical Image Computing and Computer-Assisted Intervention–MICCAI 2012. (2012) 625–633

[25] Wang, D., Klatzky, R., Amesur, N., Stetten, G.: Carotid artery and jugular vein tracking and differentiation using spatiotemporal analysis. In: Medical Image Computing and Computer-Assisted Intervention–MICCAI 2006. (2006) 654–661

[26] Wang, D.C., Klatzky, R., Wu, B., Weller, G., Sampson, A.R., Stetten, G.D.: Fully automated common carotid artery and internal jugular vein identification and tracking using B-mode ultrasound. Biomedical Engineering, IEEE Transactions on **56**(6) (2009) 1691–1699

[27] Wein, W., Pache, F., Röper, B., Navab, N.: Backward-warping ultrasound reconstruction for improving diagnostic value and registration. In Larsen, R., Nielsen, M., Sporring, J., eds.: Medical Image Computing and Computer-Assisted Intervention – MICCAI 2006. Volume 4191 of Lecture Notes in Computer Science. (2006) 750–757

[28] Xu, C., Prince, J.L.: Gradient vector flow: A new external force for snakes. In: Computer Vision and Pattern Recognition, 1997. Proceedings., 1997 IEEE Computer Society Conference on, IEEE (1997) 66–71

D

3D Velocity Field and Flow Profile Reconstruction from Arbitrarily Sampled Doppler Ultrasound Data

Oliver Zettinig[1], Christoph Hennersperger[1], Christian Schulte zu Berge[1], Maximilian Baust[1], and Nassir Navab[1]

[1] Chair for Computer Aided Medical Procedures (CAMP), Technische Universität München, Germany.

Contributions. The main work for this publication was done jointly by Christoph Hennersperger and Oliver Zettinig. The core idea for pulse phase retrieval was developed initially and refined in joint discussions with all co-authors. Implementation was done by Oliver Zettinig, the construction of the experimental setup by Christoph Hennersperger, and the writing of the publication performed together and in conjunction with the co-authors.

Abstract. With the need for adequate analysis of blood flow dynamics, different imaging modalities have been developed to measure varying blood velocities over time. Due to its numerous advantages, Doppler ultrasound sonography remains one of the most widely used techniques in clinical routine, but requires additional preprocessing to recover 3D velocity information. Despite great progress in the last years, recent approaches do not jointly consider spatial and temporal variation in blood flow. In this work, we present a novel gating- and compounding-free method to simultaneously reconstruct a 3D velocity field and a temporal flow profile from arbitrarily sampled Doppler ultrasound measurements obtained from multiple directions. Based on a laminar flow assumption, a patch-wise B-spline formulation of blood velocity is coupled for the first time with a global waveform model acting as temporal regularization. We evaluated our method on three virtual phantom datasets, demonstrating robustness in terms of noise, angle between measurements and data sparsity, and applied it successfully to five real case datasets of carotid artery examination.

D.1 Introduction

Today, there are several medical imaging techniques for non-invasive quantitative and qualitative blood flow assessment. Although conventional Doppler ultrasound (US) sonography suffers from limited anatomical accessibility as well as high inter-observer variability, it is still an indispensable imaging modality for this task in clinical routine. The reason for this fact is that in comparison to 4D magnetic resonance imaging and digital subtraction angiography, US is broadly available, allows for fast acquisitions, offers high frame rates, and does not expose the patient to ionizing radiation or nephrotoxic contrast agent. Yet, Doppler US can only measure the projection of the true velocity vector along the echo beam direction and is thus blind to the flow orthogonal to it. As a consequence, examiners need experience in order to make qualitative assertions regarding the three-dimensional blood flow, which also explains the recent endeavors to reconstruct three-dimensional flow fields from multiple Doppler acquisitions.

Since the early works by Fox et al. [3], who utilized simultaneous measurements from multiple directions to recover velocity information, cross-beam techniques have been proposed to overcome this limitation [2]. Alternative approaches such as the augmentation of single 2D Doppler images using ventricular wall motion [4] have the potential to successfully reconstruct vortex patterns but rely on additional restrictions. Arigovindan et al. [1] introduced B-spline grids to regularize the reconstruction problem. An extension of their approach by Gomez et al. [5] allows for 3D blood flow quantification from multiple registered B-Mode and Doppler volumes acquired by a 2D matrix array probe. However, the method requires pulse phase consistency, i.e. samples acquired at (or interpolated for) the same instant in time, and fails if temporally arbitrary Doppler samples are used. Inspired by the work of Waechter et al. [8], who employ a waveform model to regularize the estimation of blood flow parameters from rotational angiography, we propose a method which facili-

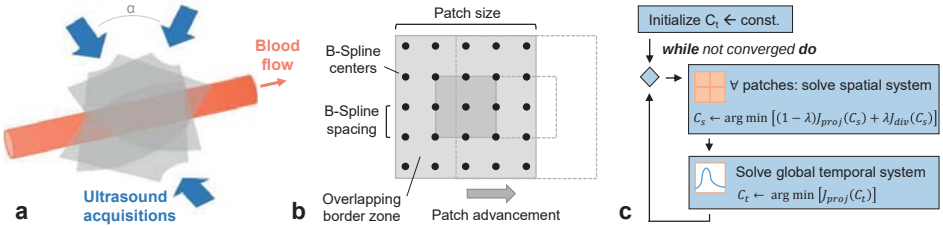

Figure D.1: **a)** Three ultrasound sweeps from different directions are necessary to reconstruct the velocity field in a blood vessel. **b)** Illustration of the patch-wise reconstruction scheme. After reconstruction, only the estimated B-spline coefficients in the non-overlapping core zone are stored. **c)** Algorithm to solve spatial velocity field and temporal flow profile function. *See text for details.*

tates the simultaneous reconstruction of both a continuous three-dimensional velocity field and a continuous waveform model. Thanks to the temporal regularization provided by the waveform model, the proposed method is *gating-free* in the sense that no data selection according to a gating signal is required and that the reconstruction is performed over the entire dataset at once. Therefore, it supports temporally arbitrary Doppler samples from any pulse phase as input. Moreover, the proposed approach is also *compounding-free* as it is based on the raw Doppler in-phase and quadrature (IQ) samples and thus also allows spatially arbitrary, non-uniform data points, without prior compounding of US volumes and associated interpolation artifacts.

D.2 Methods

The reconstruction method relies on raw Doppler IQ samples as input. In particular, 4-tuples of $(\mathbf{p}, \mathbf{d}, m, t)$ are collected for every sample, where $\mathbf{p} = [p_x, p_y, p_z]^\intercal$ denotes the sample position in Cartesian space, $\mathbf{d}$ the corresponding normalized echo beam direction, m the measured Doppler signal, and $t \in [0, 1]$ the normalized pulse phase time. B-spline basis functions are employed to describe a smooth 3D velocity field $\mathbf{v}(\mathbf{p}) = [v_x(\mathbf{p}), v_y(\mathbf{p}), v_z(\mathbf{p})]^\intercal$ [5], whose components are given by

$$v_\gamma(\mathbf{p}) = \sum_{i,j,k} c^\gamma_{i,j,k}\, \beta^n_{s,i}(p_x)\beta^n_{s,j}(p_y)\beta^n_{s,k}(p_z), \qquad \text{for } \gamma \in \{x, y, z\}. \tag{D.1}$$

The indices i, j, and k indicate a location in the regular, three-dimensional B-spline grid with spacing s, which defines the resolution of the recovered vector field. $\beta^n_{s,i}(p_x) = \beta^n(i/s - p_x)$ denotes the scaled and translated B-spline basis function of degree n at grid position i, likewise for $\beta^n_{s,j}(p_y)$ and $\beta^n_{s,k}(p_z)$. Finally, $c^\gamma_{i,j,k}$ are the corresponding B-spline coefficients to be found.

The original approach in [5] relies on an input dataset with N samples sharing the same pulse phase, from which the reconstruction is performed by minimizing the error between the measured Doppler value denoted by m_r and the projection of the recovered velocity at sample position $\mathbf{p}_r$ onto the beam

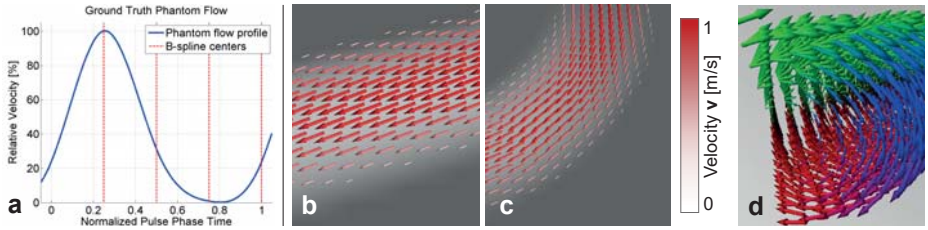

Figure D.2: **a)** Ground truth flow profile function defined using periodic B-spline coefficients. **b-d)** Results of phantom experiment reconstructions closely reflect expected results. Vector fields for *Linear* (b) and *Curved* (c) phantoms, as visible in longitudinal slices, follow vessel direction indicated in the background and exhibit quadratic velocity distributions. Expected rotatory symmetry in the *Barrel Roll* phantom (d) can be easily observed using direction-based color-mapping.

direction $\mathbf{d}_r$

$$J_{proj}(\mathbf{v}) = \sum_{r=1}^{N} \|\mathbf{d}_r \cdot \mathbf{v}(\mathbf{p}_r) - m_r\|_2^2 . \tag{D.2}$$

However, this formulation has to be adjusted for different pulse phases because the blood flow at every point within an artery varies over time. Thus, uncorrected Doppler measurements lead to inconsistent samples, prohibiting the reconstruction of the velocity field at a given instant. In this work, we introduce a flow profile function $\varphi(t)\colon [0,1] \to [0,1]$ mapping from normalized pulse phase times to scaling factors compensating the varying flow patterns (Fig. D.2a). The actual velocity vector at any point in time is then given by $\mathbf{v}(\mathbf{p},t) = \varphi(t)\,\mathbf{v}_{max}(\mathbf{p})$, assuming a pulsatile laminar flow. While allowing varying velocity magnitudes over time, our formulation keeps the flow direction constant at any position in the reconstructed volume. Unless bifurcations, high-grade stenoses, or aneurysms are invesigated, this model has been shown to introduce only negligible errors [8]. It should be noted, however, that this formulation does not enforce the velocity directions to be organized in parallel sheets. In order to compute φ, we employ a B-spline parametrization as well: $\varphi(t) = \sum_{\xi=1}^{T} c_\xi^t \beta_{\tau,\xi}^n(t)$, where $\beta_{\tau,\xi}^n(t)$ is a periodic B-spline basis function of degree n and spacing τ evaluated at grid point ξ, and c_ξ^t denote the corresponding temporal B-spline coefficients. As a result, we propose the cost function

$$J_{proj}(\mathbf{v},\varphi) = \sum_{r=1}^{N} \|\varphi(t_r)\,\mathbf{d}_r \cdot \mathbf{v}_{max}(\mathbf{p}_r) - m_r\|_2^2 \qquad \text{s.t.} \ \max_t |\varphi(t)| = 1 \tag{D.3}$$

The constraint in Eq. D.3 is added to the system to ensure that $\mathbf{v}_{max}$ is correctly scaled. For a matrix form expression, the spatial B-spline coefficients are gathered in vector $\mathbf{C}_s = \{c_{i,j,k}^x, c_{i,j,k}^y, c_{i,j,k}^z\}$, the temporal ones in vector $\mathbf{C}_t = \{c_\xi^t\}$. The evaluation of the B-spline functions is encoded, after vectorization of the

3D spatial grid of size M, by sampling matrices $\mathrm{S}_s \in \mathbb{R}^{3N\times 3M}$ and $\mathrm{S}_t \in \mathbb{R}^{N\times T}$

$$\mathrm{S}_s = \begin{bmatrix} \mathrm{S}_p & 0 & 0 \\ 0 & \mathrm{S}_p & 0 \\ 0 & 0 & \mathrm{S}_p \end{bmatrix} \quad \begin{array}{ll} \text{with} & \{\mathrm{S}_p\}_{r,\mathrm{vec}(i,j,k)} = \beta^n_{s,i}(p_{r,x})\beta^n_{s,j}(p_{r,y})\beta^n_{s,k}(p_{r,z}), \\ \text{and} & \{\mathrm{S}_t\}_{r,\xi} = \beta^n_{\tau,\xi}(t) \end{array} \tag{D.4}$$

such that $\mathbf{v}_{max} = \mathrm{S}_s\mathbf{C}_s$ and $\varphi = \mathrm{S}_t\mathbf{C}_t$. The dot product is realized using the direction matrix $\mathrm{D} = [\mathrm{D}^x\mathrm{D}^y\mathrm{D}^z]$ containing diagonal matrices with the three Cartesian components of the beam directions, respectively: $\{\mathrm{D}^x\}_{r,r} = d_{x,r}$, likewise for D^y and D^z. With $\mathbf{m} = \{m_i\}$ referring to the vector of Doppler measurements and $\otimes$ to the component-wise multiplication, the cost function reads

$$J_{proj}(\mathbf{C}_s, \mathbf{C}_t) = \| \left(\mathrm{S}_t\mathbf{C}_t\right) \otimes \left(\mathrm{D}\,\mathrm{S}_s\mathbf{C}_s\right) - \mathbf{m} \|_2^2 . \tag{D.5}$$

For smoothness, a spatial regularization term is added to the final cost function:

$$J(\mathbf{C}_s, \mathbf{C}_t) = (1-\lambda)\; J_{proj}(\mathbf{C}_s, \mathbf{C}_t) + \lambda\; J_{div}(\mathbf{C}_s). \tag{D.6}$$

As shown in [5], the locally acting divergence term $J_{div} = \|\nabla \cdot \mathbf{v}_{max}\|_2^2$, derived using the B-spline formulation, enforces the incompressibility of the blood flow. It should be noted that the flow profile function φ inherently acts as temporal regularization itself, rendering further regularization terms unnecessary.

Provided a global flow profile function φ, the velocity field $\mathbf{v}_{max}$ can be reconstructed directly in a patch-wise fashion. Simultaneously solving for both $\mathbf{v}_{max}$ and φ is, however, not possible. Instead, spatial and temporal coefficients are obtained in an alternating fashion as reported in Fig. D.1c. We employ a LU decomposition with partial pivoting to directly solve the patch-wise spatial system. Hereby, patches mutually overlap for increased stability, and only the core, non-overlapping coefficients in vector $\mathbf{C}_s$ are stored (Fig. D.1b). The global temporal coefficients $\mathbf{C}_t$ are found using a Levenberg-Marquardt solver. Eventually, the algorithm yields two continuously defined results: the reconstructed maximum velocity field $\mathbf{v}_{max}$ and the blood flow profile φ.

D.3 Experiments

Phantom Evaluation. For evaluating our method, three virtual phantom datasets, each spanning 34×34×34 mm, were created. The first two phantoms, denoted *Linear* and *Curved*, contained a cylinder and a torus with a vessel radius of 6 mm, respectively. A quadratic Poiseuille flow with a velocity of $\mathbf{v}_{max,ph} = 1\,\mathrm{m/s}$ in the centerline was applied. The velocity for the third phantom, denoted *Barrel Roll*, was defined as $\mathbf{v}(\mathbf{p}) = a[\mathbf{p} - \mathbf{r}\,(\mathbf{r}\cdot\mathbf{p})] \times \mathbf{r}$, where $\mathbf{r}$ is the direction of the roll and a a scaling factor to ensure $\max \mathbf{v}_{max,ph} = 1$ [6]. In all cases, a phantom flow profile function φ_{ph} as shown in Fig. D.2a was used to construct a time-varying flow profile. Finally, synthetic Doppler sweeps from three directions $\mathbf{d}$ were generated with in total N measurements $m = \varphi_{ph}(t \sim [0,1])\,\mathbf{d}\cdot\mathbf{v}_{max,ph}(\mathbf{p}) + \eta_s + \eta_v$. The pairwise angle between the sweeps, denoted opening angle α as illustrated in Fig. D.1a, was varied between 10° and 90°. For the linear phantom, the mean direction $\bar{\mathbf{d}}$ was set to be 45° tilted against the vessel direction. Two different Gaussian noise models were

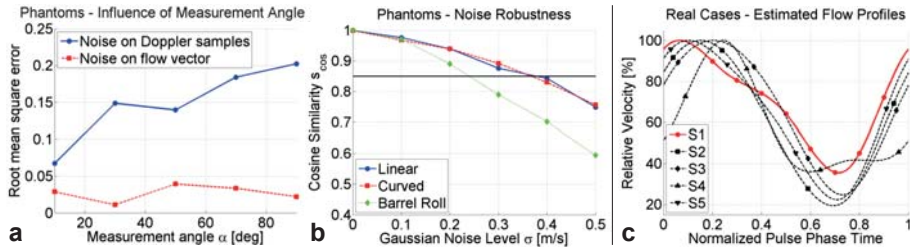

Figure D.3: **a)** The counterintuitive relation between α and the root mean squared error is only present if noise is directly applied to the Doppler samples, regardless of the direction of acquisition. **b)** Gaussian noise of up to $\sigma \leq 0.35$ m/s (*Linear* and *Curved* phantoms) can be added to the Doppler samples before the cosine similarity s_{cos} drops below the success threshold. **c)** The estimated flow profiles of all five subjects reveal the pulsatility of the artery. *See text for details.*

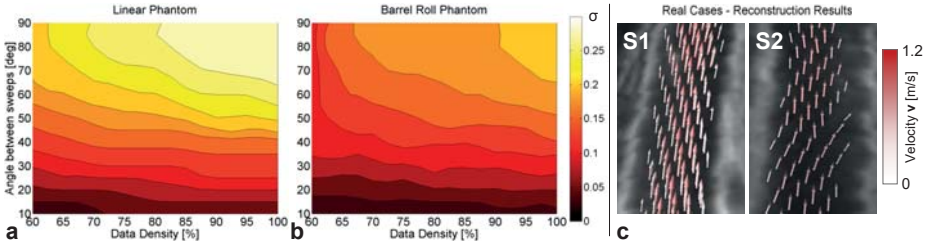

Figure D.4: **a-b) Maximum tolerable Gaussian noise level** σ for linear and barrel roll phantoms such that reconstructions fulfill $s_{cos} > 0.85$ and $e_d < 0.15$. More noise (up to $\sigma = 0.25$ m/s) can be added to samples with higher data density and higher angles between sweeps to still obtain successful reconstructions.

textbfc) Carotid arterty reconstruction results for two exemplary subjects. Overlay of velocity fields on longitudinal B-mode image slices. *See text for details.*

considered: On the one hand, noise with standard deviation σ was added to the samples such that $\eta_s = \mathcal{N}(0, \sigma)$ simulated inaccuracies of the Doppler measurement itself. On the other hand, noise added to the velocity vector under investigation such that $\eta_v = \vec{\mathbf{v}} \cdot \mathbf{d}\, \mathcal{N}(0, \sigma)$, with $\vec{\mathbf{v}} = \mathbf{v} / \|\mathbf{v}\|$, modeled inaccuracies of the tracking system or badly synchronized temporal data. The sample positions $\mathbf{p}$ were chosen from a regular grid with 1 mm spacing. Pulse phase times t were randomly drawn from a uniform distribution. The reconstruction was performed using $6 \times 6 \times 6$ mm patches, with 2 mm overlap, for which only ρN samples were used to mimic sparse sampling (data density $\rho \in [0.6, 1]$). The spatial spacing of the cubic B-splines was fixed at $s = 1.5$ mm. Due to the high runtime complexity of the alternating algorithm (Fig. D.1c), a coarse temporal spacing of $\tau = 0.25$ was used. For all experiments, moderate regularization ($\lambda = 0.1$) and cubic B-splines ($n = 3$) were employed. Three measures were used to analyze reconstruction errors of computed velocities

$\mathbf{v}_{max,c}$ and the estimated flow profile φ_c. While the mean cosine similarity s_{cos} and the mean Euclidean norm e_d quantify errors of the velocity field, the root mean squared error e_{rms} measures how well the flow profile was recovered:

$$\begin{aligned} s_{cos} &= \frac{1}{N}\sum_{r=1}^{N} \vec{\mathbf{v}}_{max,c}(\mathbf{p}_r) \cdot \vec{\mathbf{v}}_{max,ph}(\mathbf{p}_r), \\ e_d &= \frac{1}{N}\sum_{r=1}^{N} \left\| \mathbf{v}_{max,c}(\mathbf{p}_r) - \mathbf{v}_{max,ph}(\mathbf{p}_r) \right\|_2, \\ e_{rms} &= \sqrt{\frac{1}{N}\sum_{r=1}^{N} \left[\varphi_c(t_r) - \varphi_{ph}(t_r) \right]^2}. \end{aligned} \tag{D.7}$$

Real Case Acquisition and Preprocessing Protocol. We tested our method on five carotid artery screening datasets of 25 - 31 year old subjects. An open access ultrasound system (Aurotech ultrasound AS, model MANUS) with a linear array probe (128 elements, single element width 0.27 mm, height 4 mm, focal depth 30 mm, 45 aperture elements) operating at 8 MHz, was used together with an electromagnetic (EM) tracking system (Ascension Technology Corporation, model TrakStar) and a pulse-oximetry sensor (Medlab GmbH, model P-OX100). After calibration and preprocessing as described in [7], the system facilitates the acquisition of Doppler IQ samples as well as a normalized pulse phase signal, mapping the peak-to-peak distances to a linear signal in the interval $[0, 1]$. For each subject, three US sweeps, mutually around $\alpha = 60°$ apart, were acquired. To correct for the limited precision of the EM tracking system, the Doppler magnitudes of each sweep were manually thresholded to obtain a point cloud of the blood vessel. The three point clouds were then registered using ICP in a pairwise manner. It should be noted that a sufficiently precise tracking system, e.g. mechanical tracking, would make this preprocessing obsolete.

D.4 Results and Discussion

Phantom Experiments. Fig. D.2b-d illustrate reconstruction results for all phantoms with the ideal parameter configuration $\alpha = 90°$, $\eta_s = \eta_v = 0$, and $\rho = 1$. For the estimation of the flow profile, the correlation r between e_{rms} and the acquisition parameters was investigated. Interestingly, increasing opening angles α led to higher errors ($r_{rms,\alpha} = +0.18$) when only η_s was applied, which is intuitively more likely to cancel out if all samples are roughly obtained from one direction ($\alpha \approx 0°$). If, however, only η_v was used, no significant relationship between angle and error could be observed ($r_{rms,\alpha} = -0.03$), as shown in Fig. D.3a. Although we expect the latter noise model to be dominant in a clinical scenario, the former model facilitates evaluating the limitations of the method. Therefore, we set $\eta_v = 0$ for all subsequent experiments.

A reconstruction of the velocity field was considered successful if $s_{cos} \geq 0.85$ and $e_d \leq 0.15$ mm. As shown in Fig. D.3b, Gaussian noise of up to $\sigma \leq 0.35$ m/s could be added to the Doppler samples under ideal measurement conditions of $\alpha = 90°$ and $\rho = 1$, before the cosine similarity s_{cos} dropped below the success threshold (similar results were obtained for the Euclidean norm e_d). We evaluated the effect of data density and angle between the measurements

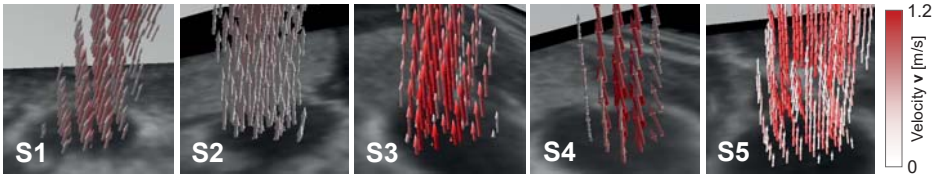

Figure D.5: **Carotid artery reconstruction results** for all five subjects. Overlay of velocity fields on cross-sectional B-mode image slices illustrate that the blood flow pattern was qualitatively well captured *(compounding only for reference)*.

for the same noise range. Figure D.4a-b illustrate the maximum tolerable noise level σ for various acquisition parameters, indicating robustness in terms of data sparsity. As expected, the method was most sensitive to noise for the vortex patterns of the *Barrel Roll* phantom.

Real Case Evaluation. Despite the coarse temporal grid spacing, realistic and qualitatively accurate velocity fields and flow profiles could be successfully reconstructed with a resolution of 1 mm for all five datasets. The estimated flow profiles captured the pulsatility of the artery well (Fig. D.3c). Results illustrated in Fig. D.4c and Fig. D.5 show an overall promising agreement between vector fields and vessel anatomies as seen in the B-mode images. However, in some datasets, e.g. S2, reconstruction errors at the vessel borders are evident. While phantom experiments suggest an unsatisfactory registration of the three sweeps and thus missing vector information at the borders, further evaluation is necessary to assess the effect of the spatially relaxed laminarity assumption.

D.5 Conclusion and Future Work

In this work, we have presented a novel approach to quantify varying blood velocities over time from spatially and temporally arbitrarily sampled Doppler ultrasound measurements. For the first time and to the best of our knowledge, we were able to simultaneously reconstruct a continuous three-dimensional blood velocity field and a periodic temporal flow profile function by coupling a patch-wise B-spline formulation of blood velocity with a waveform model. With the assumption of a laminar flow, our both gating- and compounding-free framework supports Doppler samples from any pulse phase acquired with a tracked freehand ultrasound system. As presented on three virtual phantom datasets, our method is robust with respect to noise, angle between measurements and data sparsity. We were also able to present promising results on five real case datasets of carotid artery screening, showing qualitatively well captured blood flow patterns and realistic, pulsatile flow profiles. Apart from a potentially expedient diagnostic value in clinical routine, our approach may have further important applications, for instance as initialization of computational fluid dynamics models by the recovered flow profile. Possible future extensions of this work include a detailed parameter evaluation, a thorough quantitative validation, a more local definition of the flow profile for handling

bifurcations, and an improvement of ultrasound sweep registration toward higher velocity field resolution.

D.6 References

[1] Arigovindan, M., Suhling, M., Jansen, C., Hunziker, P., Unser, M.: Full motion and flow field recovery from echo doppler data. Medical Imaging, IEEE Transactions on **26**(1) (2007) 31–45

[2] Dunmire, B., Beach, K., Labs, K., Plett, M., Strandness Jr, D.: Cross-beam vector doppler ultrasound for angle-independent velocity measurements. Ultrasound in Medicine and Biology **26**(8) (2000) 1213–1235

[3] Fox, M.D.: Multiple crossed-beam ultrasound doppler velocimetry. Sonics and Ultrasonics, IEEE Transactions on **25**(5) (1978) 281–286

[4] Garcia, D., del Álamo, J.C., Tanné, D., Yotti, R., Cortina, C., Bertrand, É., Antoranz, J.C., Pérez-David, E., Rieu, R., Fernández-Avilés, F., et al.: Two-dimensional intraventricular flow mapping by digital processing conventional color-doppler echocardiography images. Medical Imaging, IEEE Transactions on **29**(10) (2010) 1701–1713

[5] Gomez, A., Pushparajah, K., Simpson, J.M., Giese, D., Schaeffter, T., Penney, G.: A sensitivity analysis on 3D velocity reconstruction from multiple registered echo Doppler views. Medical Image Analysis **17**(6) (2013) 616–631

[6] Hastenteufel, M.: Neue Methoden des 3D Ultraschalls zur Geschwindigkeitsrekonstruktion und intraoperativen Navigation. PhD thesis, Universität Fridericiana, Karlsruhe, Germany (2005)

[7] Hennersperger, C., Karamalis, A., Navab, N.: Vascular 3D+T freehand ultrasound using correlation of doppler and pulse-oximetry data. In Stoyanov, D., Collins, D.L., Sakuma, I., Abolmaesumi, P., Jannin, P., eds.: Information Processing in Computer Assisted Interventions - IPCAI 2014, Lecture Notes in Computer Science. Volume 8498. (2014) in press.

[8] Waechter, I., Bredno, J., Hermans, R., Weese, J., Barratt, D.C., Hawkes, D.J.: Model-based blood flow quantification from rotational angiography. Medical Image Analysis **12**(5) (2008) 586–602